

**PURDUE UNIVERSITY
GRADUATE SCHOOL
Thesis/Dissertation Acceptance**

This is to certify that the thesis/dissertation prepared

By James Hengenius

Entitled Quantitative Modeling of Spatiotemporal Systems: Simulation of Biological Systems and Analysis of Error Metric Effects on Model Fitting

For the degree of Doctor of Philosophy



Is approved by the final examining committee:

Michael Gribskov

Ann Rundell

James Fleet

David Umulis

To the best of my knowledge and as understood by the student in the Thesis/Dissertation Agreement, Publication Delay, and Certification/Disclaimer (Graduate School Form 32), this thesis/dissertation adheres to the provisions of Purdue University's "Policy on Integrity in Research" and the use of copyrighted material.

Michael Gribskov

Approved by Major Professor(s): _____

Approved by: Ann L. Kirchmaier

10/15/2014

Head of the Department Graduate Program

Date

QUANTITATIVE MODELING OF SPATIOTEMPORAL SYSTEMS: SIMULATION
OF BIOLOGICAL SYSTEMS AND ANALYSIS OF ERROR METRIC EFFECTS ON
MODEL FITTING

A Dissertation

Submitted to the Faculty

of

Purdue University

by

James B. Hengenius

In Partial Fulfillment of the

Requirements for the Degree

of

Doctor of Philosophy

December 2014

Purdue University

West Lafayette, Indiana

UMI Number: 3687049

All rights reserved

INFORMATION TO ALL USERS

The quality of this reproduction is dependent upon the quality of the copy submitted.

In the unlikely event that the author did not send a complete manuscript and there are missing pages, these will be noted. Also, if material had to be removed, a note will indicate the deletion.



UMI 3687049

Published by ProQuest LLC (2015). Copyright in the Dissertation held by the Author.

Microform Edition © ProQuest LLC.

All rights reserved. This work is protected against unauthorized copying under Title 17, United States Code



ProQuest LLC.
789 East Eisenhower Parkway
P.O. Box 1346
Ann Arbor, MI 48106 - 1346

For the flies

ACKNOWLEDGEMENTS

I wish to express appreciation to my mentors and committee members, Drs. Michael Gribskov, Ann Rundell, and David Umulis. This work would not be possible without their guidance, knowledge, understanding, and unconditional support.

I would like to thank my committee member, Dr. James Fleet. His commentary and insight brought clarity when I found myself bogged down by minutiae of research.

Further, I am grateful to the insight and feedback provided by fellow graduate students and postdoctoral researchers in the Gribskov, Rundell, and Umulis research groups. It has been a privilege to work with each of these friends and colleagues.

I would be remiss if I failed to acknowledge my friends in the Lafayette area. When inevitable research frustrations mounted, they provided the support helped me rally and tackle problems anew. Without them, this document might not exist.

Finally, I extend my deepest gratitude to Rachel Buckser. She supported and inspired me at my best and worst.

TABLE OF CONTENTS

	Page
LIST OF FIGURES	vi
ABSTRACT	vii
CHAPTER 1. INTRODUCTION.....	1
1.1 Introduction and Scope.....	1
1.2 Computational Systems Biology: Promise and Challenges	3
1.3 Three Spatiotemporal Modeling Case Studies	13
1.3.1 Optimizing Sensitivity of an Amperometric Glucose Biosensor via Simulation of Nanoscale Electrode Placement.....	14
1.3.2 Gap GRN Inference with a 3D Model of the <i>Drosophila melanogaster</i> Embryonic Blastoderm	17
1.3.3 Characterizing the Effects of Objective Function Choice on Estimated Parameters.....	24
1.4 Brief Outline.....	26
CHAPTER 2. OPTIMIZATION OF A NANO-STRUCTURED GLUCOSE BIOSENSOR DESIGN TO MAXIMIZE GLUCOSE SENSITIVITY	29
CHAPTER 3. CAN EMBRYONIC GEOMETRY AND SPATIALLY HETEROGENEOUS MATERNAL PROTEINS ACCOUNT FOR DORSAL-VENTRAL ASYMMETRIES IN GAP GENE PATTERNING?	66
3.1 A Note About this Article	66
CHAPTER 4. THE IMPORTANCE OF CHOOSING PROPER OBJECTIVE FUNCTIONS FOR SPATIOTEMPORAL MODEL OPTIMIZATION	113
4.1 A Note About this Article	113
CHAPTER 5. THE STATE OF THE ART AND FUTURE DIRECTIONS	165
5.1 Overfitting and Its Implications	169
5.2 Countering Overfitting	175
5.3 A Complete Search of the Gap Gene Parameter Space	180
5.4 Concluding Remarks	186
REFERENCES	189

VITA	205
------	-------	-----

LIST OF FIGURES

Figure	Page
Figure 1.1 A Cost Function Landscape.....	11
Figure 1.2 Dorsal-Ventral Patterning Asymmetries in the <i>Drosophila</i> Embryo	23
Figure 5.1 Overfitting and Model Complexity	172
Figure 5.2 Reduced Four-Species Gap Gene Model	182
Figure 5.3 Discretized Gap Gene Data and Sample Model Output	188

ABSTRACT

Hengenius, James B. Ph.D., Purdue University, December 2014. Quantitative Modeling of Spatiotemporal Systems: Simulation of Biological Systems and Analysis of Error Metric Effects on Model Fitting. Major Professor: Michael Gribskov.

Understanding the biophysical processes underlying biological and biotechnological processes is a prerequisite for therapeutic treatments and technological innovation. With the exponential growth of computational processing speed, experimental findings in these fields have been complemented by dynamic simulations of developmental signaling and genetic interactions. Models provide means to evaluate “emergent” properties of systems sometimes inaccessible by reductionist approaches, making them test beds for biological inference and technological refinement.

The complexity and interconnectedness of biological processes pose special challenges to modelers; biological models typically possess a large number of unknown parameters relative to their counterparts in other physical sciences. Estimating these parameter values requires iterative testing of parameter values to find values that produce low error between model and data. This is a task whose length grows exponentially with the number of unknown parameters. Many biological systems require spatial representation (*i.e.*, they are not well-mixed systems and change over space and time). Adding spatial dimensions complicates parameter estimation by increasing computational time for each

model evaluation. Defining error for model-data comparison is also complicated on spatial domains. Different metrics compare different features of data and simulation, and the desired features are dependent on the underlying research question.

This dissertation documents the modeling, parameter estimation, and simulation of two spatiotemporal modeling studies. Each study addresses an unanswered research question in the respective experimental system. The former is a 3D model of a nanoscale amperometric glucose biosensor; the model was used to optimize the sensor's design for improved sensitivity to glucose. The latter is a 3D model of the developmental gap gene system that helps establish the bodyplan of *Drosophila melanogaster*; I wished to determine if the embryo's geometry alone was capable of accounting for observed spatial distributions of gap gene products and to infer feasible genetic regulatory networks (GRNs) via parameter estimation of the GRN interaction terms. Simulation of the biosensor successfully predicted an optimal electrode density on the biosensor surface, allowing us to fabricate improved biosensors. Simulation of the gap gene system on 1D and 3D embryonic demonstrated that geometric effects were insufficient to produce observed distributions when simulated with previously reported GRNs. Noting the effects of the error definition on the outcome of parameter estimation, I conclude with a characterization of assorted error definitions (objective functions), describe data characteristics to which they are sensitive, and end with a suggested procedure for objective function selection. Choice of objective function is important in parameter estimation of spatiotemporal system models in varied biological and biotechnological disciplines.

CHAPTER 1. INTRODUCTION

1.1 Introduction and Scope

Spatiotemporal models of biological systems provide insights in life science, bio-engineering, and other disciplines. Biological models are unique in the large numbers—and uncertainty in the values—of physiochemical parameters. All parameters in a model are a parameter set (θ) and all parameter set values must be estimated to produce realistic model behavior. Estimation requires a search of an abstract parameter space. The number of dimensions of the space corresponds to the number of parameters, so the size (and difficulty) of the estimation problem grows exponentially with the numbers of unknown parameters. To discover superior parameter sets, modelers must choose objective functions to quantify error between experimental data and the model output of different parameter sets. The objective is typically a variant of the sum of squared error although the effects of objective selection on biological parameter estimation has not been well studied.

This work documents the modeling, parameter estimation, and simulation of two spatiotemporal modeling studies. Each study addresses an unanswered research question in the respective experimental system. The former is a 3D model of a nanoscale amperometric glucose biosensor; the model was used to optimize the sensor's design for

improved sensitivity to glucose. The latter is a 3D model of the developmental gap gene system that helps establish the bodyplan of *Drosophila melanogaster*; we wished to determine if the embryo's geometry alone was capable of accounting for the spatial distributions of gap gene products and to infer feasible genetic regulatory networks (GRNs) via parameter estimation of the GRN interaction terms.

Motivated by the successes and failures of these modeling studies, we noted a relationship between the objective function and the parameter estimation. As with preceding studies, we used Euclidian distance (a variant of the sum of squared error) as our objective function. For the biosensor model, which required quantitative agreement between model and data to properly address the design optimization problem, the Euclidean distance was appropriate to minimize the quantitative error between observed and simulated current. However, the estimation of *Drosophila* GRN parameters depends on "semi-quantitative" immunofluorescence data that cannot be absolutely calibrated to protein concentration. As such, only qualitative agreement between the shape and relative position of embryonic protein expression bands can be used to compute error. The choice of objective must account for this. The Euclidean distance's dependence on quantitative summation of errors made it a poor choice in this case. It assigned high errors to qualitatively similar model output (*e.g.*, similar experimental and simulated protein distributions with differing magnitudes). In response, this work presents an initial characterization of the effects of objective function choice on qualitative spatial error calculations. Though we apply it to the *Drosophila* gap gene system, this study is applicable to spatial and spatiotemporal models relying on spatial distributions with

ratiometric rather than defined, absolute measures – a common situation in biological models with spatial dimensions.

1.2 Computational Systems Biology: Promise and Challenges

In contrast to the traditionally reductionist approaches to biological research, some recent scholars have chosen to frame their inquiries in the context of “systems biology”, a popular but poorly defined catchphrase for holistic and integrative approaches to biological understanding. Various attempts to define the phrase have been offered by biologists and philosophers, though tension remains as to whether it refers to computational simulation of biological systems or bioinformatics, the analysis of high-throughput “-omics” data (*e.g.*, genomics, transcriptomics, proteomics, etc.)[1-7].

Prototypical systems biology concepts are found as early as the 1940s, when Norbert Wiener applied aspects of control theory to biology in his seminal *Cybernetics, or Control and Communication in the Animal and in the Machine*[8]. The discipline was further developed in 1968 when “Systems Theory and Biology” was selected as the topic of the Third Systems Symposium at the Case Institute of Technology[9]. In the 1960s and 1970s, Michael Savageau and contemporaries developed biochemical systems theory to simulate and analyze metabolic networks [10-12]. The term “bioinformatics”, referring to information flow through biological systems, was also coined in 1970[13]. The 1980s saw the introduction and growth of flux balance analysis, a computationally efficient method for approximating steady-state chemical flux through metabolic networks[14]. The focus expanded from computational analysis to include bioinformatics in the 1990s.

This decade marked several milestones in DNA sequencing, from the initiation of sequencing for the Human Genome Project[15] to the first complete genome (*Haemophilus influenzae*)[16], and decreases in the time and cost required to collect genomic data[17]. The accumulation of sequence data required processing and analysis, and the field of bioinformatics expanded to apply computational approaches to sequence assembly, phylogenetic alignment, network analysis, molecular structure simulation/prediction, and data mining techniques to extract novel biological associations among genomic and other high-throughput data[18,19]. From the 1990s to today, computational biologists and bioinformaticists have applied modeling and data analyses toward an integrative understanding of biological systems. In this work, we focus on mathematical modeling and computational simulation within the larger framework of systems biology. Specifically, we will describe the benefits and challenges of using mathematical models to predict biological outcomes and to infer physiologically meaningful relationships among simulated biochemical species.

Mathematical models of varying complexity are used to represent diverse dynamic phenomena in the biological sciences. A dynamic model describes change in the system state variable(s) over a time course of interest; it contains explicit mechanistic descriptions of the system and rules for updating the state of the system in time [20]. Independent of the mechanistic description, the behavior of the model depends on the initial conditions of the system (*e.g.*, simulated molecular concentrations at time zero). Developmental models often simulate spatially heterogeneous systems; in these cases the shape of the spatial domain also affects outcome. Mechanistic dynamic models are

parametric[21]. In addition to the state of the system and the shape of its domain, parameters are constant values that define the behavior of the system and often have biophysical interpretations (*e.g.*, binding rate constants are parameters of receptor binding models) [22,23]. To determine the applicability of a model, parameter estimation must be used to bring the model into agreement with data[24]. This involves iteratively simulating the model with different parameter values and comparing the resultant output to data. Parameters that yield simulated values minimally different (or maximally similar) to data are retained[24-26]. The difficulty of this parameter search depends on the range each parameter is allowed to assume, the number of parameters to be estimated, the covariance of parameters with model output, and the number of local minima where search algorithms may become trapped[27]. The specific type of model determines both the type of data needed to inform the model and the parameter estimation methods that relate the model to the data.

Even after parameters are estimated, mathematical models of complex biological and biotechnological systems exist in an “uncanny valley”; many models look and behave *almost* like the natural systems they are designed to simulate, but they display imperfections that make their predictions suspect. The disparity between a model result and the actual system’s behavior may be a small-yet-systemic mismatch or a complete absence of a frequently observed experimental feature. This “uncanny valley” for models might suggest that modeling is a distraction that interferes with experimental discovery because models attempt to show how the system works in quantitative detail, yet they are typically simplified relative to the system under study. Among mathematical biologists it

is understood that simulations will always be simplifications incapable of reproducing all experimental behaviors; however, imperfect models still promote greater understanding of biological behaviors. More recently, they have been informing experimental design and testing assumptions when experiments are infeasible.

Central to modeling is the need to quantify how well a model agrees with experimental data and identify where it might disagree. Because model output depends on the model parameters, parameter estimation (*i.e.*, parameter optimization) algorithms must be able to quantitatively score and sort parameter sets according to how well their corresponding outputs agree with data. This quantification of model-to-data agreement is determined by an objective function that measures the model error with respect to data; however, there are many objective functions to measure model-data error and the choice of objective depends on the type of data, the type of model, and the research question(s) being asked. In Chapter 4 we compare diverse objectives for the calculation of model-data error and identify each function's strengths and weaknesses in the context of developmental pattern formation by morphogens.

The quality of a parameterized model's output, the uncertainty of its predictions, and the proper choice of objective function all depend on the type and quality of the data used for the training and optimization of the model. Data collected from biosensor experiments comes in the form of total device amperage; this current represents the aggregate of redox reactions occurring at the sub-micron scale[28-30]. Meanwhile, experimental data common in the analysis of morphogen signaling systems may take several forms

depending on the nature of the assays used. Broadly, this data may be separated into qualitative, semi-quantitative, and quantitative data. Specifically, qualitative data encodes nonnumeric descriptors of the morphogen and targets of interest; semi-quantitative data is predominantly ratiometric such as the relative intensity of a stained biomolecule or intensity of a band in a western blot; and quantitative data provides information of specific, measured quantities with associated uncertainty such as absolute concentrations. As the quantitative content of the data increases, the associated uncertainties typically decrease providing more stringent constraints that improve the resulting model (see Pargett and Umulis, 2013 and Pargett, 2013 for further details [31,32]).

Once mechanistic model parameters are optimized to maximize model-data agreement, they can be used to address a number of important questions. They can include explicitly defined biochemical species and reactions, thus encoding hypotheses and allowing researchers to determine if a given hypothesis (model formulation) is sufficient to recapitulate experimental observations[33,34]. Multiple models (hypotheses) may also be compared to discover which best fits data. Rather than encoding a single hypothesis, a model may have many unknown interactions (*e.g.*, genetic regulatory interactions) represented by parameters; estimating parameters that fit simulations to observations generates biologically interpretable inferences (*e.g.*, feasible GRNs) which may direct further experimental work[35]. With sufficient confidence in a model, researchers may make qualitative and quantitative predications regarding the dynamics of experimentally observable and unobservable chemical species simulated by the model. These models

may be used to perform “surrogate experiments” when experimental techniques are unavailable or too costly to probe the dynamics of species relevant to research questions. Finally, techniques of sensitivity analysis (SA) may be used in design of experiments and the control of biological systems.

Mechanistic models should not be confused with statistical models (sometimes known as phenomenological models). Statistical models (*e.g.*, linear or logarithmic regression) quantify correlation among observable data. This knowledge often proves invaluable in hypothesis generation, but statistical models’ predictive power is limited to interpolation within the range of existing data [36]. Conversely, mechanistic models encode users’ suppositions about the nature of the underlying system. As such, they may be used to extrapolate beyond the range of current data and provide predictions *given that the modeled mechanism is accurate*.

To illustrate this difficulty, consider a simple combinatorial experimental design. A researcher desires to sample three experimental variables, each at two different levels. A complete set of experiments would contain 2^3 (8) experiments. Now consider a similar design that contains ten experimental variables. A combinatorial design would involve 2^{10} (1024) separate experiments. In parameter estimation, the number of unknown parameters (n_θ) is analogous to the number of experimental variables. The resolution of the search increases with the number of levels (n_{level}) at which parameters are sampled. A combinatorial search of the parameter space requires $n_{level}^{n_\theta}$ samples. While computers may simulate hours of biological activity in less than a second, the sheer

number of simulations requires nontrivial amounts of time. Biological models may contain as few as one or two parameters (*e.g.*, Michaelis-Menten kinetic simulations) and as many as dozens or hundreds of parameters. Further, the sensitivity of biological models to small changes in parameter values means that high resolution is required to sufficiently cover the parameter space. In a low resolution search ($n_{level} = 100$) of a forty parameter model ($n_{\theta} = 40$) requiring 0.1 seconds ($t = 0.1s$) per simulation, the total time required is equal to $tn_{level}^{n_{\theta}} = 1 \times 10^{79}$ seconds or 3.2×10^{71} years. By comparison, the age of the universe is only thought to be 1.5×10^{10} years[37]!

There are several means by which computational biologists may reduce the total time (also known as computation cost) required for large-scale parameter space searches. One method is to parallelize the task over many central processing units (CPUs). For the combinatorial example above, in which each simulation in the parameter space is completely independent, the $n_{level}^{n_{\theta}}$ simulations may be parceled out to c individual processors. This leads to a total time of $tn_{level}^{n_{\theta}}/c$ and a time reduction proportional to $1/c$. This represents the maximum reduction for completely independent simulations; many search algorithms are not completely parallelizable and exhibit a more modest reduction. Regardless, the numerator grows exponentially with n_{θ} but only decreases proportional to $1/c$, often leaving an unacceptable computational cost. Another avenue for cost reduction involves decreasing the individual simulation time t . Investigators may optimize simulation software to improve its efficiency, though this approach is problem-specific and may not be possible with all models. Finally, algorithmic alternatives to

exhaustive searches (*e.g.*, factorial screens) may be implemented to decrease the number of model evaluations.

These optimization approaches use different criteria to sample subsets of the parameter space, but they proceed from a common starting point: The unknown parameters have biologically feasible ranges assigned to them (*e.g.*, a kinetic constant or diffusion constant cannot be negative). Then an incomplete search is performed within this constrained feasible region of the parameter space while ignoring biologically impossible parameter value combinations. Sampled parameter sets are ranked according to the objective function values of their output. Finally, investigator-established criteria are used to decide whether the fit is “good enough.” If it is, the algorithm terminates; if not, it may be restarted or allowed to continue until a user-specified time limit is reached.

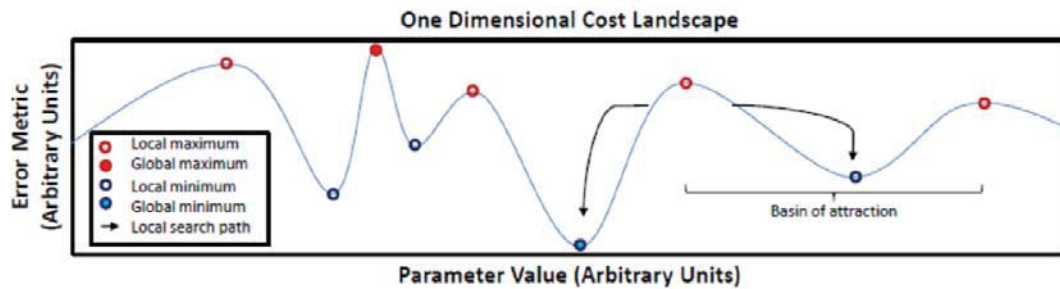


Figure 1.1 A Cost Function Landscape

When parameter values are mapped to error values via an objective function, a high-dimensional cost surface is revealed. This plot represents model error as one parameter is changed. Maxima (red circles) and minima (blue circles) dot the cost surface; parameter estimation seeks the global minimum (filled blue circle), or best fit, though this is not always attainable. Each local minimum (empty blue circle) has an associated basin of attraction bounded by adjacent maxima; local searches must start within the global minimum's basin to converge to the global minimum. Because basins may be small and local methods would need to start within the basin, global searches are used to survey the cost surface for low-error points from which to launch local searches.

The mapping of objective function error values to feasible parameter combinations (points in the parameter space) results in a map called a cost landscape (so named because classical business applications sought to minimize costs; we seek to minimize error). See **Figure 1.1** for a one-parameter cost landscape. Optimization algorithms seek the parameter set corresponding to the lowest error – the global minimum or the lowest point of the landscape – to minimize the cost [24,25]. Broadly, optimization algorithms may be categorized as local and global[38]. Local search methods begin at an expert’s “best guess” and proceed “downhill” on the landscape to the nearest minimum (black arrows, **Fig. 1.1**). Because biological data is noisy and precise prior knowledge of biological systems is often unavailable, researchers’ “best guesses” are often uncertain and these methods usually lead to a local rather than global minimum. To avoid such local minima traps, stochastic global searches are used to sample the whole feasible region without completely searching the space [39]. However, the size of the space grows exponentially while objective function calculation proceeds linearly. Due to the curse of dimensionality, such global searches covers a smaller fraction of the feasible region as the number of parameters grows. As a result, parameters reported in the literature are likely to represent local rather than global minima.

Search algorithms are typically run multiple times to improve coverage of the space. When searches return optimized parameter sets, these sets are ranked by goodness-of-fit. Those with the lowest objective values are retained, though investigators often inject an element of subjectivity by ranking the lowest cost parameters “by eye.” This expert

evaluation, coupled with the probabilistic nature of the search makes independent reproducibility of parameter estimation and model analyses more difficult.

This work focuses on three case studies of three spatiotemporal system models: First, we developed a three-dimensional (3D) model of a nanoscale glucose biosensor utilizing glucose oxidase and electrodeposited platinum electrodes; after parameter estimation, we used the model to optimize the nanoscale design features and improve the sensor's glucose sensitivity. Second, we constructed a 3D embryonic model of the *Drosophila melanogaster* developmental gap gene system and attempted to infer GRNs compatible with observed protein expression; only one family of GRNs was recovered. Finally, after noting the unexpected lack of multiple feasible GRNs, we constructed a 1D model of embryonic gap gene patterning and characterized the sensitivity of parameter estimation to the choice of model-data error functions (*i.e.*, objective functions) used to minimize error; this is described in detail in **Chapter 4**.

1.3 Three Spatiotemporal Modeling Case Studies

Spatiotemporal dynamic models are widely used in simulations of physical systems and engineering. In these applications many model parameters are fixed at known values (*e.g.*, materials properties such as moduli, viscosities, and heat capacities), leaving few unknown parameters to estimate. Such simulations may also require hours to days per simulation, severely limiting or completely removing the ability to perform parameter estimation. However, the accurate prior knowledge of the system parameters often yields low error simulations. In contrast, limited prior knowledge of biological and

biotechnological parameter values and the quasi-physical nature of some parameters (e.g., “lumped” kinetic constants) immensely increase the difficulty of parameter optimization and interpretation in biological models; adding spatial dimensions further increases the computational expense of model evaluation.

1.3.1 Optimizing Sensitivity of an Amperometric Glucose Biosensor via Simulation of Nanoscale Electrode Placement

The increasing prevalence of insulin-dependent diabetes over the past three decades has increased the need for patient-operable glucose sensors[40]. These devices allow patients to monitor their blood glucose concentration and thus administer proper amounts of insulin. Though diabetes was eighth leading cause of death worldwide and the seventh leading cause of death in the United States in 2011, claiming 1.4 million lives[41,42], patient compliance with recommended glucose monitoring practices may be as low as 20%-50% among individuals with type 1 and 2 diabetes[43]. Poor compliance is often attributed to capillary glucose testing, the commonplace method used to let blood for glucose measurement, due to its invasive nature (a fingertip needle prick) and associated discomfort. One solution to this problem is surgical implantation of closed-loop insulin pumps or “artificial pancreases” [44,45]. Such devices monitor glucose and administer insulin independent of patients’ actions. This approach has two key limitations: Firstly, patients discouraged by invasive blood drawing methods might be more intimidated by the prospect of invasive surgical procedures. Secondly, diabetes incidence and mortality both correlate with lower socioeconomic status [46,47]; surgical intervention can be

prohibitively expensive to individuals with lower incomes and limited access to medical care.

An alternative approach to increased compliance is reduction of patient discomfort with noninvasive self-testing utilizing saliva or tear samples in place of blood [48-50].

Unfortunately, the glucose concentrations in these bodily fluids are orders of magnitude below blood glucose and cannot be accurately measured by current commercial home-use glucose monitors[48,51,52]. Improving the sensitivity and sensing range of glucose monitors has been a longstanding challenge in biomedical engineering. Research efforts have evaluated chemical, spectroscopic, electrochemical, and other approaches to this problem.

In Chapter 2 we describe a model-driven approach to optimization of an electrochemical sensor. Modern commercial glucose monitor designs are dominated by electrochemical mechanisms[53]. These devices employ test strips containing electrodes and a bioactive reagent (typically glucose oxidase) that oxidizes glucose. Glucose oxidation triggers a series of redox reactions. Glucose oxidation corresponds with the reduction of a mediator molecule; mediators vary from design to design[54-56]. The mediator is oxidized at the electrode surface to generate a measurable current[55].

The developing field of nanotechnology has provided new fabrication methods and miniaturization of electrical biosensors[28,57-88]. The detection limits and sensitivities of electrochemical biosensors are governed in part by the kinetic and diffusional

parameters of the biosensor system. When diffusional mass transport rates are much greater than enzyme kinetic rates, diffusion replenishes glucose as it is consumed at the biosensor surface. As a result, the micro-environment of the electrode experiences glucose concentrations similar to the bulk solution. In this regime, enzyme kinetics dominate. Observed current is proportional to the bulk glucose concentrations below the saturation regime of the enzyme. In the diffusion-limited regime, enzyme kinetics outpace mass transport. This leads to a depletion of glucose around the electrode, especially when the concentrations are low and the small glucose concentration gradient slows mass transport to the electrode. This phenomenon prevents linear calibration of glucose concentration with current and raises the lower detection limit. Finally, enzyme kinetic parameters affect linear sensing at decreased glucose concentrations. Apparent Michaelis-Menten parameter (K_M) values represent the half-saturation concentration of the enzyme about which the concentration response is approximately linear. Lower effective K_M values correspond to linear response at lower concentrations.

Nanoscale electrochemical studies have demonstrated improvements in the sensitivity and accuracy of glucose biosensors. Approaches include spectroscopic methods [89-93], novel materials for nanoscale electrodes and glucose oxidase scaffolding [94-98], and geometrically novel nanoelectrodes [82,99-104]. Though some attempts have been made to model biosensor designs via computational simulation [105-108], most design optimization approaches rely on experimental trial-and-error tuning of fabrication variables. In Chapter 2, we evaluate a previously-published novel biosensor design in which sub-micron spherical platinum electrodes were deposited upon single-walled

carbon nanotube (swCNT) conductors [29,30]. The fabrication process of this device allowed tuning of platinum nanosphere density along the length of the swCNTs. The goal of our research was to determine whether simulations of a dynamic model of the sensor could be used in place of experiments to find the optimal nanosphere density for maximal sensitivity and sensing range of the device [28].

1.3.2 Gap GRN Inference with a 3D Model of the *Drosophila*

melanogaster Embryonic Blastoderm

The fruit fly *Drosophila melanogaster* has been a model organism in genetic studies for over one hundred years[109]. With the expansion of molecular methods over the past thirty years, *Drosophila* has become a popular organism for molecular dissection of early developmental processes [110-136]. Early embryonic development, during which morphogen (transcription factor) transport occurs in a syncytial cytoplasm, has proven amenable to mathematical modeling [137-140]. One developmental system active during this syncytial phase of blastoderm growth is the gap gene system, named for the “gaps” or missing body segments seen in mutants in later embryonic stages. The gap genes regulate each other’s expression to form complex morphogen expression patterns along the anterior-posterior (AP) axis of the embryo; these patterns govern later body plan development.

Initial gap gene expression takes positional cues from anisotropic maternal mRNAs and their resultant protein products (transcription factors)[141]. The maternal anterior determinant, Bicoid (Bcd), is expressed from anteriorly distributed mRNA and forms a

decreasing concentration gradient from the anterior to posterior of the embryo [113]. Though Bcd has been studied since the 1980s[113,114,117,126,142-145], mathematical modeling of its gradient formation is a more recent enterprise [126,137,142,146,147]. These early models represented the AP axis of the embryo as a 1D line. The anterior end of the line was a point source for Bcd production and expressed protein would diffuse toward the posterior. To avoid saturation of the AP axis with accumulating Bcd, Bcd degradation was modeled by a first order decay term[126,142]. Collectively, these source-diffusion-decay (SDD) models were numerically easy to calculate and contained parameters with explicit biophysical meanings (*e.g.*, diffusion constants). The models replicated the stationary Bcd gradient observed in data, though the time required to reach this state did not agree with comparable experimental time course observations. These discrepancies prompted further model development. Ibanez and Belmonte provide an excellent review of these SDD modeling approaches [148].

Recent experimental and modeling work has discarded the passive and stationary mRNA hypothesis and considers the simultaneous behaviors of both RNA and morphogen [149]. Spirov *et al.* consider a number of mechanisms by which *bcd* mRNA may be degraded and transported so as to modify the Bcd gradient [150]. In a complementary study, Cheung *et al.* consider the dependency of Bcd production on the embryonic volume (hence, the absolute mRNA amounts) at points along the AP axis [151]. These models are capable of replicating a greater range of behaviors found in experiments, but at the cost of greater model complexity and difficulty matching model behavior to biological activity.

Though Bcd is relatively simple to model, it is vital for the establishment of the gap gene patterning. The gap genes require considerably more complex modeling approaches and are discussed in Chapters 3 and 4.

Modeling has played a large role in the evaluation of the *Drosophila melanogaster* gap gene system. Driven in part by maternal genes such as Bcd, this system of genetically interacting transcription factors forms specific expression bands along the fly embryo's anterior-posterior axis [141]. First experimentally characterized in the 1980s, decades of experimental work have resulted in a wealth of data with which to fuel model-driven discovery [118,122,152-156]. Varied modeling approaches have been applied to this system in the last two decades, each presenting different challenges to model fitting.

Early models (*e.g.*, Sanchez and Thierry [125]) incorporated pre-defined GRNs inferred from expert interpretation of mutant data rather than using parameter estimation to infer GRNs. To compensate for contemporary computational limitations, these simulations frequently incorporated simplifying assumptions such as discrete protein levels, discrete spatial domains, and discrete time updates. The qualitative nature of the model output limited error calculations; protein data might be classified as high, low, or absent and compared to similar model output.

The work of Jaeger *et al.*[138,139] initiated quantitative modeling for the purpose of GRN inference via parameter estimation. This approach led to numerous analyses [140,157-163], but also brought new challenges to model fitting and parameter identification. Building on the partial differential equation simulation methods of

Mjolsness and Reinitz[137], these models moved gap genes from discrete time and concentration simplifications to simulation of continuous concentrations and time on a 1D domain. Rather than building a model with assumptions about the nature of GRN interactions, Jaeger *et al.* built a general model framework in which every gene had the potential to enhance or inhibit the expression of every other gap gene. By minimizing the unscaled sum of squared error between model, they then fit the model to immunofluorescence expression data and observed which optimized GRNs replicated the observations most closely. This approach generated a set of similar GRNs that recapitulated expression patterns and agreed with genetic interactions previously proposed from mutant data. While the computationally inferred GRNs are consistent with expectations, a major shortcoming remains: When gap genes were knocked out in simulations of published gap gene models, the resulting protein distributions did not match available mutant data.

In conjunction with GRN inference studies, this model framework has been used to determine the sufficiency of proposed biological mechanisms. Proposed by Waddington in 1942, the canalization model refers to the reduction of cell potency (*i.e.*, from totipotency to unipotency) over the course of development [164]. To determine whether the gap gene interactions could account for this behavior, Manu *et al.* applied the mathematical formalism of dynamic attractors to a simplified version of Jaeger's model [161]. Much as physical objects are attracted to the stable position at the bottom of a gravity well, this analysis identifies stable equilibria to which dynamic models are "attracted" [20]. Their findings and experimental data suggest that canalization did occur

in the system; the interaction of gap genes led to protein band expression regions with less spatial variability than their upstream maternal regulators [161]. Bieler *et al.* constructed a model on a 3D domain [165]. Unlike the Jaeger family of models, their model included explicit representations of mRNAs and a transcription factor dimerization mechanism. This model also served to confirm the prevailing GRN inferences predicting mutual inhibition among gap genes. Like previous 1D models, both 3D models are insufficient to recover mutant phenotypes. This may be indicative of a missing component (or components) in the current models/hypotheses.

All of the preceding models (except the early discrete variants) attempt to fit 25+ parameters; this high-dimensional parameter space may lead to two related problems: over fitting and non-unique solutions. In statistical models, over fitting refers to overly parameterized models which predict noise rather than underlying trends [36]. Similarly, over fitting of dynamic models involves the distribution of error among many parameters during fitting; this may lead to spurious inferences from parameter estimation. While parameter estimation seeks the global optimal point – the best possible fit in the parameter space – high dimensional parameter spaces may contain many local optimal parameter sets which produce equivalent fits (**Fig. 1.1**). Indeed, when two parameters affect the same model output (*e.g.*, when two genes A and B enhance a target gene C), the parameters regulating $A \rightarrow C$ and $B \rightarrow C$ are said to be correlated and unique parameter values will not be identifiable [39,166]. Because Jaeger *et al.*'s approach allows all gap proteins to interact (thus estimating 36+ regulatory parameters), there is no guarantee of the uniqueness of estimated parameters and over fitting may occur. Fomekong-Nanfack

et al. found that it was impossible to distinguish between activator or repressor activity in fitting results because of parameter correlation [157,160]. The sensitivity analysis of Bieler *et al.* also indicates correlation among model parameters, limiting the scope of model inference [165].

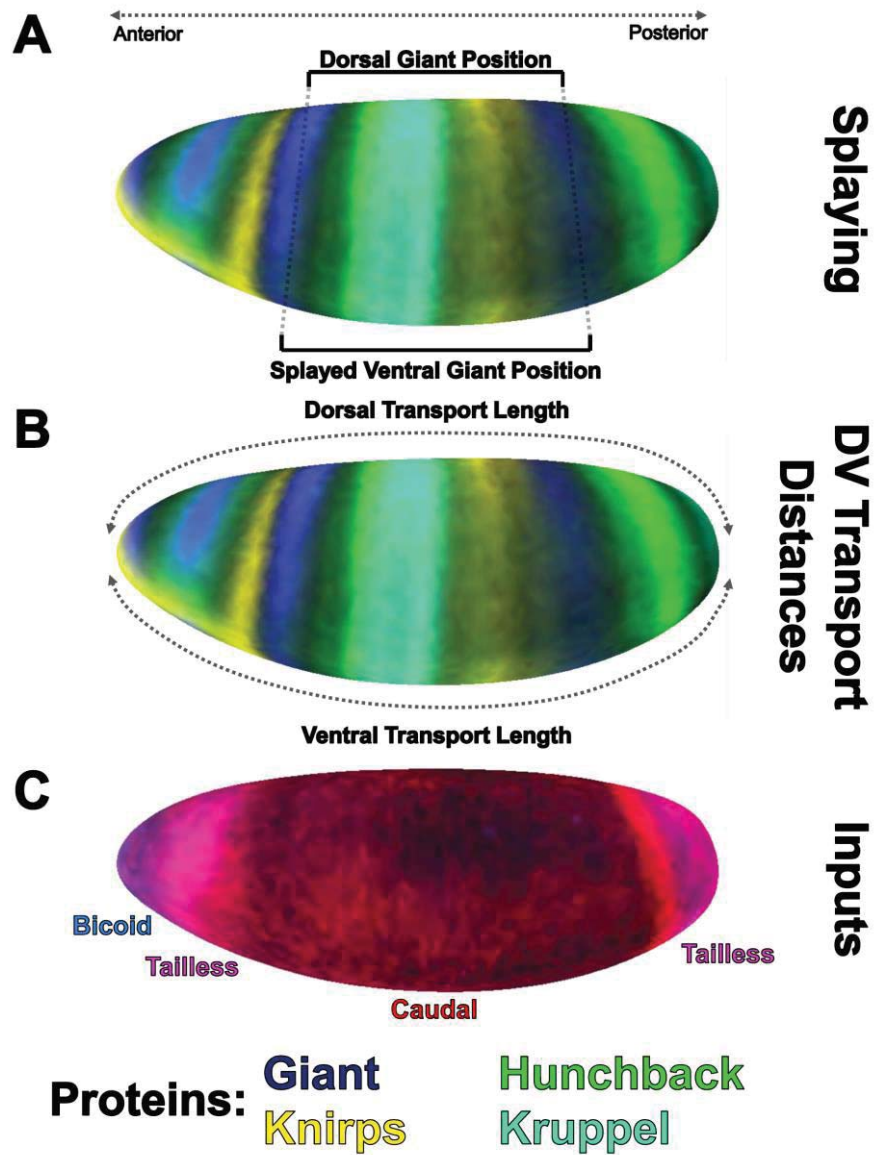


Figure 1.2 Dorsal-Ventral Patterning Asymmetries in the *Drosophila* Embryo

A-C present lateral views of the *Drosophila* blastoderm. The “splaying” phenomenon is represented in A; expression bands are closer together on the dorsal surface and farther on the ventral surface. Giant (blue) is highlighted as an example. B illustrates the difference in mass transport path lengths. Diffusion is limited to a thin layer along the embryo surface, which creates a longer ventral path relative to the dorsal path (B). DV asymmetric inputs (C) and initial conditions may also contribute to asymmetries in expression patterns. (Generated using the PointCloudXplore software[167].)

Extant gap gene models, as with all dynamic models, are necessarily incomplete abstractions of reality. Although it determines the AP axis of the fruit fly embryo, gap genes also show differences in patterning along the dorsal-ventral (DV) axis, notably “splaying” or distancing of protein bands toward the ventral side of the embryos (Fig. 1.2a). In Chapter 3, we built upon Jaeger *et al.*’s modeling approach to create a 3D model domain. We sought to determine whether embryo shape (Fig. 1.2b) and DV-asymmetric inputs (Fig. 1.2c) were sufficient to induce observed DV asymmetries and whether the additional 3D data could further constrain GRN estimation and allow estimation of new parameter sets[162]. We found embryonic geometry insufficient to explain DV gap patterns, and additional GRN inference proved inconclusive.

1.3.3 Characterizing the Effects of Objective

Function Choice on Estimated Parameters

As noted above, parameter estimation via optimization algorithms requires an objective function to assign quantitative output error values to parameter sets. These quantitative error values allow parameter sets to be sorted according to their goodness-of-fit.

However, the concept of a “good fit” is subjective; which features of model output constitute a good fit is dependent on how the research question is posed. For example, a medical model built to predict optimal drug delivery must reduce errors to safe, clinically acceptable levels. A good fit for a model built to capture qualitative aspects of a system (*e.g.*, the presence or absence of a protein expression band at a particular position along a *Drosophila* embryo) is less constrained; however, this scenario requires selection of an objective function that adequately captures investigators’ qualitative definitions of

“presence” and “absence”. Despite the context-dependence of goodness-of-fit, much of the biological modeling literature reports use of the sum of squared error (SSE, summing the squared value of error between each datum and its simulation) or its variants. In the case of *Drosophila* gap gene patterning – and more widely in models where a good fit depends on qualitative spatial trends – the SSE’s emphasis on pairwise errors may cause it to miss good qualitative fits that have poor numerical agreement (*e.g.*, matching spatial patterns of different magnitudes).

A large body of work is devoted to the selection and development of procedures for parameter optimization[38]. Though these procedures depend upon an objective function to rank parameter sets, few computational biologists have characterized the effects of objective function choice when precise quantitative agreement is not a criterion for a good fit.

It should be noted that the preceding two case studies have utilized or variants of the SSE measure (*e.g.*, root-mean-square-error or weighted SSE). This proved adequate in the case of biosensor design optimization, but may have been insufficient to recover new parameter sets in the gap gene patterning study. In particular, we observed qualitatively bad fits (simulated gap gene distributions that were dissimilar to data distributions) that had SSE error values on par with previously determined good fits. This indicated that objectives which sum individual errors might be inappropriate to capture the important qualitative features of the data. The limitations of these measures in fitting relative spatial positioning data (such as adjacent gap genes) will be discussed in Chapter 4.

1.4 Brief Outline

In the Chapter 2, I expand on a prior publication in which we develop a model of a glucose-detecting nanoscale biosensor and use the model to optimize the biosensor design for increased glucose sensitivity[28]. I set out to determine whether a dynamic model of the biosensor, once fit to data via parameter estimation, could successfully suggest optimized sensor designs. I evaluated the success of this process by fabricating the optimized designs and evaluating their glucose sensitivity relative to the original sensor. I also compare the new sensor's sensitivity to the simulation of the optimized biosensor architecture. I found an increase in sensor sensitivity and agreement with the simulated optimized sensor.

In Chapter 3, I discuss a three dimensional (3D) reaction diffusion model of gap gene patterning in the syncytial embryo of the fruit fly *Drosophila melanogaster*. The gap genes are so named because gap mutants have “gaps” between segments in later stages of development. The gap genes are spatially heterogeneous, early-expressing transcription factors that modulate each other's expression to form sequential expression bands along the anterior-posterior (AP) axis of the embryo, though some dorsal ventral (DV) asymmetries are present. [141]. Experimental observations have been insufficient to completely characterize the GRN governing gap gene interactions. Jaeger *et al.* pioneered a 1D model-based GRN inference approach that assigned parameters to all possible interactions and optimized those parameters to bring the model into agreement with data. Building on this body of work, I applied Jaeger's approach to a 3D embryonic geometry and asked whether geometry and/or DV-asymmetric initial conditions are

sufficient to explain observed final DV asymmetries. I also constrained Jaeger *et al.*'s inferential parameter estimation with additional spatial data. I found that neither realistic geometry nor 3D initial conditions were sufficient to explain the DV gap gene patterns. Counterintuitively, the additional data did not lead to inference of new GRNs. Inferred GRNs were qualitatively similar (*i.e.*, having the same enhancing and inhibiting interactions) to those reported by Jaeger *et al.* The successful parameter estimation for the biosensor and the poor estimation for the gap gene model led us to consider the effects of the error metric used to measure the goodness-of-fit between model and data; these are outlined in Chapter 4.

Chapter 4 describes another study of the gap gene system. Here, I reduced the model to one spatial dimension, the AP axis. Because parameter estimation is a form of optimization that minimizes error between data and model, I asked how the choice of objective function (quantifying error) affects the optimization process and the final estimated parameter set. I consider traditional objectives such as sum of squared error, intrinsic scaling metrics such as cosine distance, and metrics typically applied to probability distributions. I also suggest a workflow for improved parameter estimation of semi-quantitative spatial data and choice of objective function.

In Chapter 5, I review the key findings from the preceding case studies. In light of our inability to recover qualitatively novel GRNs (those with new patterns of inhibition and enhancement) during parameter estimation of the *Drosophila* gap gene system, the wide variety of inferred GRNs reported by others, and the inability of reported GRNs to

duplicate mutant phenotypes, I address the current lack of model validation in the gap gene modeling literature. To address the computational bottleneck of searching the high-dimensional GRN search space, I propose a time- and space-discretized model with a discrete parameter space. This model framework avoids several computational challenges described in this text: it has a smaller, completely-searchable parameter space and is easier to interpret. However, it is further removed from biological reality and must be further evaluated for computational artifacts arising from the discretization. I conclude with preliminary simulated data from this discrete framework.

CHAPTER 2. OPTIMIZATION OF A NANO-STRUCTURED GLUCOSE
BIOSENSOR DESIGN TO MAXIMIZE GLUCOSE SENSITIVITY

PUBLICATION

Claussen, J. C., Hengenius, J. B., Wickner, M. M., Fisher, T. S., Umulis, D. M., Porterfield, D. M. (2011) Effects of Carbon Nanotube-Tethered Nanosphere Density on Amperometric Biosensing: Simulation and Experiment. *Journal of Physical Chemistry C* 115: 20896-2090.

Effects of Carbon Nanotube-Tethered Nanosphere Density on Amperometric Biosensing: Simulation and Experiment

Jonathan C. Claussen^{1,2,3,†}, *James B. Hengenius*^{4,†}, *Monique M. Wickner*^{1,3}, *Timothy S. Fisher*^{1,5}, *David M. Umulis*^{2,3,6,*}, *D. Marshall Porterfield*^{1,2,3,6,*}

¹Birck Nanotechnology Center, ²Bindley Bioscience Center, ³Department of Agricultural and Biological Engineering, ⁴Department of Biological Sciences, ⁵School of Mechanical Engineering, ⁶Weldon School of Biomedical Engineering, Purdue University, West Lafayette, IN 47907

[†]Authors contributed equally to this work

*Corresponding authors' emails: dumulis@purdue.edu & porterf@purdue.edu

Corresponding Authors:

David M. Umulis

Purdue University

Department of Agricultural & Biological Engineering

225 South University Street

West Lafayette, IN 47907-2093

Phone: (765) 494-1223

Fax: (765) 496-1115

E-mail: dumulis@purdue.edu

D. Marshall Porterfield

Purdue University

Department of Agricultural & Biological Engineering

225 South University Street

West Lafayette, IN 47907-2093

Phone: (765) 494-1190

Fax: (765) 496-1115

E-mail: porterf@purdue.edu

ABSTRACT

Nascent nanofabrication approaches are being applied to reduce electrode feature dimensions from the microscale to the nanoscale—creating biosensors that are capable of working more efficiently at the biomolecular level. The development of nanoscale biosensors has been driven largely by experimental empiricism to date; consequently, the precise positioning of nanoscale electrode elements is typically neglected, and its impact on biosensor performance is subsequently overlooked. Herein we present a bottom-up nanoelectrode array fabrication approach that utilizes low-density and horizontally oriented single-walled carbon nanotubes (SWCNTs) as a template for the growth and precise positioning of Pt nanospheres. We further develop a computational model to optimize the nanosphere spatial arrangement and elucidate the tradeoffs among kinetics, mass transport, and charge transport in an enzymatic biosensing scenario. Optimized model variables and experimental results confirm that tightly packed Pt nanosphere/SWCNT nanobands outperform low-density Pt nanosphere/SWCNT arrays in enzymatic glucose sensing. These computational and experimental results demonstrate the profound impact of nanoparticle placement on biosensor performance. This integration of bottom-up nanoelectrode array templating with analysis-informed design produces a foundation for controlling and optimizing nanotechnology-based electrochemical biosensor performance.

KEYWORDS: multi-scale modeling, simulation, carbon nanotubes, Pt nanospheres, nanoelectrode arrays, biosensor

1. Introduction

The application of nanotechnology to nanoscale electrode design has been widely practiced across numerous biological and chemical disciplines.[168-172] Characteristics of nanoelectrodes including favorable Faradic-to-capacitive current ratios, fast response times, and high current densities have significantly enhanced the detection limit and resolution of electrochemical biosensors.[74,173,174] In general, these findings can be attributed to improved catalytic and mass transport properties associated with the electrode material, surface structure, and geometry.[59,175,176] Noble metals commonly used in nanoelectrode fabrication (*e.g.*, Pt, Pd, and Au) act as excellent heterogeneous catalysts and are resistant to corrosion and oxidation.[177] The catalytic nature of these bulk materials are enhanced at the nanoscale, as decreasing size increases the reactive surface area and qualitatively changes the electronic structure by quantum confinement.[178] Nanoelectrodes also experience enhanced mass transport of target species by radial diffusion, further contributing to their favorable electrochemical response.[179] However, nanoscale electrodes for sensing have been developed primarily through experimental empiricism, and a pressing need exists to improve both the controllability of nanoscale morphologies and the associated analysis-driven design procedures to optimize performance.

A major drawback to nanoelectrodes is the reduction in current due to overall low electroactive surface area. Large, high-density arrays of conducting nanoelectrodes separated by non-conducting oxide are often employed to overcome this drawback, substantially increasing the total generated electrode current.[180,181] Consequently,

biosensor performance is intimately affected by the packing density of these nanoelectrode arrays. Overlapping diffusion fields from tightly packed neighboring nanoelectrodes can impede incident transport of electroactive species, while low electroactive surface area in loosely packed arrays can reduce heterogeneous charge transport.[182] Hence, a balance between electrode spacing and electroactive surface area must be achieved for optimal nanoelectrode array design.

Precise positioning of metal nanoparticles on electrode surfaces to produce nanoelectrode arrays is challenging. Many techniques have been employed to create various types of ordered and random arrays of nanoelectrodes. Ordered nanoelectrode arrays often utilize e-beam lithography or ion-beam milling to expose nanosized metallic disks embedded under non-conducting oxide.[63,183,184] However, these techniques typically are expensive, usually restricted to specific material systems, and limited to serial processing.[185] Likewise, securing random arrays of metal nanoparticles to electrodes involves several formidable challenges. Current strategies such as physiochemical adsorption and covalent bonding have been developed to randomly cast premade nanoparticles onto electrode surfaces for biosensor applications.[186,187] However these top-down nanoparticle/electrode fabrication strategies generally offer little control over nanoparticle placement while requiring extensive chemical processing steps.

Perhaps the most promising methods of securing metal nanoparticles to electrode surfaces is through deposition on carbon nanomaterial substrates. Recently carbon nanomaterial-based electrodes from carbon nanotubes (CNT)[29,188,189] to exfoliated

graphite nanoplatelets[190] and graphene composites[191] have been used as highly conductive templates for metallic nanoparticle immobilization and subsequent biosensing applications. In this report, we build upon this work by developing glucose biosensors from networks of single-walled carbon nanotubes (SWCNTs) and platinum nanospheres with the assistance of computational modeling. We seek to understand the relationship between nanoparticle density and biosensor sensitivity.

Herein, we present an entirely bottom-up approach for nanoelectrode array fabrication in which single-walled carbon nanotubes (SWCNTs) grown from the surface of the electrode act as support structures for subsequent Pt nanosphere growth through electrodeposition—obviating the need for expensive lithographic techniques and laborious chemical processing steps. The Pt nanospheres act both as sites for heterogeneous charge transport and as docking points for biorecognition agents, while the SWCNTs act as highly conductive electrical wires that connect in parallel the network of Pt nanospheres. The nanoelectrodes are transformed into glucose biosensors by forming alkanethiol self-assembled monolayers (SAMs) on the nanospheres for subsequent conjugation with the enzyme glucose oxidase (GOx). These Pt nanosphere/SWCNT biosensors build upon previous electrode designs involving electrodeposited Pd nanocubes[192] and Au coated Pd nanocubes[29] on SWCNTs, however in this study, we demonstrate both the ability to alter the packing density of Pt nanospheres along each SWCNT and to correlate the effects of nanosphere density on amperometric biosensing through computational and experimental results.

Though nano-electrodes have found application in a variety of fields, the quantitative understanding of enzymatic kinetics and spatial effects of nano-electrode placement remains incomplete. Previous work has explored analytical solutions to mass transport equations for arrays of micro or nanoelectrode arrays.[179,193] Others have built numerical models of oxidation and mass transport with enzymatic conversion of analytes to an electrically active form for electrodes of various sizes.[194-197] We build upon this body of work to develop a multiscale numerical reaction-diffusion model that utilizes enzymatic and transport principles to predict the biosensor current response based upon the spatial arrangement of the nanoparticles immobilized on the biosensor surface.

Several key features distinguish our model from those previously mentioned in the literature, notably a probabilistic spatial distribution of random nanoelectrode arrays and the coupling of enzyme kinetics with mass transport. The probabilistic spatial distribution of nanospheres along SWCNTs creates unique diffusional microenvironments defined by glucose competition with neighboring nanospheres. Thus nanosphere current is dependent on microenvironment; we simulate total biosensor current by integrating nanosphere current over this spatial distribution to acquire biosensor scale properties from the cumulative contributions of nanoscale phenomena. This reaction-diffusion model is subsequently used to optimize the Pt nanosphere packing density along individual SWCNT strands by analyzing the mass transport of analyte, enzymatic reaction kinetics, and electrochemistry within the nanosphere domain. The simulated biosensor current displayed by the model is fit to experimental glucose sensing data and utilized to predict a more favorable nanosphere packing density for glucose

sensing. This prompted the development of arrays with closely packed Pt nanospheres—a device with regularly spaced SWCNTs coated with spherical Pt segments that promotes optimal signaling capability in terms of both sensitivity and linear sensing range.

2. Experimental Section

2.1. Reagents. Glucose oxidase (GOx, *Aspergillus niger* lyophilized powder, 100,000-250,000 units/g without added oxygen, stored at 4 °C, 50KU, G7141), 11-mercaptoundecanoic acid (MUA, 95%, 450561), 2-(N-Morpholino)ethanesulfonic acid (MES, ≥99% titration, 50G, M3671), N-Hydroxysuccinimide (NHS, 98%, 25G, 130672), 1-[3-(Dimethylamino)propyl]-3-ethylcarbodiimide methiodide (EDC, 10G, 165344), hydrogen peroxide (H₂O₂ 30% (w/w) in H₂O, stored at 4°C), chloroplatinic acid hexahydrate (H₂PtCl₆·6H₂O, ≥ 37.50% Pt basis, 1G), sodium sulfate (Na₂SO₄, ≥99.99% trace metal basis, 10G, 204447) were obtained from Sigma Aldrich. Phosphate buffered saline (PBS, 0.1 M, pH 7.4, 10010072) was obtained from Invitrogen Corporation. Oxalic acid dihydrate (ACS, 99.5 – 102.5%, 250g, 33262) and sulfuric acid (H₂SO₄, 93 – 98%, 500mL, 38751) was obtained from Alfa Aesar.

2.2. SWCNT Template Fabrication. By following our previous fabrication protocols, a porous anodic alumina (PAA) substrate is developed for subsequent SWCNT synthesis.[29,192,198] In order to create the PAA template, a thin film metal stack [Ti (100 nm), Al (100 nm), Fe (1 nm), and Al (400 nm)] is e-beam evaporated on an oxidized silicon wafer [P <100> Si (5 μm), SiO₂ (500 nm)] at a base pressure of 5.0×10^{-7} Torr. The metalized substrate is subsequently anodized by immersion in 0.3 M oxalic acid

(1.5°C) while being biased with 40 V versus a Pt gauze auxiliary electrode. The anodization process creates semi-ordered pores (20nm dia.) that extend through the Al/Fe/Al layers to the Ti layer (the bottom electrical contact for the electrode) and converts the Al layers into the dielectric Al₂O₃. Additionally, an electrically conductive contact pad comprised of the evaporated metals is created for subsequent electrochemical processing and biosensing by leaving a portion of the sample un-anodized.

2.3. SWCNT Synthesis. Arrays of SWCNTs are grown from the Fe catalyst embedded within the pores of the PAA by a microwave plasma chemical vapor deposition (MPCVD) technique that utilizes a SEKI AX5200S MPCVD reactor. The anodized substrate is placed in the reactor on a 5.1 cm diameter molybdenum puck and heated by a 3.5 kW radio-frequency power supply to 900°C in a hydrogen ambient. Subsequently, a hydrogen plasma is generated over the sample via a 5 kW ASTeX AX2100 microwave generator, and methane (CH₄) gas, the acting precursor for carbon nanotube (CNT) growth, is introduced into the chamber for 10 minutes. The hydrogen plasma decomposes the methane gas to permit CNT growth and penetrates the oxide layer at the base of the pores of the PAA. The 10 minute plasma/methane reaction creates SWCNTs, 10 – 50 μm in length, that extend vertically from the pores of the PAA and eventually come to rest horizontally on the PAA surface.

2.4. Pt Nanosphere Formation. A 3-electrode set-up (BASi Epsilon Cell Stand) is utilized to electrodeposit Pt nanospheres at the defects sites of SWCNTs. The SWCNT electrodes act as the working electrode, Ag/AgCl as the reference electrode, and Pt gauze

as the auxiliary electrode. The three electrodes are submersed within a 20ml metal salt bath consisting of 4 mM $\text{H}_2\text{PtCl}_6 \cdot 6\text{H}_2\text{O}$ in 0.5 M Na_2SO_4 . In order to create the low-density Pt nanosphere/SWCNT electrodes, pulsed electrical currents of 2 mA/cm² (Pt electrodeposition) with a frequency of 500 ms were applied between the working and auxiliary electrodes for 250 cycles. The high-density Pt nanosphere/SWCNT electrodes were created in exactly the same manner with one exception, the pulsed electrical current was changed to 8 mA/cm². These Pt electrodepositions create an electrical back contact to the SWCNTs by partially filling the pores of the PAA and electrically connecting the Ti bottom layer and the SWCNTs, while Pt nanospheres (150 nm dia.) grow concentrically around the exposed SWCNTs (**Fig. 1**).

2.5. Enzyme Immobilization. The formation of SAM alkanethiols on the electrodeposited Pt nanospheres was carried out by following similar protocols established for SAM formation on Au and Pt surfaces.[199,200] The electrodes were electrochemically cleaned by cycling the potential from -0.5 to 1.0 V in 0.3M H_2SO_4 and subsequent washing in ethanol and nanopure water and finally drying under a gentle stream of N_2 gas. The electrodes were exposed to H_2SO_4 for no longer than 10 minutes to avoid oxidative cutting of the SWCNTs.[201] The SAM layer was formed by immersing the electrodes in an ethanol solution containing 10 mM 11-mercaptoundecanoic acid (MUA) for 24 hours. The electrodes were subsequently rinsed thrice in ethanol to remove any unbound thiol. Carbodiimide chemistry was employed to activate carboxylic acid groups within the SAM layer for subsequent linking with enzyme by immersing the electrodes in a 0.1M MES acid with 15 mM NHS and 75mM EDC for 2 hours. Finally

the electrodes were rinsed thrice in 0.1M PBS and immersed in individual test tubes containing 0.1M PBS with 2mg/mL GOx and placed in a test-tube shaker for 2 hours. After the enzyme immobilization process the electrodes were rinsed thrice in nanopure water to remove unbound enzyme and subsequently stored in 0.1M PBS at 4°C prior to electrochemical experimentation.

2.6. Electrochemical Sensing. H₂O₂ concentration levels were monitored directly and via the enzymatic breakdown of glucose with a BASi C3 Cell Stand (3 electrode set-up). The low- and high-density Pt nanosphere/SWCNT biosensors were biased (600 mV) against a Ag/AgCl reference electrode in a phosphate buffered saline (PBS, 0.1 M pH 7.4) while a Pt wire acted as the auxiliary electrode. Electrical charge generated during electrochemical sensing flows through the Pt nanosphere/SWCNT matrix to the conducting Ti underlayer that is electrically wired to the cell stand. The theoretical detection limit was calculated by evaluating the experimental electrode current response three standard deviations from the arithmetic mean of the baseline signal (*i.e.*, signal-to-noise ratio [S/N] = 3).

2.7. Imaging. An S-4800 Hitachi microscope was utilized at a power setting of 5.0 kV to obtain the field emission scanning electron microscopy (FESEM) micrographs. Samples were imaged before the immobilization of the SAM/GOx enzyme layer and without any additional processing steps.

3. Results and Discussion

3.1. Biosensor Fabrication. The SWCNT networks are fabricated in situ from a porous anodic alumina (PAA) template embedded with a catalytic Fe layer and developed from an oxidized silicon wafer (**Fig. 1**). The SWCNTs grow from an Fe catalyst layer embedded within the pores of the PAA through a microwave plasma chemical vapor deposition (MPCVD) process and subsequently come to rest horizontally on the surface of the PAA. Pt nanospheres are subsequently electrodeposited onto the SWCNTs to enhance the electrocatalytic properties of the sensor[202,203] and to serve as docking points for enzyme immobilization through thiol linking.[200] The average inter-nanosphere spacing on each single SWCNT strand was 366 nm ($\sigma = 362$ nm) while an average spacing between each SWCNT strand was 8.0 μm ($\sigma = 6.1\mu\text{m}$). Details of the biosensor fabrication are included in the **Experimental Section**.

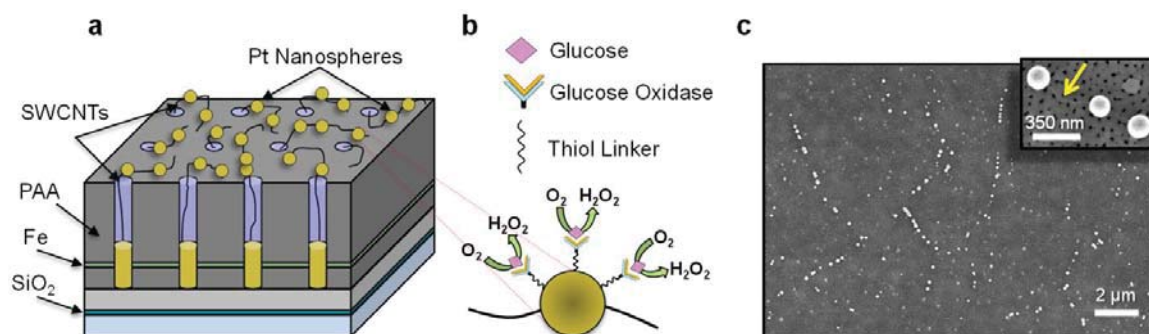


Figure 1. (a) Tilted cross-sectional schematic illustrating the Pt nanosphere-augmented SWCNT electrode with (c) corresponding top-view field emission scanning electron microscopy (FESEM) micrograph. (b) Biofunctionalization schematic demonstrating the covalent linking of the enzyme glucose oxidase to the Pt nanospheres for subsequent glucose biosensing. Glucose binds within the GOx enzymatic pocket producing H_2O_2 while consuming O_2 . FESEM micrograph inset (c) portrays a magnified view of a single Pt nanosphere decorated SWCNT with the yellow arrow pointing to an undecorated portion of the SWCNT. Note: schematics are not drawn to scale.

3.2 Model Development. To improve biosensor performance, reaction-diffusion models of the biosensor were developed to optimize the design and to understand the tradeoffs between transport-limited processes and reactions on the Pt nanospheres. First, a single Pt nanosphere electrode model simulated glucose flux to and oxidation at Pt nanospheres. Individual nanospheres were simulated under conditions mimicking different microenvironments on the biosensor surface while the total biosensor current was simulated by computing a weighted sum of these individual nanosphere currents.

Before simulating the total biosensor current, we confirmed that the single-nanosphere model recapitulated theoretical predictions regarding diffusion-enhanced signal. A domain representing the volume around one nanosphere as it lies along a SWCNT on the biosensor surface simulated the biosensor environment (**Fig. 2**). We assumed that the SWCNTs were sufficiently separated so that a single nanosphere would experience bulk glucose solutions in all directions perpendicular to the SWCNT except at the alumina biosensor surface. The curved surface of the cylinder represents the interface with the bulk glucose solution; this geometry allows the analyte to diffuse radially to the electrode from the region around the SWCNT ensuring accurate model output while reducing computational cost of a larger domain. The governing equations and boundary equations associated with each model domain are presented as follows.

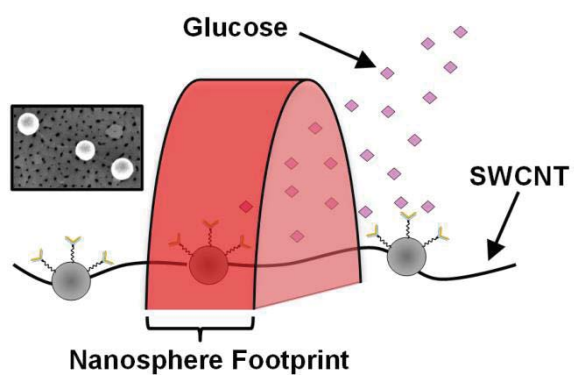
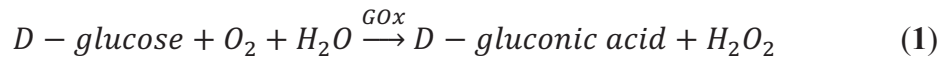


Figure 2. The model domain represents a volumetric “slice” of space (red hemicylindrical surface) along the Pt nanosphere-augmented SWCNT electrodes on the biosensor surface. The volume of the domain is proportional to the nanosphere footprint (*i.e.*, the sum of the nanosphere diameter and the average distance to the adjacent nanospheres).

3.2.1. Glucose Oxidase (GOx) Enzyme Function. Glucose biosensing depends on two chemical processes: enzymatic oxidation of glucose to gluconic acid and H_2O_2 and subsequent electrochemical oxidation of H_2O_2 at the electrode surface (producing measurable current). These two reactions (**Eq. 1** & **Eq. 2**) couple with diffusive transport to describe the amperometric sensing capabilities of the biosensor.



Though oxygen and oxidation byproducts play a role in these chemical reactions,[204,205] we assume that oxygen is in excess because the duration of glucose sensing experiments performed in this study is short (< 35 mins) and the solution volume in the testing vial (20 mL) is large compared to the size of the working electrode. Furthermore, the GOx enzymatic reaction is considered irreversible. We further assume that H_2O_2 , generated near the nanosphere surface, undergoes near-instantaneous oxidation. With these simplifying assumptions, we explicitly model the diffusion and enzymatic oxidation of glucose alone.

3.2.2. Glucose Diffusion and Enzymatic Oxidation. Mass transport of glucose throughout the domain is diffusive. Diffusion of glucose is represented by

$$\frac{d[Glucose]}{dt} = D_{glucose} \nabla^2 [Glucose], \quad (3)$$

where $D_{glucose}$ is the diffusion constant for glucose. The domain represents a transverse “slice” of the analyte solution around a single Pt nanosphere electrode (**Fig. 2**). We assume that the domain is a unit cell repeated along the length of the SWCNT where each nanosphere is equidistant from both adjacent neighbors on a SWCNT—permitting the use of periodic boundary conditions for the two semicircular faces of the domain. Zero-flux boundary conditions are imposed on these semicircular faces and on the insulating anodized alumina surface (*i.e.*, the surface on which the nanosphere rests). The glucose concentration is fixed at $[Glucose]_{bulk}$ at the outer edge of the domain (*i.e.*, the interface with the bulk glucose analyte). Finally, flux at the nanosphere surface contains several components. Glucose is consumed at this surface according to Michaelis-Menten enzyme kinetics,[195,206]

$$-\mathbf{n} \cdot \mathbf{N}_G = -V_{max} \frac{[Glucose]}{K_M + [Glucose]} \quad (4)$$

where \mathbf{n} is a normal vector perpendicular to the surface of interest, $\mathbf{N}_G = -D\nabla[Glucose]$ (*i.e.*, the diffusive flux of glucose at that point on the surface), V_{max} is the maximum glucose flux, and K_M is the glucose concentration at half maximum glucose flux (Michaelis-Menten constant) for the reaction. Similarly, the H_2O_2 flux at the nanosphere surface contains a Michaelis-Menten production flux and an oxidative consumption flux (J_{ox}),

$$-\mathbf{n} \cdot \mathbf{N}_H = V_{max} \frac{[Glucose]}{K_M + [Glucose]} - J_{ox} \approx -V_{max} \frac{[Glucose]}{K_M + [Glucose]} \quad (5)$$

where $N_H = -D\nabla[H_2O_2]$. On the assumption that J_{ox} dominates over diffusion of H_2O_2 away from the nanosphere, we simplify the model by making H_2O_2 consumption and production equal (*i.e.*, all H_2O_2 generated at the surface is effectively oxidized). Using this rate-limiting assumption, we are able to neglect an explicit representation of H_2O_2 within the model.

3.2.3. Simulated Biosensor Current Output to a Single Nanosphere Electrode. To quantify the current output of a single nanosphere electrode we computed the following surface integral over the nanosphere surface (denoted S):

$$I_{nanosphere} = \frac{2N_A \times 10^{-3}}{6.242 \times 10^{15} (e/C)} \int_{\partial\Omega} \frac{V_{max}[Glucose]}{K_M + [Glucose]} dS \quad (6)$$

where the integrand is oxidative H_2O_2 flux at the nanosphere surface (mM s^{-1}). The integral is multiplied by a constant that converts to units of Amperes. The factor 2 in the numerator represents the two moles of electrons that are produced per oxidation of one mole of H_2O_2 (**Eq. 2**) while $N_A \times 10^{-3}$ is Avogadro's number adjusted for millimolar concentrations. **Equation 6** quantitatively predicts the electron flux at a single nanosphere electrode surface (optimization metrics and parameter values are provided in the **Supporting Information**).

To model the range of nanosphere behaviors in different microenvironments, fifty model domains of varying lengths were constructed along the SWCNT axis (*e.g.*, **Fig. 3a & 3d**).

These variable lengths represent different inter-nanosphere spacing and by extension, different diffusion regimes. To generate model output for comparison to experimental data, the steady-state current response of all fifty domains was simulated at three experimentally measured glucose concentrations (10 μ M, 1mM, 15mM) (**Fig. 3b**). These single-nanoelectrode currents were computed for each glucose concentration according to **Equation 6**. The result – that current increases with radial diffusion – agrees with previous work [57,207-209], suggesting that radial analyte diffusion improves biosensor sensitivity.

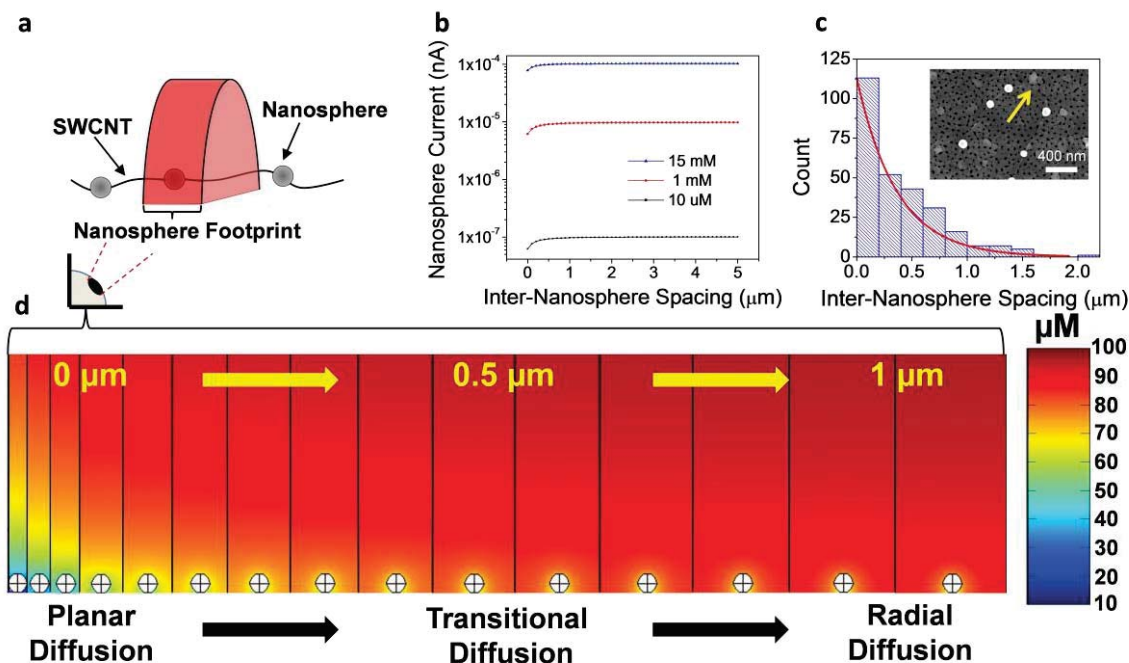


Figure 3. (a) The model domain represents a volumetric “slice” of space along the low-density Pt nanosphere-augmented SWCNT electrodes on the biosensor surface. The volume of the domain is proportional to the nanosphere footprint (*i.e.*, the sum of the nanosphere diameter and the average distance to the adjacent nanospheres). (b) The generated current for each nanosphere reaches a plateau during increasing inter-nanosphere distance while current increases for increasing concentrations of glucose. (c) The experimentally observed distribution of the low-density Pt nanosphere spacing along each SWCNT strand is displayed as the histogram. An exponential distribution (red line) with mean $\mu = 366$ nm and exponential parameter $1/\mu$ is fitted to the histogram. Inset FESEM micrograph displays spacing between nanospheres on a single SWCNT with yellow arrow pointing to an undecorated portion of the SWCNT. (d) Steady-state glucose concentration gradients (generated in COMSOL Multiphysics®) around a single nanosphere and perpendicular to the SWCNT strand with initial bulk glucose concentration of $100 \mu\text{M}$. Diffusion regimes change from planar to radial as distance between nanospheres on a SWCNT increases (see line of sight from cartoon eyeball).

3.2.4. Simulated Total Biosensor Current Output. The total simulated biosensor current was found by integrating the individual single-nanoelectrode currents (**Eq. 6**). The contribution of each domain to the total biosensor current is proportional to the number of electrodes experiencing that domain's local environment,

$$I_{total} \propto \sum_{i=1}^n w_i I_i \quad (7)$$

where I_{total} is the total biosensor current, n is equal to fifty (the number of domains), the weights (w_i) are the proportional contribution of electrodes in each microenvironment to the total biosensor current (*i.e.*, the fraction of nanospheres experiencing the environment), and I_i are currents from the model domains. The weight w_i is the area under the exponential curve for the i th domain normalized to the area under the entire curve and is proportional to the distribution of distances between nanospheres on each SWCNT. The experimental inter-Pt nanosphere distance data were best fit by an exponential function with a nearly equivalent mean ($\mu = 366$ nm) and standard deviation ($\sigma = 360$ nm) and decay constant ($1/\mu$) (**Fig. 3c**). The distribution of defect sites along a finite length of SWCNT (thought to be nucleation sites for nanoparticle formation [60]) are Poisson distributed where the length of intervals between Poisson-distributed nanospheres follows an exponential distribution.[210]

Total biosensor current is calculated by multiplying the right-hand side of the proportionality in **Equation 7** to the total number of Pt nanosphere electrodes on the biosensor surface. The total number of Pt nanospheres is acquired by dividing the total SWCNT length, approximated through image-analysis techniques (see **Supporting**

Information), by the average nanosphere footprint (*i.e.*, the length of nanotube occupied by each electrode, **Fig. 2**)

$$N_{total} = \frac{L}{\delta} \quad (8)$$

where L is the total length of SWCNTs and δ is the length of the average nanosphere footprint.

With this approximation of the total number of Pt nanospheres, the proportionality in **Equation 8**, can be modified as follows:

$$I_{total} = N_{total} \sum_{i=1}^n w_i I_i \quad (9)$$

Though **Equation 9** approximates the total biosensor current, we noted that the relationship between inter-nanosphere spacing and current increased in a smooth and monotonic manner—making current amenable to continuous interpolation. Similarly, the weights (w_i) are evaluations of the exponential distribution of inter-nanosphere spacing. Thus, to minimize numerical error, **Equation 9** can be cast as an integral,

$$I_{total} = N_{total} \int_{x_{space}=0}^{\infty} Exp(x_{space}^{-1}) I_{interp}(x_{space}) dx, \quad (10)$$

where $Exp(\cdot)$ is the exponential probability distribution, x_{space} is the inter-nanosphere spacing, \bar{x}_{space} is the average inter-nanosphere spacing, and $I_{interp}(\cdot)$ is the linear interpolant of simulated current performed in Matlab and shown in **Fig. 3b**. Using **Equation 10** in conjunction with simulated current, we approximated the steady-state current of the biosensor in response to each glucose concentration.

3.3. Model-based Biosensor Design. To evaluate the relative contributions of increased electroactive surface area and increased diffusive flux of analyte, the model was implemented over a range of glucose concentrations (100 μM – 86 mM) to obtain unweighted values of domain currents. Storing these unweighted current values, the shape parameter (\bar{x}_{space}^{-1}) of the inter-nanosphere distance exponential distribution was varied. The integral in **Equation 6** was then updated with an exponential parameter and the total nanospheres (N_{total}) for each distribution and subsequently the total biosensor output was evaluated according to **Equations 7-9**. Finally, the simulated biosensor current outputs for average nanosphere spacing ranging from 0 to 1 μm were plotted (**Fig. 4**).

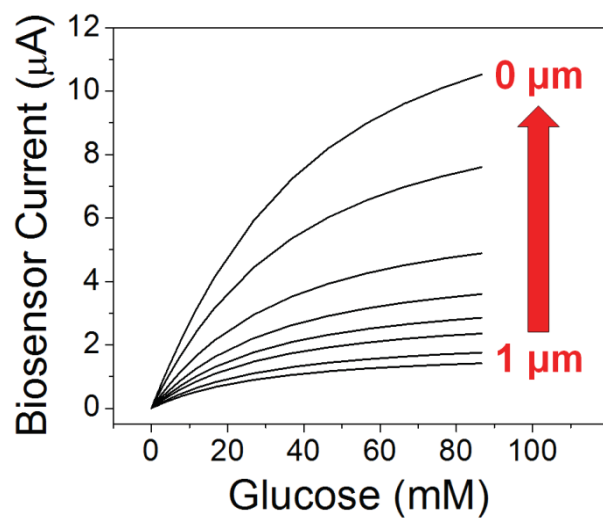


Figure 4. Simulated amperometric glucose response of the entire biosensor as a function of average inter-nanosphere spacing measured sphere edge to adjacent sphere edge. Total biosensor current monotonically increases as inter-nanosphere spacing decreases from 1 to 0 μm .

From these simulated results we observed that the total biosensor current is maximized when the Pt nanospheres are packed end-to-end along the SWCNT axis. These in silico findings suggest that the diminished electroactive surface area in the low-density Pt nanosphere/SWCNT biosensors reduces the overall biosensor current relative to the high-density Pt nanosphere/SWCNT biosensors. The signal reduction in the low-density Pt nanosphere/SWCNT biosensors occurs despite enhanced mass transport by radial diffusion between individual nanospheres along the axis of the SWCNTs (**Fig. 3b,d**). However the high-density SWCNT biosensors experience an enhanced signal due to both convergent diffusion and increased surface area. The SWCNT networks of these high-density Pt nanosphere/SWCNT electrodes are nearly completely coated with Pt—acting as nanoband electrode arrays where nanoscale widths are still maintained between SWCNTs. The inter-SWCNT distance of $8.0\ \mu\text{m}$ ($\sigma = 6.1\ \mu\text{m}$) falls above several popular nanoelectrode array spacing parameters (*e.g.*, $1\ \mu\text{m}$ spacing between nanoelectrodes or six [211] or ten [212] times the radius/width of the nanoparticle/nanoband)—ensuring the enhanced mass transport of glucose by convergent diffusion between each SWCNT strand. Therefore the high-density Pt nanosphere/SWCNT nanoband biosensors still experience enhanced mass transport from directions perpendicular to the SWCNT despite the apparent lack of enhanced mass between adjacent nanospheres along the axis of the SWCNT. Thus in the simulation, the current signal is dominated by incremental changes in surface area while the signal penalty incurred by inter-particle interactions is minimized—producing a biosensor current that increases monotonically with decreasing inter-nanosphere spacing (**Fig. 4**).

From these simulated results we observed that the total biosensor current is maximized when the Pt nanospheres are packed at maximal density. These *in silico* findings suggest that the lack of electroactive surface area in a low-density Pt nanosphere/SWCNT sensor, as compared to that of a high-density Pt nanosphere/SWCNT sensor, is sufficiently large to reduce the overall biosensor current despite enhanced mass transport by radial diffusion along the axial direction of the SWCNTs. Furthermore, the SWCNT networks of the high-density Pt nanosphere/SWCNT electrodes are nearly completely coated with Pt—thus acting as nanoband electrode arrays where nanoscale widths are still maintained. The inter-SWCNT distance of $8.0\ \mu\text{m}$ ($\sigma = 6.1\ \mu\text{m}$) falls above several popular nanoelectrode array spacing parameters (*e.g.*, $1\ \mu\text{m}$ spacing between nanoelectrodes or six [211] or ten [212] times the radius/width of the nanoparticle/nanoband)—ensuring the enhanced mass transport of glucose by convergent diffusion between each SWCNT strand.

3.4. Experimental Glucose Sensing with Low-density Pt Nanosphere Decorated

SWCNTs. Glucose sensing was performed by using a 3-electrode arrangement (BASi Epsilon Cell Stand) in a test vial containing 20 mL of phosphate buffer solution (PBS, pH = 7.4) while a potential of 600 mV was placed between the working and auxiliary electrodes. Details of the biosensor fabrication and testing protocols are provided in the **Experimental Section**. Generated current from the electrochemical oxidation of H_2O_2 (*i.e.*, the electroactive product of GOx/glucose, see **Eq. 1 & 2**) was monitored while successive glucose aliquots were added to the test vial to increase overall glucose concentration. Amperometric calibration and experimental detection limit graphs for the

low-density Pt nanosphere/SWCNT biosensor are illustrated in **Figure 5**. Two aliquots of PBS (0.1 M, pH 7.4) of equal volume to glucose aliquots were added to the test vial after glucose sensing in the detection limit plots—demonstrating current response originates from the glucose and not the saline buffer media itself (**Fig. 5b**, insets). The low-density Pt nanosphere/SWCNT biosensor experienced a linear glucose sensing range from 300 μM to 15mM and a theoretical glucose detection limit of 74 μM (S/N = 3). The glucose sensitivity of the entire biosensor was calculated to be 0.32 $\mu\text{A mM}^{-1} \text{cm}^2$.

3.5. Experimental Glucose Sensing with High-density Pt Nanosphere Decorated

SWCNTs. Finally, we verified the simulated current response of a high density Pt nanosphere/SWCNT biosensor (*i.e.*, where the Pt nanospheres are electrodeposited end-to-end along each SWCNT) through experimental testing (**Fig 5b**). The high-density Pt coated SWCNT nanoband arrays monitored glucose with a sensitivity of 0.69 $\mu\text{A mM}^{-1} \text{cm}^2$, linear sensing range of 100 μM to 20 mM, and a detection limit of 5.8 μM (S/N = 3). This concomitance of a low detection limit and wide linear range of the Pt/SWCNT nanoband arrays is an improvement upon similar CNT/Pt nanoparticle hybrid biosensors [213-217]—permitting the sensing of glucose in physiological fluids of saliva, tears, and blood (**Fig. 5c**).

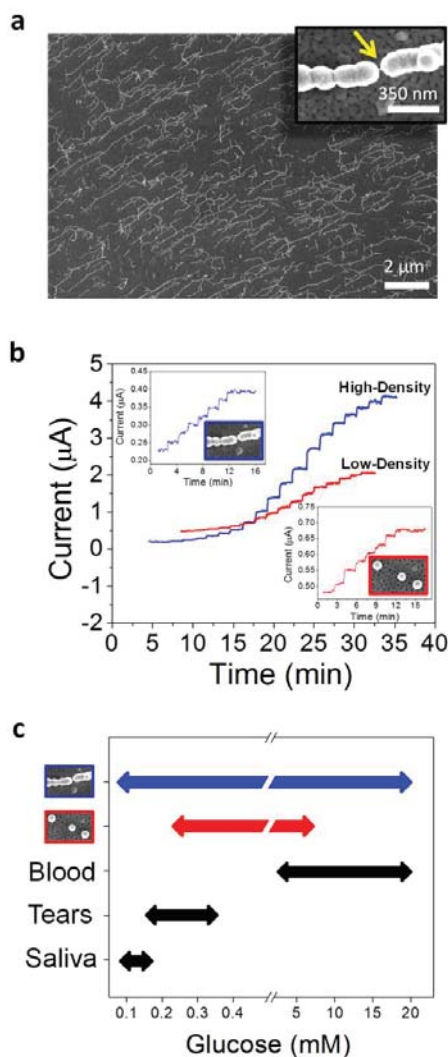


Figure 5. (a) FESEM micrograph illustrating a Pt nanosphere-augmented SWCNT electrode with high density Pt nanosphere packing. FESEM micrograph insets portray a magnified view of a single Pt nanosphere decorated SWCNT with the yellow arrow pointing to an undecorated portion of the SWCNT. (b) Experimental amperometric glucose calibration plots for the high-density (**blue**) and low-density (**red**) Pt nanosphere/SWCNT biosensors. (**blue-middle**) Current response for successive glucose concentration increases of 50 μM , 100-500 μM by 100 μM , 1-5 mM by 1 mM and finally 7 consecutive concentration increases of 10mM while insets show current vs. concentration profiles. (**red-middle**) Current response for successive glucose concentration increases of 100-500 μM by 100 μM , 1-5 mM by 1 mM and finally 6 consecutive concentration increases of 10mM while insets show current vs. concentration profiles. (**Insets**) Current response for 10 successive 20 μL glutamate injections resulting in incremental concentration increases of 100 μM (**blue**) and 300 μM (**red**) followed by two 20 μL injections of PBS (0.1M, pH 7.4). (c) Glucose sensing ranges of the low-density (**red**) and high-density (**blue**) Pt nanosphere/SWCNT biosensors as compared to glucose levels in three physiological fluids (blood,[51] tears,[48] and saliva[52]).

3.6. Model Verification. In order to test our hypothesis regarding biosensor current output and Pt nanosphere packing density we first optimized our computational model to fit the low-density Pt nanosphere/SWCNT nanoelectrode arrays (**Table S1** in **Supporting Information**). The subsequent optimized model was used to predict the generated current output of a high-density Pt nanosphere/SWCNT nanoband array. To compare the model output against the low-density biosensor, we used image-analysis software in MATLAB to identify the density and distribution of distances of individual Pt nanospheres (**Fig. S1** in **Supporting Information**). Using the best-fit parameter values obtained from the low-density model, the high-density Pt nanosphere/SWCNT sensor was simulated using the single domain schema detailed previously—recapturing the behavior of the biosensor current output (**Fig. 6**).

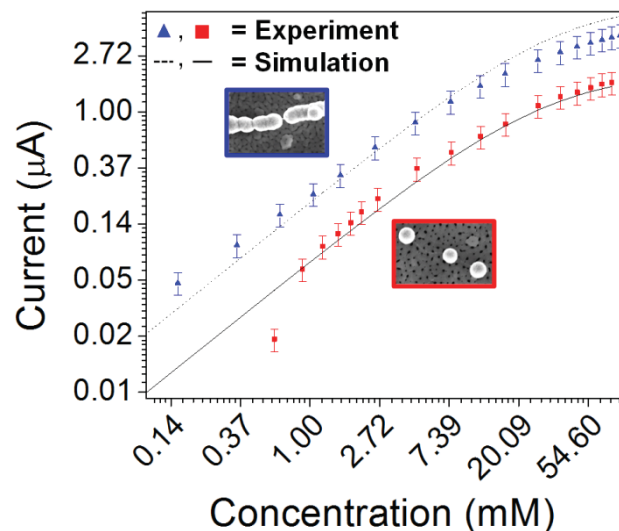


Figure 6. (a) Experimental and simulated amperometric glucose calibration plots for the high- and low density Pt nanosphere/SWCNT biosensors. Low-density biosensor data (**red squares**) was used to optimize model output (**solid black line**). The optimized model parameters were capable of recapitulating high-density biosensor data (**blue triangles**) shown by high density model output (**dashed black line**).

4. Conclusions

Networks of Pt nanospheres electrically interconnected by individual SWCNTs were created from a PAA template for electrochemical sensing applications. By altering the fabrication protocol according to computational modeling results, we increased the packing density of the Pt nanospheres along each SWCNT strand to improve the sensitivity, detection limit, and linear sensing range of the biosensor. The model was successfully used as a computational tool to improve biosensor performance, while reducing the excessive expenditures that are oftentimes required in ad hoc experimental design and fabrication.

This work builds upon the foundational research presented within the last decade that describes the mass transport properties of nanoelectrodes of various geometries and spatial arrangements [59,173,175,176,211]. We add to this foundational work by incorporating enzyme kinetics and charge transport in addition to mass transport to create a model capable of describing transport and oxidation on a random array of Pt nanospheres. Computational efficiency is achieved by simulating a limited number of nanospheres and integrating over the spatial distributions found on the biosensor array. This approach provides insight into the behavior of the system: where simulations indicate that a balance between electroactive surface area and inter-electrode spacing needs to be reached for maximal biosensor performance. The resulting model-inspired biosensor, with a tightly packed nanosphere arrangement, converts the biosensor from a NEA to a nanoband array—where generated electrochemical current signals are higher due to the increased electroactive surface area of the tightly packed Pt nanospheres and

fast radial transport to each nanoband due to the nanoscale widths. Future modeling work will focus on a generalization of our spatial integration scheme (**Eq. 10**) to include inter-SWCNT distance distributions in addition to inter-electrode distances. Such modifications to the model will be also useful in the design and development of patterned PAA through e-beam lithography.[184]

The hybrid nature of the SWCNT/Pt nanosphere arrays creates a unique platform that is advantageous for electrochemical biosensing due to the geometry and morphology of the SWCNTs and the Pt nanoparticle constituents. The embedded iron layer within the PAA matrix creates a template for the growth of low-density SWCNTs that extend horizontally on the surface of the PAA as opposed to high density growth of multi-walled carbon nanotubes.[218] These low-density horizontal lying SWCNTs rise above the surface of the PAA, due to their tethered nature, and accordingly allow for the concentric growth of nanoparticles at SWCNT defect sites including the “near spherical” Pt nanostructures presented in this work. Near spherical Pt nanostructures enhance charge transport during electrochemical sensing because they contain numerous facets with more interfacial surface atoms to catalyze reactions than those of other shapes (*e.g.*, cubical shapes).[219] Furthermore, the inter-SWCNT spacing ($8.0\ \mu\text{m}$, $\sigma = 6.1\ \mu\text{m}$) within a nonconducting template allows for the creation of nanoelectrode and nanoband arrays—electrode geometries that experience enhanced signal-to-noise ratios that are well suited for electrochemical biosensing. Thus the hybrid SWCNT/Pt nanosphere structures create a highly conductive network that is conducive towards 3D nanoparticle formation

and nanoelectrode/nanoband array fabrication—characteristics not found in other novel carbon nanomaterials such as edge plane pyrolytic graphite or planar graphene.[220,221]

In conclusion, this work demonstrates how nanoparticle placement on electrode surfaces can significantly alter the sensing capabilities of enzymatic biosensors. The model-inspired Pt nanosphere/SWCNT nanoband biosensors could potentially be used to monitor blood glucose levels where the physiological range for blood glucose is typically between 3.6 mM and 7.5 mM (65 mg/dL – 135 mg/dL) for healthy patients and between 1.1 mM and 16.7 mM (20 mg/dL – 300 mg/dL) for diabetic patients. Additionally, the high-density Pt nanosphere/SWCNT biosensors are capable of submicromolar glucose sensing and thus could be incorporated into devices that monitor glucose concentrations within saliva and tears.[222-224] These Pt nanosphere/SWCNT hybrid biosensors could also be potentially utilized in a self-referencing modality to monitor glucose transport processes in pancreatic β -cells, where highly sensitive glucose sensing is needed to improve the spatial and temporal resolution of the biosensor.[225,226] Furthermore, this completely bottom-up approach towards sensor fabrication and biofunctionalization creates a biosensor that can be potentially scaled and incorporated into devices for numerous commercial applications. Thus, this fusion of bottom-up nanoelectrode array design combined with computational analysis serves as a foundation for controlling nanotechnology-based electrochemical biosensor performance and functions as a design guideline for enzyme-based amperometric biosensors.

Acknowledgment. The authors would like to gratefully acknowledge assistance from the Purdue Physiological Sensing Facility, ABE Computational Biology Group, and the Nanoscale Transport Research Group of the Birck Nanotechnology Center and Bindley Bioscience Center. We graciously recognize funding support from the Purdue Research Foundation Trask Fund, Office of Naval Research, and National Science Foundation.

Supporting Information Available. Details regarding computational model including optimization metrics, parameter values, and the approximation of the total length of SWCNTs and density of Pt nanospheres by image-analysis techniques. This material is available free of charge via the Internet at <http://pubs.acs.org>.

References

- (1) Claridge, S. A.; Schwartz, J. J.; Weiss, P. S. *ACS Nano* **2011**, *5*, 693.
- (2) Jiang, X.; Hu, J.; Fitzgerald, L. A.; Biffinger, J. C.; Xie, P.; Ringeisen, B. R.; Lieber, C. M. *Proc. Natl. Acad. Sci. U.S.A.* **2010**, *107*, 16806.
- (3) Sun, P.; Laforge, F. o. O.; Abeyweera, T. P.; Rotenberg, S. A.; Carpino, J.; Mirkin, M. V. *Proc. Natl. Acad. Sci. U.S.A.* **2008**, *105*, 443.
- (4) Tricoli, A.; Pratsinis, S. E. *Nat. Nano* **2009**, *5*, 54.
- (5) Velmurugan, J.; Zhan, D.; Mirkin, M. V. *Nat. Chem.* **2010**, *2*, 498.
- (6) Compton, R. G.; Wildgoose, G. G.; Rees, N. V.; Streeter, I.; Baron, R. *Chem. Phys. Lett.* **2008**, *459*, 1.
- (7) García-Morales, V.; Krischer, K. *Proc. Natl. Acad. Sci. U.S.A.* **2010**, *107*, 4528.
- (8) Soleymani, L.; Fang, Z.; Sargent, E. H.; Kelley, S. O. *Nat. Nanotechnol.* **2009**, *4*, 844.
- (9) Arrigan, D. W. M. *Analyst* **2004**, *129*, 1157.
- (10) Murray, R. W. *Chem. Rev.* **2008**, *108*, 2688.
- (11) Zhang, B.; Zhang, Y.; White, H. S. *Anal. Chem.* **2006**, *78*, 477.
- (12) Bard, A. J.; Faulkner, L. R. *Electrochemical Methods. Fundamentals and Applications* **2001** 2nd ed.; John Wiley: New York, 2001.
- (13) Rao, C. N. R.; Kulkarni, G. U.; Thomas, P. J.; Edwards, P. P. *Chem. Eur. J.* **2002**, *8*, 28.
- (14) Godino, N.; Borrisé, X.; Muñoz, F. X.; del Campo, F. J.; Compton, R. G. *J. Phys. Chem. C* **2009**, *113*, 11119.
- (15) Lin, Y.; Lu, F.; Tu, Y.; Ren, Z. *Nano Lett.* **2004**, *4*, 191.
- (16) Tan, L. K.; Chong, A. S. M.; Tang, X. S. E.; Gao, H. *J. Phys. Chem. C* **2007**, *111*, 4964.
- (17) Menshykau, D.; Huang, X. J.; Rees, N. V.; Del Campo, F. J.; Muñoz, F. X.; Compton, R. G. *Analyst* **2008**, *134*, 343.
- (18) Lanyon, Y. H.; Arrigan, D. W. M. *Sens. Actuators, B* **2007**, *121*, 341.
- (19) Lanyon, Y. H.; De Marzi, G.; Watson, Y. E.; Quinn, A. J.; Gleeson, J. P.; Redmond, G.; Arrigan, D. W. M. *Anal. Chem.* **2007**, *79*, 3048.
- (20) Sandison, M. E.; Cooper, J. M. *Lab Chip* **2006**, *6*, 1020.
- (21) Sander, M. S.; Tan, L. S. *Adv. Funct. Mater.* **2003**, *13*, 393.
- (22) Katz, E.; Willner, I.; Wang, J. *Electroanalysis* **2004**, *16*, 19.
- (23) Luo, X.; Morrin, A.; Killard, A. J.; Smyth, M. R. *Electroanalysis* **2006**, *18*, 319.
- (24) Claussen, J. C.; Franklin, A. D.; ul Haque, A.; Porterfield, D. M.; Fisher, T. S. *ACS Nano* **2009**, *3*, 37.
- (25) Rakhi, R. B.; Sethupathi, K.; Ramaprabhu, S. *J. Phys. Chem. B* **2009**, *113*, 3190.
- (26) Wen, Z.; Ci, S.; Li, J. *J. Phys. Chem. C.* **2009**, *113*, 13482.
- (27) Lu, J.; Do, I.; Drzal, L. T.; Worden, R. M.; Lee, I. *ACS Nano* **2008**, *2*, 1825.

- (28) Hong, W.; Bai, H.; Xu, Y.; Yao, Z.; Gu, Z.; Shi, G. *J. Phys. Chem. C* **2010**, *114*, 1822.
- (29) Maschmann, M. R.; Franklin, A. D.; Scott, A.; Janes, D. B.; Sands, T. D.; Fisher, T. S. *Nano Lett.* **2006**, *6*, 2712.
- (30) Menshykau, D.; Huang, X. J.; Rees, N. V.; Del Campo, F. J.; Muñoz, F. X.; Compton, R. G. *Analyst* **2009**, *134*, 343.
- (31) Baronas, R.; Ivanauskas, F.; Kulys, J. *Sensors* **2003**, *3*, 248.
- (32) Bartlett, P. N.; Pratt, K. F. E. *Biosens. Bioelectron.* **1993**, *8*, 451.
- (33) Squires, T. M.; Messinger, R. J.; Manalis, S. R. *Nat. Biotechnol.* **2008**, *26*, 417.
- (34) Vijayendran, R. A.; Ligler, F. S.; Leckband, D. E. *Analytical Chemistry* **1999**, *71*, 5405.
- (35) Franklin, A. D.; Janes, D. B.; Claussen, J. C.; Fisher, T. S.; Sands, T. D. *Appl. Phys. Lett.* **2008**, *92*, 013122.
- (36) Anandan, V.; Gangadharan, R.; Zhang, G. *Sensors* **2009**, *9*, 1295.
- (37) Brito, R.; Tremont, R.; Feliciano, O.; Cabrera, C. R. *J. Electroanal. Chem.* **2003**, *540*, 53.
- (38) Ziegler, K. J.; Gu, Z.; Peng, H.; Flor, E. L.; Hauge, R. H.; Smalley, R. E. *J. Am. Chem. Soc.* **2005**, *127*, 1541.
- (39) Guo, S.; Wen, D.; Zhai, Y.; Dong, S.; Wang, E. *ACS Nano* **2010**, *4*, 3959.
- (40) Liu, Z.; Lin, X.; Lee, J. Y.; Zhang, W.; Han, M.; Gan, L. M. *Langmuir* **2002**, *18*, 4054.
- (41) Cambiaso, A.; Delfino, L.; Grattarola, M.; Verreschi, G.; Ashworth, D.; Maines, A.; Vadgama, P. *Sens. Actuators, B* **1996**, *33*, 203.
- (42) Lemke, K. *Med. Biol. Eng. Comput.* **1988**, *26*, 523.
- (43) Mell, L. D.; Maloy, J. T. *Anal. Chem.* **1975**, *47*, 299.
- (44) Baker, W. S.; Crooks, R. M. *J. Phys. Chem. B* **1998**, *102*, 10041.
- (45) Campbell, F. W.; Belding, S. R.; Baron, R.; Xiao, L.; Compton, R. G. *J. Phys. Chem. C* **2009**, *113*, 14852.
- (46) Jeoung, E.; Galow, T. H.; Schotter, J.; Bal, M.; Ursache, A.; Tuominen, M. T.; Stafford, C. M.; Russell, T. P.; Rotello, V. M. *Langmuir* **2001**, *17*, 6396.
- (47) Streeter, I.; Baron, R.; Compton, R. G. *J. Phys. Chem. C* **2007**, *111*, 17008.
- (48) Fan, Y.; Goldsmith, B. R.; Collins, P. G. *Nat Mater* **2005**, *4*, 906.
- (49) Montgomery, D. C.; Runger, G. C. *Applied Statistics and Probability for Engineers* **2010** 5th ed.; John Wiley: New York, 2010.
- (50) Davies, T. J.; Compton, R. G. *J. Electroanal. Chem.* **2005**, *585*, 63.
- (51) Fletcher, S.; Horne, M. D. *Electrochem Commun* **1999**, *1*, 502.
- (52) Hrapovic, S.; Liu, Y.; Male, K. B.; Luong, J. H. *Anal. Chem.* **2004**, *76*, 1083.
- (53) Kang, X.; Mai, Z.; Zou, X.; Cai, P.; Mo, J. *Talanta* **2008**, *74*, 879.
- (54) Pang, X.; He, D.; Luo, S.; Cai, Q. *Sens. Actuators, B* **2009**, *137*, 134.
- (55) Tsai, M. C.; Tsai, Y. C. *Sens. Actuators, B* **2009**, *141*, 592.
- (56) Zhao, K.; Zhuang, S.; Chang, Z.; Songm, H.; Dai, L.; He, P.; Fang, Y. *Electroanalysis* **2007**, *19*, 1069.

- (57) Wilson, G. S.; Hu, Y. *Chem. Rev.* **2000**, *100*, 2693.
- (58) Lane, J. D.; Krumholz, D. M.; Sack, R. A.; Morris, C. *Curr. Eye. Res.* **2006**, *31*, 895.
- (59) Jurysta, C.; Bulur, N.; Oguzhan, B.; Satman, I.; Yilmaz, T. M.; Malaisse, W. J.; Sener, A. *J. Biomed. Biotechnol.* **2009**, 2009.
- (60) Kim, S. S.; Amama, P. B.; Fisher, T. S. *J. Phys. Chem. C* **2010**, *114*, 9596.
- (61) Narayanan, R.; El-Sayed, M. A. *The Journal of Physical Chemistry B* **2005**, *109*, 12663.
- (62) Banks, C. E.; Compton, R. G. *Analyst* **2006**, *131*, 15.
- (63) Bong, S.; Kim, Y. R.; Kim, I.; Woo, S.; Uhm, S.; Lee, J.; Kim, H. *Electrochem. Commun.*, *12*, 129.
- (64) Claussen, J. C.; Sungwon, K. S.; Haque, A. u.; Artiles, M. S.; Porterfield, D. M.; Fisher, T. S. *J. of Diabetes Sci. and Technol.* **2010**, *4*, 312.
- (65) Fan, Y.; Goldsmith, B. R.; Collins, P. G. *Nat. Mater.* **2005**, *4*, 906.
- (66) Narayanan, R.; El-Sayed, M. A. *Nano Letters* **2004**, *4*, 1343.
- (67) O'Neill, R. D.; Chang, S. C.; Lowry, J. P.; McNeil, C. J. *Biosensors and Bioelectronics* **2004**, *19*, 1521.
- (68) Kagie, A.; Bishop, D. K.; Burdick, J.; La Belle, J. T.; Dymond, R.; Felder, R.; Wang, J. *Electroanalysis* **2008**, *20*, 1610.
- (69) Mukhopadhyay, R. *Analytical Chemistry* **2006**, *78*, 4255.
- (70) Tabak, L. A. *Annals of the New York Academy of Sciences* **2007**, *1098*, 7.
- (71) Jung, S.-K.; Trimarchi, J. R.; Sanger, R. H.; Smith, P. J. S. *Anal. Chem.* **2001**, *73*, 3759.
- (72) Porterfield, D. M. *Biosens. Bioelectron.* **2007**, *22*, 1186.

CHAPTER 3. CAN EMBRYONIC GEOMETRY AND SPATIALLY
HETEROGENEOUS MATERNAL PROTEINS ACCOUNT FOR DORSAL-
VENTRAL ASYMMETRIES IN GAP GENE PATTERNING?

3.1 A Note About this Article

The Public Library of Science (PLoS) applies the open-access Creative Commons Attribution (CC BY) license to its publications, including the *PLoS ONE* article contained in this chapter.

PUBLICATION

Hengenius, J. B., Gribskov, M., Rundell, A. E., Fowlkes, C. C., Umulis, D. M. (2011) Analysis of Gap Gene Regulation in a 3D Organism-Scale Model of the *Drosophila melanogaster* Embryo. *PLoS One* 6.

Analysis of Gap Gene Regulation in a 3D Organism-Scale Model of the *Drosophila melanogaster* Embryo

JB Hengeni^a, M Gribskov^a, AE Rundell^b, CC Fowlkes^c, DM Umulis^{d,e}

^aDepartment of Biological Sciences, Purdue University, West Lafayette, IN, USA

^bDepartment of Biomedical Engineering, Purdue University, West Lafayette, IN, USA

^cDepartment of Computer Science, University of California, Irvine, CA, USA

^dDepartment of Agricultural and Biological Engineering, Purdue University, West Lafayette, IN, USA

^eCorresponding Author (dumulis@purdue.edu)

Citation: Hengeni^a, Gribskov M, Rundell AE, Fowlkes CC, Umulis DM (2011) Analysis of Gap Gene Regulation in a 3D Organism-Scale Model of the *Drosophila melanogaster* Embryo. PLoS ONE 6(11): e26797. doi:10.1371/journal.pone.0026797

Editor: Johannes Jaeger, Centre for Genomic Regulation (CRG), Universitat Pompeu Fabra, Spain

Received: April 28, 2011; **Accepted:** October 4, 2011; **Published:** November 16, 2011

Copyright: © 2011 Hengeni^a et al. This is an open-access article distributed under the terms of the Creative Commons Attribution License, which permits unrestricted use, distribution, and reproduction in any medium, provided the original author and source are credited.

Funding: This research was funded by the National Institutes of Health (NIH) Biophysics Training Grant (5T32GM008296-21). The funders had no role in study design, data collection and analysis, decision to publish, or preparation of the manuscript.

Competing interests: The authors have declared that no competing interests exist.

Abstract

The axial bodyplan of *Drosophila melanogaster* is determined during a process called morphogenesis. Shortly after fertilization, maternal *bicoid* mRNA is translated into Bicoid (Bcd). This protein establishes a spatially graded morphogen distribution along the anterior-posterior (AP) axis of the embryo. Bcd initiates AP axis determination by triggering expression of gap genes that subsequently regulate each other's expression to form a precisely controlled spatial distribution of gene products. Reaction-diffusion models of gap gene expression on a 1D domain have previously been used to infer

complex genetic regulatory network (GRN) interactions by optimizing model parameters with respect to 1D gap gene expression data. Here we construct a finite element reaction-diffusion model with a realistic 3D geometry fit to full 3D gap gene expression data. Though gap gene products exhibit dorsal-ventral asymmetries, we discover that previously inferred gap GRNs yield qualitatively correct AP distributions on the 3D domain only when DV-symmetric initial conditions are employed. Model patterning loses qualitative agreement with experimental data when we incorporate a realistic DV-asymmetric distribution of Bcd. Further, we find that geometry alone is insufficient to account for DV-asymmetries in the final gap gene distribution. Additional GRN optimization confirms that the 3D model remains sensitive to GRN parameter perturbations. Finally, we find that incorporation of 3D data in simulation and optimization does not constrain the search space or improve optimization results.

Introduction

Embryonic development in *Drosophila melanogaster* is initiated with the formation of spatial morphogen distributions in the early embryo. The dynamic spatial patterns of diffusive morphogens encode information which specifies organism-scale development [1], [2]. Nonuniform initial spatial distributions of maternally deposited morphogen mRNAs, coupled with diffusion, decay, and complex genetic regulatory interactions, give rise to finer patterns that subdivide the dorsal-ventral (DV) [3]–[5] and anterior-posterior (AP) axes [2], [6] into distinct developmental regions.

The gap gene system is one of the most widely studied morphogen systems in *Drosophila* and is involved in delineation of boundaries of gene expression within the

AP body plan [2]. AP patterning events begin approximately one hour post-fertilization. This patterning foreshadows the subsequent segmentation of the embryo [1], [2], [6]–[9]. During early development, the embryo is a polynucleated syncytium; most nuclei are arrayed in a thin layer near the surface of the embryo. Due in part to a cytoplasmic viscosity gradient common to insect embryos [10], morphogens (here, gap gene products) are thought to diffuse freely through periplasm near the embryonic surface and less substantially through the interior. Here, they regulate transcription within the periplasmic nuclei [2]. The process is initiated by the gene products of maternally-deposited, spatially-heterogeneous *bicoid* (Bcd), *caudal* (Cad), and *nanos* mRNAs [2], [11],[12]. Maternally deposited RNA species regulate expression of the gap genes: Hunchback (Hb, with a maternal mRNA contribution), Giant (Gt), Tailless (Tll), Krüppel (Kr), and Knirps (Kni) (see Fig. 1a) [11], [13], [14]. The gap genes, in turn, regulate the pair-rule genes which in turn control segment-polarity genes and embryonic segmentation [1], [2], [6], [15].

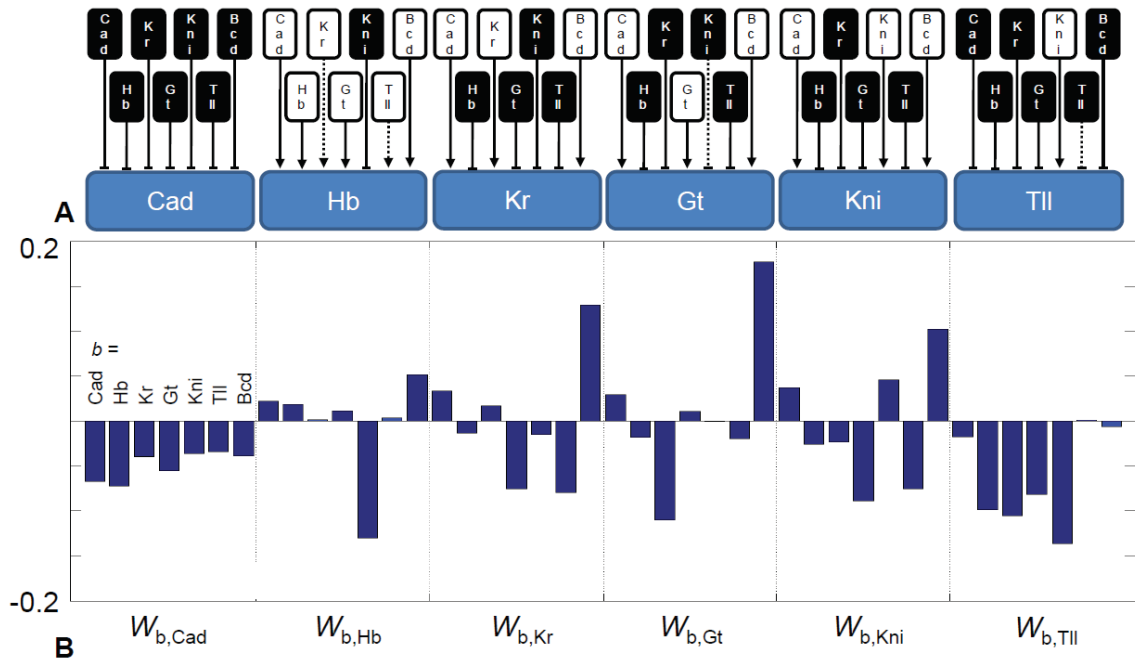


Figure 1. Gap gene genetic regulatory network.

The model representation of the gap gene network. The network topology in (A) represents negative (black box, flat line) and positive (white box, arrowhead) regulatory effects on each target gene (blue). Dashed lines represent near-zero regulatory inputs that may be negligible. This qualitative topology is quantified in (B) as a set of genetic regulatory network (GRN) weight parameters $w_{b,a}$, the influence of gene b on gene a . From left to right, each set of seven inputs represent Cad, Gt, Hb, Kni, Kr, Tll, and Bcd. Each cluster of seven interactions represents a target gene Cad, Gt, Hb, Kni, Kr, and Tll.

Most inferences regarding the gap genetic regulatory network (GRN) have been drawn from mutant and gene dosage studies in which the effects on morphology, gap, pair-rule, or segment polarity genes are observed [12], [16]–[36]. While these experiments are informative, it is difficult to unambiguously derive genetic regulatory interactions from such data; phenotypic changes may arise via direct action of the perturbed gene or via downstream targets of that gene. In contrast, Reinitz, Jaeger, and others applied a reverse engineering approach using dynamic wild-type data. Computational studies have modeled gap gene patterning using 1D partial differential equation (PDE) systems or ordinary differential equation systems that include an implicit approximation to the PDE [13], [14], [37]–[40] and logical rule sets [41]. These models represent the lateral trunk region of the *Drosophila* embryo along the AP axis, typically omitting the anterior and posterior end regions (with the exception of [40]). GRN topology is represented by a regulatory weight matrix and gene expression is modeled by a transfer function that sums the regulatory impact of each regulatory protein on expression of the others (see Fig. 1b) [13]. Model-driven inferences about GRN topology (*i.e.*, inferring whether and to what degree one morphogen regulates expression of other morphogens) have been obtained by inverse modeling: optimizing the regulatory weight matrix against experimental gap gene expression data in hopes of recovering “true” GRNs [14], [42]–[45]. Findings have been mixed. Biological systems are thought to be robust (and thus insensitive) to perturbations. Some GRN parameters are highly sensitive while considerable uncertainty is associated with others [44],[45].

Previous 1D PDE models have been used effectively to infer network topology and investigate patterning regulation [13], [14], [42], [45], [46], but there are some questions that are better investigated using a full 3D spatial patterning model. Many important 3D effects, including variable diffusive path lengths around the embryo surface and optimization against 3D data, cannot be observed in a 1D model domain. DV asymmetries in gap gene distribution and possible interactions between the gap gene system and DV patterning systems are also neglected. Further, these 3D data may serve to constrain GRN optimization and inference.

Quantitative spatiotemporal atlases of gene expression data in the *Drosophila* embryo have been published and provide the starting point for quantitative analysis. [47]–[49]. The atlas includes measurement of gap gene expression collected from hundreds of individual embryos and registered onto a standardized 3D mesh of nuclei coordinates using pair-rule gene expression patterns as fiduciary points (mesh coordinates available in [File S1](#)). This composite VirtualEmbryo (VE) is a logical starting point for the development of 3D embryonic GRN models. It provides a ready-made embryonic geometry for full spatial PDE representations of the gap gene system. It also contains quantitative expression data against which we can optimize model parameters (and thus infer GRNs).

Table 1: Model Variants and Corresponding Optimal Parameter Sets.

Model	Geometry	Initial Conditions	Optimal GRN Parameters* (M_{Data}^{Model})
M^{1D-P}	1D domain representing partial 35%–92% AP axis	$Gt_0 = Kni_0 = Kr_0 = Tll_0 = 0$; Bcd_{55} , Hb_0 , Cad_0 values in Jaeger et al. [13]	N/A (evaluated with Jaeger et al.'s reported GRN, P^D)
M^{1D-F}	1D domain representing full 0%–100% AP axis	$Gt_0 = Kni_0 = Kr_0 = Tll_0 = 0$; Bcd_{55} , Hb_0 , Cad_0 values in Jaeger et al.	P_{1D-P}^{1D-F} (fit to Jaeger's model output); $P_{1/2}^{1D-F}$ (fit to VirtualEmbryo data)
M_{Bcd1D}^{3D}	VE 3D domain	$Gt_0 = Kni_0 = Kr_0 = Tll_0 = 0$; Bcd_{55} , Hb_0 , Cad_0 values in Jaeger et al. projected about AP axis (see Fig. 3b–d)	P_{Bcd1D}^{3D} (evaluated with GRN $P_{1/2}^{1D-F}$)
M_{Bcd3D}^{3D}	VE 3D domain	$Gt_0 = Kni_0 = Kr_0 = Tll_0 = 0$; Hb_0 , Cad_0 values in Jaeger et al. projected about AP axis. Bcd_{55} interpolated from VE data (Fig. 3e).	P_{Bcd3D}^{3D} (evaluated with GRN $P_{1/2}^{1D-F}$)
$M_{Bcd3D-S}^{3D}$	VE 3D domain	$Gt_0 = Kni_0 = Kr_0 = Tll_0 = 0$; Hb_0 , Cad_0 values in Jaeger et al. projected about AP axis. $[Bcd]_{55}$ interpolated from VE data and smoothed (Fig. 3f).	$P_{Bcd3D-S}^{3D}$

*optimized by fitting model output to Virtual Embryo data unless otherwise noted.
doi:10.1371/journal.pone.0026797.t001

Using the VE data, we evaluate the impact of 1D model assumptions, conversion from 1D to 3D geometries, and incorporation of fully 3D protein distribution data in model simulation. Herein we reconstruct the 1D gap gene model of Jaeger *et al.* [13] using the finite element method (FEM) and extend it to the 3D VE geometry (Fig. S1). The 1D model of Jaeger *et al.* [13], M^{1D-P} (see Table 1 for model definitions), is refit to lateral expression data from the VE. We then extend the 1D model PDEs to the full 3D embryonic geometry described by Fowlkes *et al.* and compare GRNs inferred from 1D and 3D models. Though 1D models focus on the lateral AP axis in 1D simulations, gap genes are not uniformly distributed along the DV axis. Coupled with the 3D geometry, DV asymmetries in initial conditions may encode positional information partially responsible for the observed AP patterning. As a preliminary exploration of asymmetric DV effects in an embryonic geometry, we evaluate the model using DV-asymmetric Bcd concentration data from thirteen embryos compiled in the VE.

In addition to GRN sensitivities highlighted by previous 1D analyses [14], [38], [39], [44], [50], we find that the 3D model exhibits fragility with respect to the shape of maternal gradients: GRNs which were inferred by optimization of 1D models showed similar gap gene patterning when applied to 3D models with DV-symmetric Bcd. However, these GRNs gave rise to qualitatively different patterns in DV-asymmetric models. These realistic Bcd gradient models also captured some of the DV-asymmetries in gap gene patterning. The 3D models were also sensitive to small perturbations in GRNs; regulatory networks which were qualitatively similar (*i.e.*, all network interactions maintained the same excitatory or inhibitory relationships and

differed only by small changes in magnitude) led to qualitatively different gap gene patterns. Refitting of the DV-asymmetric 3D model to VE data produced a GRN which was similar to 1D GRNs but which produced an improved fit.

Another question addressed in this study is whether inclusion of 3D data improves optimization by the inclusion of additional constraints without increasing the degrees of freedom in the model. Unexpectedly, we found that the incorporation of additional 3D information in the form of a realistic DV-asymmetric Bcd worsened the error between optimized 3D models and data. This suggests the involvement of additional regulators in the formation of DV-asymmetries and indicates a direction for future modeling studies.

Results

One-Dimensional Model Analysis

Before analyzing the effects of embryonic geometry and DV-asymmetric positional information, we reimplemented the 1D model of Jaeger *et al.* using the finite element method. In this work we denote model variants with M ; superscripts represent model domains and subscripts signify initial conditions if multiple initial conditions are used. The 1D model of Jaeger *et al.* is called M^{1D-P} (using a 1D domain representing a partial AP length of 35%–92%; full model nomenclature available in Table 1). We verified M^{1D-P} against Jaeger *et al.*'s simulated output. Whereas the original model limited gene expression to a finite number of discrete nuclear coordinates along the 35–92% region of the embryonic AP axis, the FEM approximates a continuous solution to these equations along this domain. Discrete versus continuous model comparisons by

Gursky *et al.* suggest that embryonic patterning is not strongly coupled to nuclear position and that continuous models are comparable to discrete models of gene expression [51]. Our results agree with this finding. FEM simulations produce model output comparable to Jaeger *et al.*'s discrete 1D model (Fig. 2a, dashed line, cf. Figure S20 in [13]).

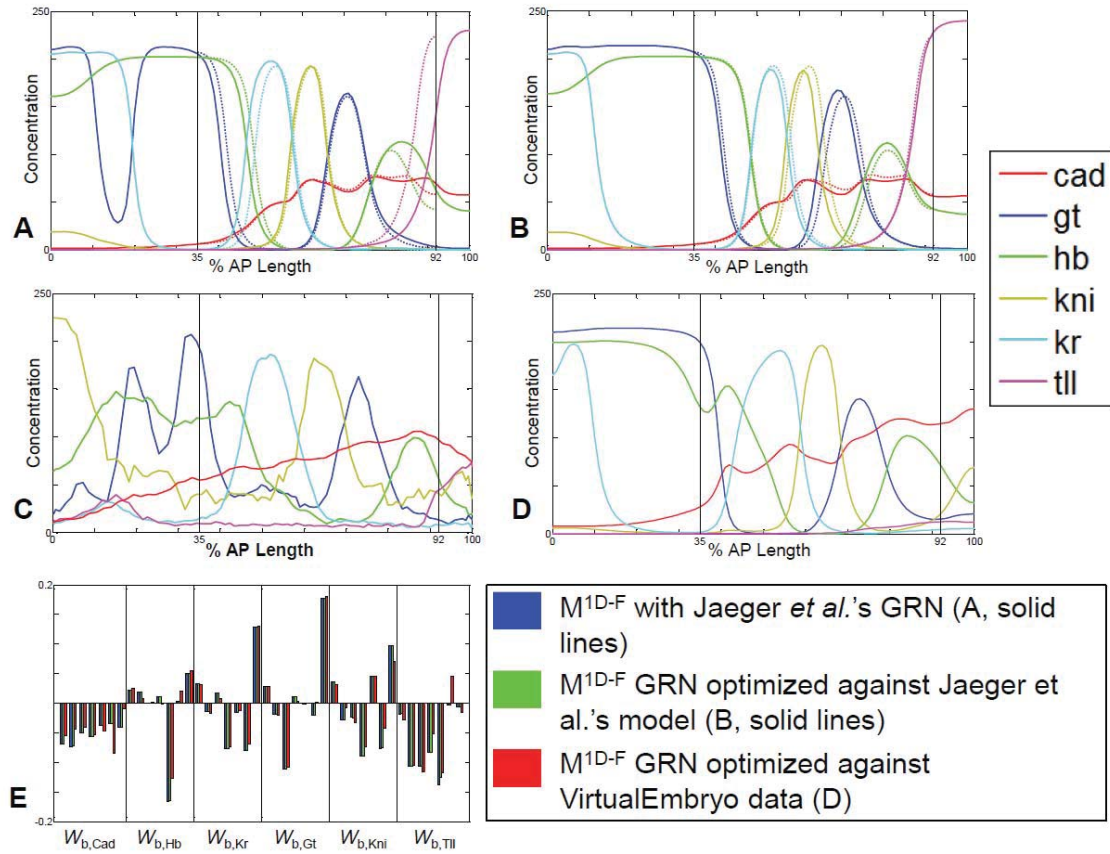


Figure 2. One-dimensional model results.

Model output was simulated over a 0–100% AP length domain using the optimal GRN reported by Jaeger et al. Solid vertical lines represent the original model boundaries, not used in this simulation. (A) (solid lines) shows qualitative agreement with the Jaeger model (dashed lines) in the 35–92% AP range, but shows discrepancies at either end of the domain due to the movement of boundaries; all species displayed at $t = 70$ min. (B) The best-fit GRN from Jaeger et al. was locally optimized to improve the agreement of the 0–100% AP length, model (solid lines), and the original Jaeger et al. original model (dashed lines); all species displayed at $t = 70$ min. (C) VE protein data for Gt, Hb, Kni, Kr at $t = 70$ min; VE mRNA data for Tll at $t = 70$ min; protein data from Jaeger et al. for Cad at $t = 56$ min. (D) Model output (solid lines) was also optimized against VE data (RMSE = 13.992); Gt, Hb, Kni, Kr, Tll at $t = 70$ min; Cad at $t = 56$ min. Despite modest improvements in model agreement in the 35% and 92% region (C–D), the resulting changes in parameter values were small. (E) Optimized parameter magnitudes vary but signs remained the same in most cases (blue - ; green - ; red -).

Though M^{1D-P} recapitulated previous results when simulated in the region from 35–92% on the AP axis, we sought to determine whether moving the boundaries to the embryo ends perturbed gap gene patterning in the trunk region. It is unclear *a priori* how modification of boundary conditions might impact the model output, because the selection of boundaries at 35% and 92% in earlier work appears to coincide with either maxima or minima of gap gene distributions; at these positions, spatial derivatives are near zero and diffusive flux may be negligible. Using no-flux boundaries at 0% and 100% EL, coupled with the parameters and initial conditions specified in the original model [13], we evaluated M^{1D-P} and M^{1D-F} using the GRN parameters P^0 reported by Jaeger *et al.* [13]. Herein, parameter sets are denoted P and super- and subscripts have model-specific meanings. The simulated patterns from the original 35–92% AP and the 0–100% AP domains are shown in Figure 2a's dashed and solid lines, respectively.

Pronounced shifts in Tll and Kr distributions, coupled with the qualitative change in the anterior Gt distribution, demonstrate the role boundary conditions play in the in the distribution of gap gene products for a given set of parameters. Though the output of M^{1D-P} qualitatively resembles the expression data collected previously when evaluated at P^0 [13], these findings suggest that M^{1D-P} 's agreement with data arises from a combination of the inferred GRN and the domain's boundary conditions. Thus, the internal zero-flux boundary conditions used in previous models may bias GRN inference. To evaluate the impact of boundary placement on GRN inference, we performed a numerical gradient descent search of the parameter space to minimize the root mean squared error (RMSE) between M^{1D-F} and M^{1D-P} (represented by the dashed line

in Figure 2a). The search was initialized with the previously reported optimal P^0 . The result of this search, optimized GRN P_{1D-P}^{1D-F} (superscript denotes the model being optimized and subscript denotes data with which the model is optimized), is illustrated in Figure 2b. Here, the output of M^{1D-P} represents extant models' with internal no-flux boundaries.

Though domain boundary placement affects the banding pattern, Figure 2b suggests that these constraints have a limited effect on GRN inference. Optimizing the GRN parameters of M^{1D-F} to fit the original model output recovered a quantitatively similar patterning within the 35–92% AP length of the full 1D domain. Additionally, the optimized GRN P_{1D-P}^{1D-F} was qualitatively similar to P^0 (e.g., though optimized parameters underwent small changes in magnitude, all parameters maintained the same sign, Fig. 2e).

To facilitate a direct comparison between 1D and 3D models presented herein, we first evaluated the goodness-of-fit between the 35–92% AP (M^{1D-P}) and full AP domain (M^{1D-F}) 1D models using VE data. When possible, we use protein expression data from the VE: Gt, Hb, Kni, and Kr protein data is available across six equidistant time points spanning 50 minutes. Tll protein data is unavailable and we use Tll mRNA data as a surrogate for the protein distributions. Cad protein distributions are also unavailable in the VE; we substitute 1D Cad data from Jaeger *et al.* [13] that spans 45 minutes with seven time points. Because the 1D model domains represent the lateral region of the full embryo, we extracted expression data from this region of the VE (Fig. 2c). We performed

a constrained search of GRN parameters initialized at P_{1D-P}^{1D-F} to yield an optimized GRN P_{VE}^{1D-F} (subscript *VE* denotes VE training data). The resulting model output and a comparison of model parameters are shown in Figures 2d–e.

Though M^{1D-F} was capable of recovering the output of M^{1D-P} (with parameter set P_{1D-P}^{1D-F}) and VE data (P_{VE}^{1D-F}) within the 35–92% AP axis, poor fit to VE data persisted outside of this region. The 0–35% and 92–100% AP regions exhibit qualitative disagreement with VE data in these regions consistent with the biological requirement for additional head and tail patterning genes (Fig. 2c–d).

Three-Dimensional Model Analysis

Beginning with the GRN optimized on the full 1D domain, we extended the model to a 3D domain using the geometry in the VE. This was performed by implementing the system of PDEs on a 2D surface “wrapped” around the VE geometry. We used this model to evaluate the effects of both model geometry and DV-asymmetric initial conditions on model output.

To assess the effects of model geometry on patterning independent of initial conditions, the model was first simulated using DV-symmetric initial conditions (M_{Bcd1D}^{3D}): Bcd, Hb, and Cad distributions at time zero were obtained from the original 1D model and projected around the surface of the embryo (Fig. 3a–d). Evaluated at the previously inferred optimal 1D GRN (P_{VE}^{1D-F}), model M_{Bcd1D}^{3D} yielded patterning qualitatively

similar to the full length 1D model output (Fig. 4a–g, column 2). To confirm our derivation of the diffusion constants (see [Methods](#)) and rule out unintentional adjustment of the diffusive length constant ($\sqrt{D_a/\lambda_a}$), we performed a continuation of diffusion constants while holding decay parameters (λ_a) values constant ([Figs. S2, S3](#)). While band overlap does vary with diffusion constants, they are quantitatively similar. Interestingly, symmetric Bcd models appear robust against increased diffusion ([Fig. S2](#)) while increased diffusion disrupted patterning in asymmetric Bcd models ([Fig. S3](#)). The pattern formation timecourse for Bcd-symmetric patterning is animated in [Movies S1, S2, S3, S4, S5, S6](#).

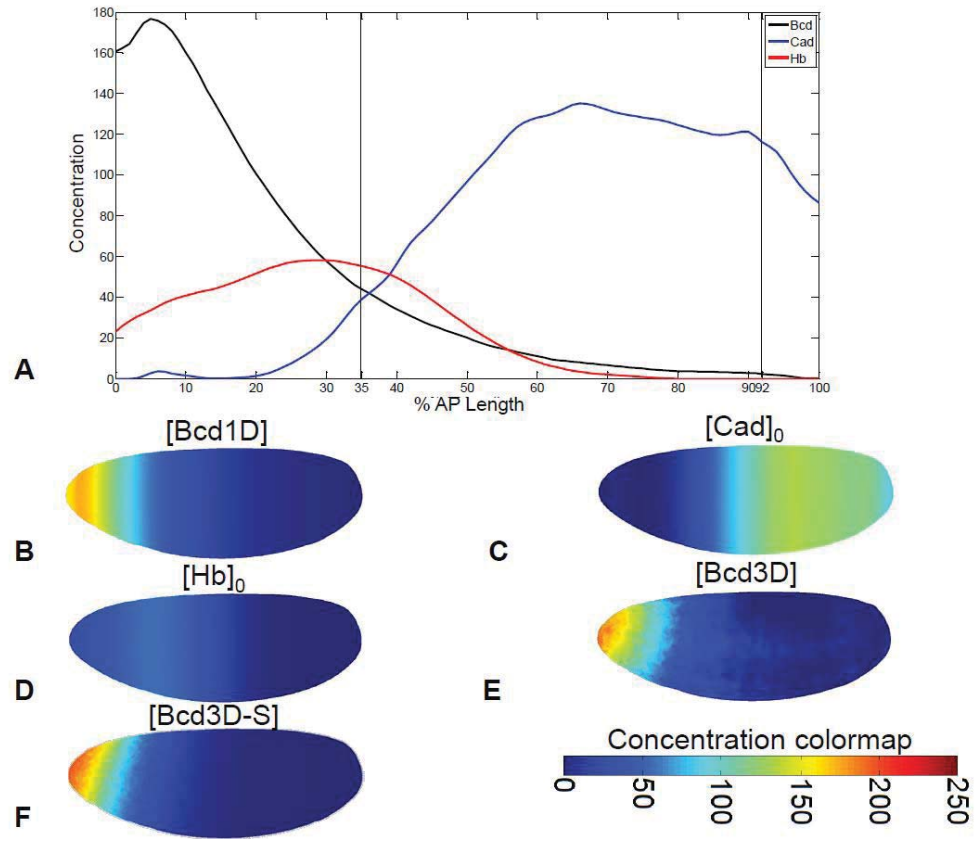


Figure 3. 1D and 3D initial conditions.

Initial conditions in various models. (A) 1D model initial conditions, reported by Jaeger et al., and used in models and . (B) 1D initial conditions were mapped onto the 3D embryonic geometry (S1). (C), 1D initial Cad protein distribution, (D) 1D initial Hb protein distribution. Subsequent models incorporated (E) DV-asymmetric interpolated [Bcd] distribution (E) or (F) smoothed DV-asymmetric interpolated [Bcd] distribution ()

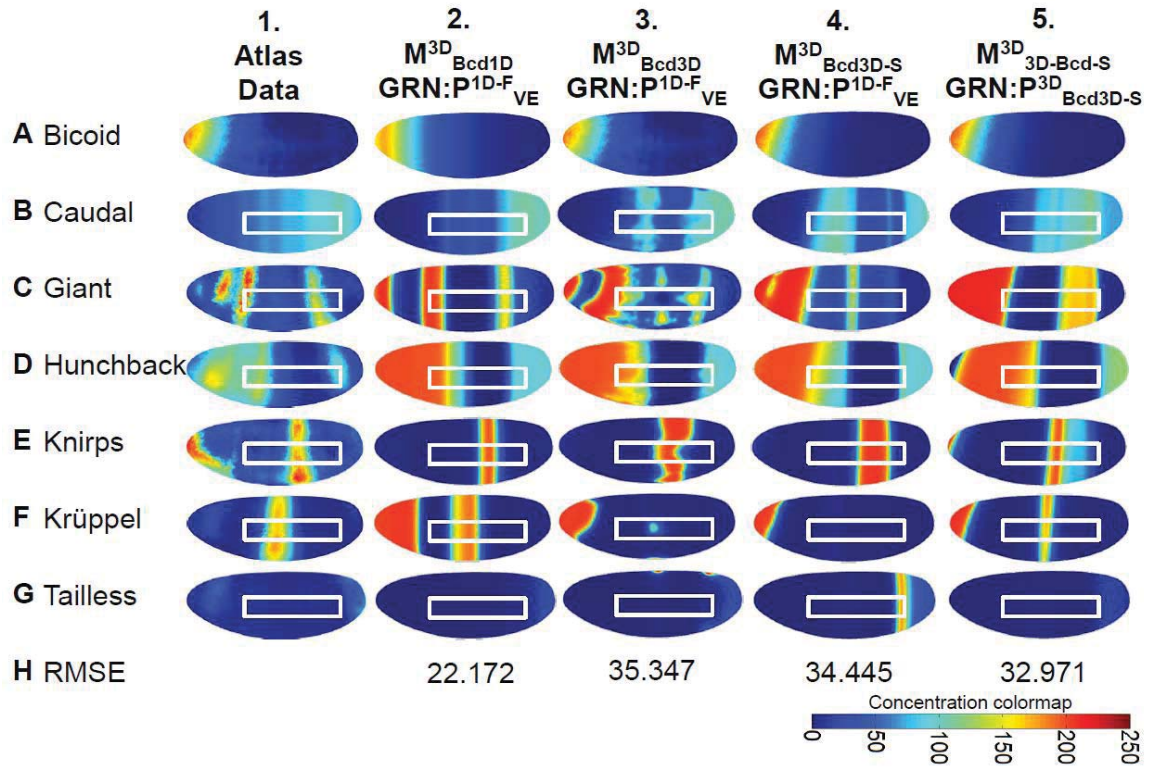


Figure 4. Three-dimensional model results.

Simulation results in the 3D model. (A–H) Lateral view of VE geometry is shown in rows A–G (Gt, Hb, Kni, Kr, Tll at $t = 70$ min, Cad at $t = 56$ min); row H displays RMSE difference between model and VE data summed with all time points. Column 1 shows scaled VE data. Column 2 displays output from evaluated with GRN. Column 3 contains output from incorporating DV-asymmetric Bcd data and GRN; Column 4 illustrates the effect of the smoothed Bcd interpolant in while considering the same GRN. Column 5 displays output from with reoptimized parameters. White boxes indicate the lateral areas where Jaeger et al. optimized their 1D model. Animations of pattern development are available for column 2 (Movies S1, S2, S3, S4, S5, S6) and column 5 (Movies S7, S8, S9, S10, S11, S12) in the supplementary material.

Though there are some DV-asymmetries present in the output (*e.g.*, slight curvature of the anterior Gt stripe), 1D versus 3D domain geometry alone has only a modest impact on DV patterning of gap genes. This suggests that the pronounced DV-asymmetries present in the final distributions of the proteins at the onset of nuclear division 14 (Fig. 4, column 1) stem from other sources. We consider the effect of spatial information encoded in initial DV asymmetries of protein distributions. The coupling of gap gene regulation with DV-patterning systems [5], [52], [53] is another possibility.

Effect of Dorsal-Ventral Asymmetric Bcd

To evaluate the impact of DV-asymmetric inputs on the model, we modified the steady-state Bcd distribution shown in Figure 3b to incorporate a realistic DV gradient (Fig. 3e). Unlike other morphogens, the Bcd distribution is static over the entire time course of model simulation. This allowed us to create a single interpolant of VE Bcd data and use it as a model input for all 70 minutes of the simulation. The pattern formation timecourse for Bcd-asymmetric patterning is animated in [Movies S7](#), [S8](#), [S9](#), [S10](#), [S11](#), [S12](#).

Evaluated at the optimal 1D GRN P_{VE}^{1D-F} , model M_{Bcd1D}^{3D} produces patterning that is radically different from DV-symmetric 1D (M^{1D-F}) and 3D (M_{Bcd1D}^{3D}) models (Figs. 4a–g, column 3). The most striking example of this is the Kr model output; whereas Kr forms a full band *in vivo*, M_{Bcd3D}^{3D} lacks full lateral expression of Kr and has an anomalous region of expression at the anterior end of the embryo (Fig. 4f, column 3). Similarly, the simulated Hb concentrations remain above observed levels (Fig. 4d, **column 3**). The

posterior Hb band also shifts to the posterior end of the embryo. Gt exhibits qualitative disagreement with the VE data; whereas anterior Gt expression is observed only in a limited dorsal region of the embryo (Fig. 4c, column 1), the anterior of the M_{Bcd3D}^{3D} is saturated with Gt (Fig. 4c, column 3). Further, though the experimentally observed posterior Gt band (Fig. 4c, column 1) is predicted by simulation, it exhibits unusual differences in width along the DV axis. As in previous versions of the model, the best agreement between model and data was found in the lateral 35–92% AP region (Fig. 4b–g, column 3 white boxes).

The cell-to-cell variability in patterning found for many simulated proteins (*e.g.*, Gt, Cad, and Kni) in M_{Bcd3D}^{3D} led us to consider the effect of noise in the VE Bcd distribution. Diffusion of Bcd may serve to smooth this variation *in vivo*; our use of a single static Bcd interpolant in M_{Bcd3D}^{3D} leads to an artificial persistence of the noise found in VE data (Fig. 3e). To test for and remove this artificial condition, we created a regularized version of the Bcd interpolant (Fig. 3f). This was constructed by building a simple source diffusion decay (SDD) reaction-diffusion model of Bcd alone [18]. This SDD model was fit to VE data and the steady-state solution was used as the smoothed Bcd interpolant. The model incorporating regularized Bcd, $M_{Bcd3D-S}^{3D}$, did not show significant improvement over M_{Bcd3D}^{3D} when evaluated with P_{VE}^{1D-F} (Fig. 4 a–g, column 4). However, it did eliminate the cell-to-cell variability present in M_{Bcd3D}^{3D} . The model's artificial sensitivity to Bcd noise was especially evident in Gt (Fig. 4c, columns 3–4). Two anterior and one posterior Gt bands in M_{Bcd3D}^{3D} changed width and AP position after smoothing of Bcd.

This result suggests that while diffusion may serve as a buffer against transient stochastic variations in protein expression and local concentration (in agreement with stochastic simulation [54]), sustained cell-to-cell variability has the potential to disrupt patterning.

Having observed that a GRN inferred on the 1D domain (and lacking DV asymmetries) produces a qualitatively incorrect fit compared to 3D data, we attempted to optimize the GRN with Matlab's constrained search function `fmincon()` initialized

at P_{VE}^{1D-F} (previously used to estimate P_{1D-P}^{1D-F} and P_{VE}^{1D-F}). This approach failed to reduce model error. Fomekong-Nanfack *et al.* demonstrated that 1D gap gene systems are amenable to optimization by evolutionary algorithms [45]. We therefore employed a genetic algorithm (GA) to more broadly survey the parameter space. Due to computational cost, we used a small population size of 20 genomes to search the GRN parameter space (42 parameters), the GA identified an optimal GRN for $M_{Bcd3D-S}^{3D}$. The resulting GRN, $P_{Bcd3D-S}^{3D}$, led to a reduction in model error and a modest qualitative improvement with respect to 3D data (Fig. 4, column 5). The lateral Kr band missing from the 1D-inferred GRN P_{VE}^{1D-F} (Fig. 4f, columns 3–4) is restored (Fig. 4f, column 5), though it is not as wide as the experimentally observed band. Tll no longer shows relative over-expression at the posterior end of the embryo (Fig. 4g, column 5). Hb continues to exhibit relative over-expression at the anterior end of the embryo, though its posterior band is shifted closer to its correct position (Fig. 4d, column 5). Similarly, the anterior distribution of Gt extends beyond the dorsal region observed in the VE (Fig. 4c, column 1). However, its posterior band is now located correctly in Figure 4c, column 5 (though it

is wider than the observed protein band). Beyond differences in concentration of individual proteins, DV-asymmetric Bcd causes a notable qualitative difference in the AP position and emergence of protein bands. Compared to the M_{Bcd1D}^{3D} (Fig. 4, column 2), the DV-asymmetric GRNs (Fig. 4, columns 4–5) exhibit DV-asymmetries in their output. For example, the dorsal terminus of the anterior Gt band is posterior to its ventral terminus; it is splayed toward the anterior. This behavior agrees with observed data in the anterior half of the embryo, but the expected DV curvature is either absent (posterior Hb Fig. 4d, column 5) or inverted in the posterior half of the embryo. For example, Kni, whose dorsal terminus should exhibit posterior-splaying (Fig. 4e, column 5), is inverted. This DV curvature corresponds in direction to the DV asymmetry of Bcd. The absence of reversed splaying in the output in the posterior portion of the model (though present in the data) suggests that the model may be lacking additional posterior determinant(s) affecting the gap gene system.

In the 3D regime, $M_{Bcd3D-S}^{3D}$ demonstrated considerable sensitivity to small changes in GRN parameter values. The model was simulated after adding normally distributed noise scaled by each parameter value, p_i , across a range of magnitudes (sample model output in Fig. 5). The model gives output qualitatively similar to the optimal GRN $P_{Bcd3D-S}^{3D}$ only when parameter noise is low (e.g., 0.1% p_i in Fig. 5, column 1). All other simulations, with noise terms of 1% p_i and higher, yielded drastically and qualitatively different outputs.

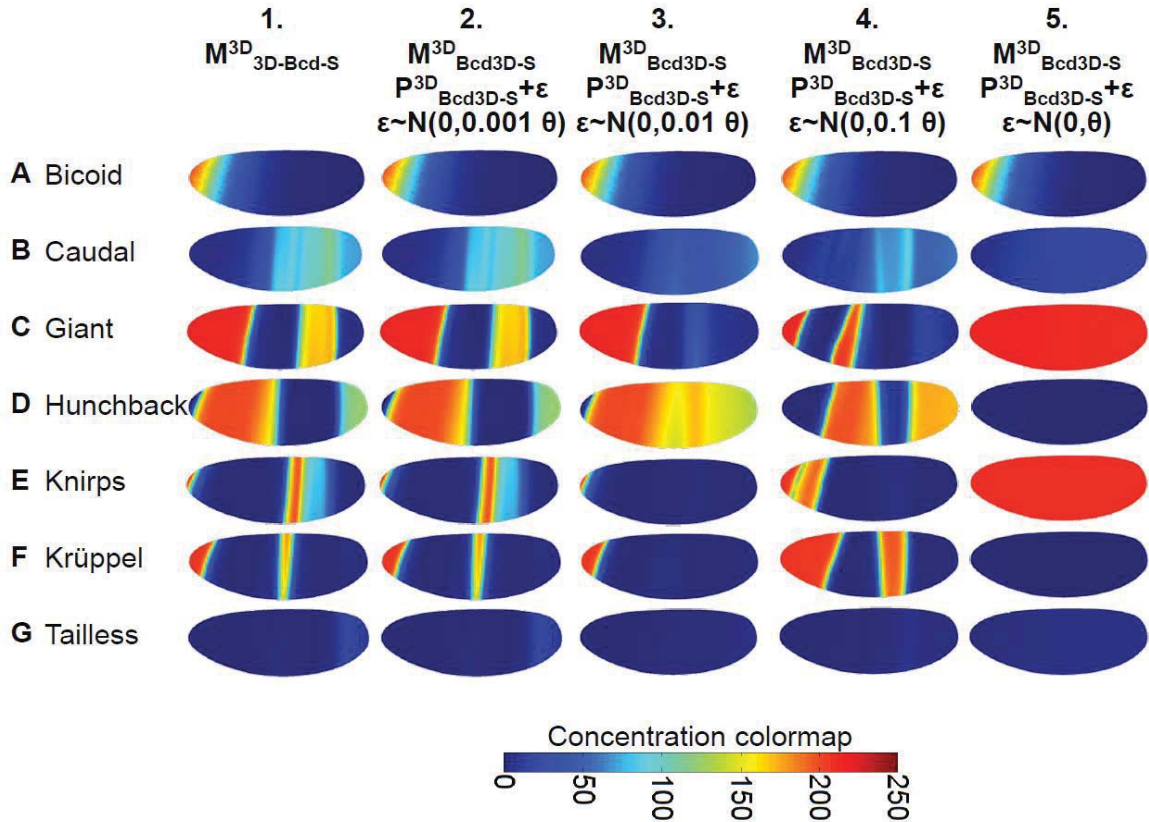


Figure 5. Model is not robust to noise in GRN parameters.

Parametric noise alters model output. Lateral view of VE geometry for all genes is shown in rows A–G (all outputs at $t = 70$ min). Each column displays output at $t = 70$ min evaluated with GRN . Columns 2–5 represent randomly chosen sample output when a normally distributed noise vector ϵ is added to the GRN parameter set (denoted θ). ϵ has mean of 0 and variance that scales with θ .

In summary, the GRNs we inferred in this study are qualitatively similar: magnitudes of parameters vary by approximately 10% and parameter sign stays the same in all but a few low-magnitude parameters (see [Table S1](#)). A notable exception is the regulatory parameter for the $\text{Kni} \rightarrow \text{Tll}$ interaction; here the sign of the parameter (and thus the regulatory relationship) is reversed. However, we acknowledge that the treatment of Tll as a state variable under gap gene regulation is artificial and this biological relevance of this observation is questionable. Optimization leaves most regulatory parameters with the same sign and changes only the magnitudes, and those regulatory weights which change sign have small magnitudes (*i.e.*, small regulatory effects). The use of a global search method (GA) to optimize $M_{\text{Bcd}3\text{D}-S}^{3\text{D}}$ did not recover a superior GRN that differed qualitatively from the original P^0 .

Discussion

The understanding of *Drosophila* developmental gene regulation has benefited from advances in quantitative modeling of gene regulation. However, existing PDE models of AP patterning have been limited to 1D approximations of the 3D geometry. By extending a model of gap gene regulation to a 3D embryonic geometry and adding realistic DV-asymmetry to upstream maternal Bcd, this work allows us to pose new questions about the effects of embryonic shape and DV gradients on gap gene patterning. Jaeger *et al.*'s 2004 model has been succeeded by more recent models of gap gene development incorporating additional regulatory inputs [37]–[39], [46], [55]–[58]. However, recent models of AP patterning retain partial domains (*e.g.*, 35%–92% AP) with internal no-flux boundary conditions and use regulatory schema similar to eqns. 1–3 (see Methods) to

represent GRNs. We chose the Jaeger *et al.*'s 2004 model as a case study in 1D vs. 3D modeling because it is the representative of many existing 1D models.

Before comparing 1D and 3D geometries, we examined the effect of boundary position in PDE solutions. Though embryos do not contain physical barriers to diffusion at 35% and 92% of the AP axis, small spatial gradients (Fig. 2a, dashed lines) at those positions suggested that small diffusive flux would minimize the effects of these internal boundaries. However, we found that the system was sensitive to boundary placement (cf. Fig. 2a, solid lines). Though this finding indicates the importance of using biologically realistic boundary conditions (*i.e.*, no-flux boundaries at 0% and 100% AP), the simulations in Figure 2 also illustrate our limited representation of regulation beyond the 35%–92% trunk region: Omission of terminal gap genes and regulators result in optimized parameter sets that cannot recapitulate expression patterns from 0%–35% and 92%–100% AP in M^{1D-F} (Fig. 2a,c). Optimization to correct the boundary artifacts (M^{1D-F} with P_{1D-P}^{1D-F}) likewise fail to improve agreement with data outside of the 35%–92% region (Fig. 2b). The inclusion of terminal gap genes such as Hucklebein in 1D gap gene models [37] provides a basis for extension to full 100% AP 1D and 3D models, though inclusion of Hucklebein in a recent 3D modeling study yielded only modest improvements in overall cost and qualitative agreement at the AP extrema [59].

Prior analyses demonstrated the sensitivity of gap gene models to GRN parameter values [14],[43], [44] and examination of boundary conditions support this finding: GRN parameter optimization corrected boundary artifacts with extremely small changes to

parameter values (Fig. 2e). Optimization against VE data produced similar small changes in GRN parameters (Fig. 2e). The GRN sensitivity of 1D models M^{1D-P} and M^{1D-F} was also found in 3D models. [Table S1](#) collects all parameter values and reports the standard deviation for each parameter across 1D and 3D model optimizations. Parameter $w_{Gt,Bcd}$ exhibits the highest deviation across models with a standard deviation of 0.05, but this represents only 13% of the total parameter range ($[-0.2,0.2]$). These small changes in GRN parameters do more than shift protein band location as observed in Figure 2; they are capable of effecting qualitative patterning changes (*e.g.*, changing the number of protein bands present on the embryo). For example, the transition from P_{VE}^{1D-F} to $P_{Bcd3D-S}^{3D}$ in model $M_{Bcd3D-S}^{3D}$ leads to the loss of a posterior Gt band and the creation of a posterior Kr band (Fig. 4c,f, columns 4–5). Figure 5 shows randomly selected sample model outputs at $t = 70$ min with increasing levels of normally distributed noise added to the GRN parameter vector. One percent noise was sufficient to induce qualitatively different banding patterns on the 3D geometry. The qualitative changes in patterning for all but the smallest levels of noise confirm the observations of parameter sensitivity in 1D and 3D models. The extreme sensitivity of model outputs to small changes in GRN parameters challenges analyses of GRN evolution positing phenotypically robust fitness landscapes [60]–[62]. Unfortunately, the computational expense of PDE models prevented an exhaustive exploration of the GRN parameter space and corresponding approximation of a fitness landscape. The fragility of the gap gene system to GRN perturbations bears further study, especially in its contrast to prevailing thoughts that evolution occurs on networks with highly-connected neutral (selectively equivalent) genotypes.

In addition to the parameter sensitivity and boundary conditions, our work also demonstrate the use of accurate 3D geometry and its effects on model predictions. We found that geometry alone has a limited effect on gap gene patterning: Excepting slight DV-asymmetry brought about by the curvature of the 3D embryo, 1D output from M^{1D-F} (Fig. 2d) and 3D output from M_{Bcd}^{3D} (Fig. 4, column 2) display qualitatively similar band position along the AP axis. The path length from anterior to posterior extrema differs with DV position: For example, the distance from anterior to posterior extrema is shorter along the dorsal surface than the ventral surface. We thought that this difference in diffusion distance might account for the anterior splaying displayed in VE data (Fig. 4, column 1), but this was not the case.

Though the 3D embryonic geometry was insufficient to explain DV-asymmetries in gap gene data, it allowed us to explore the effect of DV-asymmetric protein distributions on patterning. Notably, the 1D Bcd distribution of M_{Bcd}^{3D} (Fig. 3b) differed from the typical dorsal-anterior distribution [63], [64] also found in the VE (Fig. 3e). Experimental noise in this data led to aberrant patterning in most gap genes in M_{Bcd}^{3D} (Fig. 4, column 3), but a regularized version of the distribution (Fig. 3f) produced cleaner (though qualitatively incorrect) band appearance and position in M_{Bcd}^{3D-S} (Fig. 4, column 4). It also produced anterior-splaying in the anterior bands of Gt, Hb, Kni, and Kr. As previously noted, optimization of the sensitive GRN parameters improved qualitative agreement in model patterning with only small changes to parameter values ([Table S1](#)).

When considering 3D models and the data associated with them, we endeavored to identify any constraints on model optimization. This model has many degrees of freedom and additional information encoded in the DV asymmetries of gap genes might better guide parameter searches toward accurate GRNs. However, we observed no improvement in RMSE values and failed to find any novel GRNs for DV-asymmetric models.

Though our ensemble of models has led to interesting findings, we acknowledge model limitations. Recent modeling studies recognize that Cad and Tll patterning cannot be completely accounted for by gap genes in existing models; maternal mRNA complicates Cad expression and Tll is under the regulation of additional proteins [38]. Instead, newer models use data interpolants to represent these proteins [38]. The absence of these interpolants in our models may contribute to the unrealistic sensitivity of the 3D model parameters and DV-information. 3D interpolating functions incorporating VE data for Cad and Tll are under development; we will use these to explore the behavior of more recent 1D models on the 3D embryonic geometry.

The primary focus of this work is the comparison of 1D and 3D model geometries. Figures 2 and 4, column 2 reveal that differences in model geometry can be accommodated by relatively minor adjustments to GRN parameters. The 3D implementation (M_{Bcd}^{3D}) exhibits minor DV-asymmetries but otherwise mirrors M^{1D-F} . However, consideration of AP patterning in three dimensions allows us to address the experimentally observed DV-asymmetry in maternal Bcd and downstream AP morphogens. The inclusion of a DV-asymmetric Bcd signal led to qualitatively

different patterning with P_{VE}^{1D-F} (Fig. 4, columns 2,4). This suggests that the assumption of DV and AP independence in previous modeling studies is violated. Parameter sensitivity remained high; parameter optimization made small changes to parameter values but led to significantly improved RMSE error (Fig. 4, columns 4,5).

Finally, two cases of DV model mismatch suggest modifications that could be incorporated into future models. First, anterior Gt is more highly expressed on the dorsal side of the embryo *in vivo*, but posterior Gt displays posterior-splaying. This expression localization is not accounted for by Bcd distribution alone and should be addressed in future models that also include input from the DV patterning system downstream of the active Dorsal protein distribution [65], [66]. Second, many protein species display DV-asymmetry in terms of anterior or posterior splaying. *E.g.*, Cad bands anterior to the AP midline are anterior-splayed (Fig. 4b, column 1) while bands posterior to the AP midline are posterior-splayed. This pattern is observed for all modeled proteins (Fig. 4, column 1), though it is lacking in DV-symmetric M_{Bcd1D}^{3D} (Fig. 4, column 2). Addition of DV-symmetric Bcd (M_{Bcd1D}^{3D}) restores anterior-splaying aligned with the DV Bcd gradient (Fig. 4, column 5). This suggests that a missing posterior determinant may be responsible for posterior-splaying. The posterior maternal morphogen Nanos is a candidate that has not been included in previous models. With interpolated Cad and Tll, future models will explore the effects of posterior determinants such as Nanos [67] and, as examined in prior 1D models, Huckebein [37].

Methods

Model Construction

Building on the successful 1D/3D embryonic modeling approach of Umulis *et al.*, [4], [68], we reimplemented the Jaeger *et al.* model of gap gene regulation (M^{1D-P}) using the finite element method (FEM). This model represents six gene products as state variables: Cad, Gt, Hb, Kr, Kni, and Tll [13]. A seventh protein, Bcd (Bcd), is maintained at a constant concentration during gap gene patterning and is represented as a spatially heterogeneous stationary input [13], [63]. Each of the state variables is represented by a PDE,

$$\frac{\partial c_a}{\partial t} = D_a \nabla^2 c_a + R_a \phi_a(u_a) - \lambda_a c_a, \quad (1)$$

where c_a is the concentration of protein a , the first term on the right hand side represents diffusion, the second term represents gene expression, and the third term represents first order decay [13]. D_a is the diffusion constant of protein a and λ_a is the first order decay constant of protein a . R_a is the maximal rate of gene expression of proteins a and Φ_a is a sigmoid function,

$$\phi_a(u_a) = \frac{1}{2} \left(\frac{u_a}{\sqrt{u_a^2 + 1}} + 1 \right), \quad (2)$$

which ranges from zero to one and accepts a regulatory argument u_a :

$$u_a = h_a + \sum_b w_{b,a} c_b. \quad (3)$$

Here, h_a is a minimal regulatory threshold for expression, $w_{b,a}$ is an element in the regulatory matrix W representing the influence of protein b on the expression of protein a (ranging from -0.2 to 0.2), and c_b is the local concentration of protein b . There are six PDEs representing protein proteins $a = \text{Cad, Gt, Hb, Kr, Kni, Tll}$ (eqn. 1). In each PDE, the regulatory effects of all seven proteins, $b = [41 \text{ Kr, Kni, Tll, Bcd}]$, control protein expression (eqns. 2–3). PDEs are numerically solved using the FEM implemented in the software package COMSOL Multiphysics 3.5a [69]. Except for GRN parameters $w_{b,a}$, these parameters are fixed at values in Jaeger *et al.* [13] and may be found in [Table S2](#).

Note that previous 1D models were simulated by the spatially-discretized ordinary differential equations using the finite difference method: concentrations were tracked at uniformly-distributed nodes (nuclei) along the AP axis and diffusive fluxes across the Δx inter-node distance were modeled as a first-order differential equations. As such, previously reported diffusion parameters (\check{D}_a) were in units of inverse time [1/t]. To convert these parameters to diffusion constants (D_a) with units of squared-length-per-time [L^2/t], we multiplied \check{D}_a by $(\Delta x)^2$. To compute Δx , we took into account the length of the original model's domain (0.57 EL) and the number of nodes where the finite difference model was solved (58 nuclei). From these values, we approximated Δx as $0.57\text{EL}/57$. The

model spans 0.35–0.92 or 0.57 EL and is divided into 57 intervals between 58 nodes. In the case of the 3D geometry, we further accounted for the curvature of the embryo in our approximation of Δx . Scaling the embryo length to unity (1 EL), we observed an arc length of 1.14 along the lateral AP. Upon the assumption that curvature was uniformly distributed along the AP axis, Δx was computed as $(0.57/1.14)\text{EL}/57$. The approach slightly overestimates D_a in the 3D model relative to 1D because most curvature occurs at the AP extrema and not the trunk, but this does not translate to a large impact on AP patterning versus 1D. Whereas finite difference models explicitly modify \check{D}_a values to account for mitotic nuclear division and the halving of Δx , the continuous FEM representation renders diffusion constants independent of nuclear density. It should be noted that this representation does not account for reduced effective diffusivity due to increased nuclear trapping. While nuclear density has been linked with decreased effective diffusivity in some simulations of Bcd diffusion [70], Grimm and Wieschaus found that transcription factor distributions are largely independent of nuclear density [71]. 3D nuclear density distributions have been published [47] and nuclear density-dependent diffusion is an area for further investigation.

We developed two FEM meshes on which to simulate spatiotemporal gap gene evolution. A 1D linear domain represents the 35–92% AP axis, and replicates the domain used in previous models [13]. By scaling diffusion constants and choosing initial conditions, the 1D domain also represents the 0–100% AP length (M^{1D-F}). A 3D mesh modified from the VE geometry represents a realistic embryonic geometry. Though the embryonic syncytium includes the yolk interior of the embryo, nuclei are located within the

periplasmic domain of the exterior surface[10], [49]. Cytoplasmic viscosity increases in the embryonic interior and is presumed to limit effective diffusion of gap gene products to the 2D layer in the periplasmic volume containing the nuclei. While some gap gene products may diffuse into yolk, this process may be considered as part of the decay terms, λ_a . We took this into account when constructing the 3D domain. The reaction-diffusion equations (eqns. 1–3) are implemented as weak form PDEs on a 2D manifold (Fig. S1); this manifold is “wrapped” around the 3D embryonic geometry in 3D model implementations ($M_{Bcd}^{3D 1D}$, $M_{Bcd}^{3D 3D}$, $M_{Bcd}^{3D S}$).

Though the 3D domain is a closed surface without AP flux boundaries, the partial (M^{1D-P}) and full (M^{1D-F}) 1D domains are bounded at both termini by zero-flux conditions. These internal boundaries are unrealistic in the case of the partial AP length domain as there are no such physical barriers in the embryo; they were introduced in previous gap gene models to help account for artifacts in previously inferred GRNs [14], [42]–[44]. In full length 1D models the anterior and posterior ends of the embryo are realistically represented by zero-flux boundaries.

Numerical integration of PDEs requires specification of initial conditions as well as boundary conditions. For purposes of model comparison, we chose initial conditions specified in previous models [13]. On both 1D and 3D domains, the proteins Gt, Kni, Kr, and Tll have initial uniform concentrations of zero. Jaeger *et al.* provide initial non-uniform 1D distributions for Cad and Hb (Fig. 3a) [13]. These distributions span the entire AP length and provide initial conditions for both the partial and full length

domains. Jaeger *et al.* also provide a constant exponential 1D Bcd distribution for the full AP length. These 1D distributions were used as initial conditions in the 1D models (M^{1D-F} and M^{1D-P}). They were projected onto the 3D domain to approximate full 3D initial conditions (M_{Bcd1D}^{3D} , Fig. 3b–d). This projection was performed using built-in interpolation tools in the Comsol package. Provided AP-coordinates and corresponding concentration values, Comsol created a linear interpolant of DV-symmetric concentration values along the AP-axis of the 3D geometry.

While the Bcd data provided by Jaeger *et al.* describes the lateral AP distribution of Bcd, it fails to capture the observed DV asymmetry found in embryonic Bcd. Though sufficient for a 1D model (Fig. 3a), the resulting 3D distribution (Fig. 3b) qualitatively disagrees with VE data (Fig. 3e). We therefore built an interpolating function from the VE Bcd data and used this interpolant when simulating the model (M_{Bcd3D}^{3D}). Again, we used Comsol's interpolation functionality. However, this interpolant required full 3D specification of coordinates. We used the coordinates of nuclei and corresponding Bcd concentration values provided in the VE. Because the software does not support interpolation on a 2D boundary (the periplasmic space) in a 3D geometry, we used nearest-neighbor interpolation (Fig. 3e). Because this Bcd distribution is represented in the model as a static interpolant, noise in the data (and hence the interpolant) is not smoothed by diffusion and decay. Initial attempts at directly importing VE Bcd data resulted in persistent asymmetries and mottled distributions inconsistent with data (Fig. 4, column 3). In an ideal situation, inter-embryo variability would be averaged out of VE data. However, the data set was generated with few replicates (13 embryos for Bcd [49])

and spatial noise remained. To remove this noise from the interpolant, we first fit a steady-state source-diffusion-decay (SDD) model of Bcd production [18] to VE Bcd data on the 3D domain (Fig. 4a, column 1). Once we had obtained agreement between this regularized Bcd distribution and the data, we used the solution of the SDD model to create a new interpolant. This smoothed interpolant shown in Figure 3f and $M_{Bcd3D-S}^{3D}$'s output (Fig. 4b–g, columns 4–5) compares favorably with the results M_{Bcd3D}^{3D} (Fig. 4b–g, columns 3).

Spatiotemporal regulation of gap gene expression spans the mitotic nuclear division between nuclear cycle 13 and 14a. For purposes of comparison, we chose to simulate the same time-course as previous models. We begin by simulating the conclusion of cycle 13 for sixteen minutes, mitosis for five minutes, and continue to simulate cycle 14a for the remaining forty-nine minutes [13]. The reaction-diffusion equations (eqn. 1–3) describe the model during interphase. During mitosis, gene expression (the second term in eqn. 1) is set to zero. Molecules may diffuse and decay, but they are not transcribed or translated while the chromatin is compacted for mitotic division.

This set of initial and boundary conditions, coupled with the reaction-diffusion equations and a geometric domain, constitutes a numerically soluble model. To calculate model error, we used a straightforward root mean squared error cost function:

$$J_{RMSE} = \sum_{t=1}^6 \sum_{a=1}^6 \sum_{i=1}^n \sqrt{\frac{(c_{a,mod}(\theta, i, t) - c_{a,exp}(i, t))^2}{6n}} \quad (5)$$

Here, θ is the GRN parameter set, n is the number of data points in the 35%–92% EL region of the embryo, a is the index of protein species, i is the index of n nuclear coordinates, and t is the time index. This function sums the root squared error between model output from a given GRN, $c_{a,mod}(\theta, i, t)$, and experimental data, $c_{x,exp}(i, t)$, over data points i , model proteins a , and time t .

M^{1D-P} was originally fit to immunofluorescence data in Jaeger *et al.* [13]. As a result, both the model's concentration units and GRN parameters are scaled to reflect observed relative intensity ranges of those data. To facilitate fitting between models utilizing Jaeger *et al.*'s parameters and VE data, we pre-scaled the VE data to agree with the initial conditions reported by Jaeger *et al.* This was performed by optimizing scaling factors A_a and offsets b_a such that the difference between Jaeger *et al.*'s initial conditions and the VE data was minimized,

$$\min_{A,b} \sqrt{\left((A_a c_{VE,a} - b_a) - c_{Jaeger,a} \right)^2} \quad (6)$$

The resulting scaling was applied to the VE data, allowing for direct comparison of model outputs. VE protein data is unavailable for Cad and Tll. For the former, we substituted expression data used by Jaeger *et al.* to fit the original model [13]. For the latter, we substituted Tll mRNA data from the VE and scaled it according to **eqn. 6**.

Optimization

Using the cost function (eqn. 5), we optimized the full 1D and 3D models against scaled VE data using the Optimization Toolbox in MATLAB R2009a [72]. We began with local searches of the GRN weight matrix W (containing 42 parameters) using the constrained nonlinear minimization function `fmincon()`. We initialized these searches at the best-fit inferred GRN parameter set of the original modeling study and bounded all parameters within the interval $[-0.2, 0.2]$ [13]. Parameter and cost function tolerances for stopping criteria were set to zero and the search was allowed to progress for 4200 model evaluations (100 evaluations per parameter), resulting in arrival at local minima. In the case of the DV-asymmetric Bcd model (M_{Bcd3D}^{3D}), we subsequently included this locally optimal GRN in the initial population of a global search using genetic algorithms (GAs).

We used the GA as implemented in MATLAB. The population of size twenty genomes (parameter sets) was initialized with nineteen randomized parameter sets and the locally-optimized parameter set found for M_{Bcd3D}^{3D} . Stopping criteria were specified as a maximum of 100 generations or failure to improve cost function values above a tolerance of 10^{-6} . The latter criterion increments a “stall” counter for each generation that fails to improve the score, ending the GA when the counter reaches fifty [72]. This algorithm

was used to search the parameter space while fitting the 3D model incorporating DV-asymmetric Bcd ($M_{Bcd3D-S}^{3D}$).

References

1. St Johnston D, Nusslein-Volhard C (1992) The origin of pattern and polarity in the *Drosophila* embryo. *Cell* 201–219.
2. Jaeger J (2011) The gap gene network. *Cellular and Molecular Life Sciences* 243–274.
3. Kopp A, Blackman R, Duncan I (1999) Wingless, decapentaplegic and EGF receptor signaling pathways interact to specify dorso-ventral pattern in the adult abdomen of *Drosophila*. *Development* 126: 3495–3507.
4. Umulis D, Serpe M, O'Connor M, Othmer H (2006) Robust, bistable patterning of the dorsal surface of the *Drosophila* embryo. *Proceedings of the National Academy of Sciences of the United States of America* 103: 11613–11618.
5. Anderson K (1987) Dorsal Ventral Embryonic Pattern Genes of *Drosophila*. *Trends in Genetics* 3: 91–97.
6. Reinitz J, Sharp D (1995) Mechanism of Eve stripe formation. *Mechanisms of Development* 133–158.
7. Surkova S, Kosman D, Kozlov K, Manu , Myasnikova E, et al. (2008) Characterization of the *Drosophila* segment determination morphome. *Developmental Biology* 844–862.
8. Akam M (1987) The Molecular-Basis for Metameric Pattern in the *Drosophila* Embryo. *Development* 101: 1–22.
9. Ingham P, Arias A (1992) Boundaries and fields in early embryos. *Cell* 68: 221–235.
10. Counce S (1961) Analysis of Insect Embryogenesis. *Annual Review of Entomology* 6: 295–312.
11. Jaeger J, Sharp D, Reinitz J (2007) Known maternal gradients are not sufficient for the establishment of gap domains in *Drosophila melanogaster*. *Mechanisms of Development* 108–128.
12. Irish V, Lehmann R, Akam M (1989) The *Drosophila* posterior-group gene Nanos functions by repressing Hunchback activity. *Nature* 338: 646–648.
13. Jaeger J, Surkova S, Blagov M, Janssens H, Kosman D, et al. (2004) Dynamic control of positional information in the early *Drosophila* embryo. *Nature* 368–371.
14. Jaeger J, Blagov M, Kosman D, Kozlov K, Manu , et al. (2004) Dynamical analysis of regulatory interactions in the gap gene system of *Drosophila melanogaster*. *Genetics* 1721–1737.
15. Small S, Kraut R, Hoey T, Warrior R, Levine M (1991) Transcriptional regulation of a pair-rule stripe in *Drosophila*. *Genes & Development* 827–839.

16. Driever W, Ma J, Nusslein-Volhard C, Ptashne M (1989) Rescue of Bicoid mutant *Drosophila* embryos by Bicoid fusion proteins containing heterologous activating sequences. *Nature* 149–154.
17. Driever W, Nusslein-Volhard C (1989) The Bicoid protein is a positive regulator of Hunchback transcription in the early *Drosophila* embryo. *Nature* 138–143.
18. Driever W, Nusslein-Volhard C (1988) The Bicoid protein determines position in the *Drosophila* embryo in a concentration-dependent manner. *Cell* 95–104/
19. Lehmann R, Nusslein-Volhard C (1987) Hunchback, a gene required for segmentation of the anterior and posterior region of the *Drosophila* embryo. *Developmental Biology* 119: 402–417.
20. Jurgens G, Wieschaus E, Nusslein-Volhard C, Kluding H (1984) Mutations affecting the pattern of the larval cuticle in *Drosophila melanogaster* 2 Zygotic loci on the 3rd chromosome. *Wilhelm Roux Archives of Developmental Biology* 193: 283–295.
21. Nusslein-Volhard C, Wieschaus E, Kluding H (1984) Mutations affecting the pattern of the larval cuticle in *Drosophila melanogaster* 1 Zygotic loci on the 2nd chromosome. *Wilhelm Roux Archives of Developmental Biology* 193: 267–282.
22. Wieschaus E, Nusslein-Volhard C, Jurgens G (1984) Mutations affecting the pattern of the larval cuticle in *Drosophila melanogaster* 3 Zygotic loci on the X-chromosome and the 4th chromosome. *Wilhelm Roux Archives of Developmental Biology* 193: 296–307.
23. Wieschaus E, Nusslein-Volhard C, Kluding H (1984) Krüppel, a gene whose activity is required early in the zygotic genome for normal embryonic segmentation. *Developmental Biology* 104: 172–186.
24. Nusslein-Volhard C, Wieschaus E (1980) Mutations affecting segment number and polarity in *Drosophila*. *Nature* 287: 795–801.
25. Jackle H, Tautz D, Schuh R, Seifert E, Lehmann R (1986) Cross-regulatory interactions among the gap genes of *Drosophila*. *Nature* 324: 668–670.
26. Nusslein-Volhard C, Frohnhofer H, Lehmann R (1987) Determination of the anteroposterior polarity in *Drosophila*. *Science* 238: 1675–1681.
27. Harding K, Levine M (1988) Gap genes define the limits of Antennapedia and Bithorax gene-expression during early development in *Drosophila*. *Embo Journal* 7: 205–214.
28. Tautz D (1988) Regulation of the *Drosophila* segmentation gene Hunchback by 2 maternal morphogenetic centers. *Nature* 332: 281–284.
29. Hulskamp M, Pfeifle C, Tautz D (1990) A morphogenetic gradient of Hunchback protein organizes the expression of the gap genes Krüppel and Knirps in the early *Drosophila* embryo. *Nature* 346: 577–580.
30. Bronner G, Jackle H (1991) Control and function of terminal gap gene activity in the posterior pole region of the *Drosophila* embryo. *Mechanisms of Development* 205–211.

31. Eldon E, Pirrotta V (1991) Interactions of the *Drosophila* gap gene Giant with maternal and zygotic pattern-forming genes. *Development* 111: 367.
32. Kraut R, Levine M (1991) Mutually repressive interactions between the gap genes Giant and Krüppel define the middle body regions of the *Drosophila* embryo. *Development* 111: 611–621.
33. Capovilla M, Eldon E, Pirrotta V (1992) The giant gene of *Drosophila* encodes a B-zip DNA-binding protein that regulates the expression of other segmentation gap genes. *Development* 114: 99–112.
34. Struhl G, Johnston P, Lawrence P (1992) Control of *Drosophila* body pattern by the Hunchback morphogen gradient. *Cell* 69: 237–249.
35. Hulskamp M, Lukowitz W, Beermann A, Glaser G, Tautz D (1994) Differential regulation of target genes by different alleles of the segmentation gene Hunchback in *Drosophila*. *Genetics* 138: 125–134.
36. Simpsonbrose M, Treisman J, Desplan C (1994) Synergy between the Hunchback and Bicoid morphogens is required for anterior patterning in *Drosophila*. *Cell* 78: 855–865.
37. Ashyraliyev M, Siggins K, Janssens H, Blom J, Akam M, et al. (2009) Gene Circuit Analysis of the Terminal Gap Gene *huckebein*. *Plos Computational Biology* 5(10): e1000548.
38. Manu , Surkova S, Spirov A, Gursky V, Janssens H, et al. (2009) Canalization of Gene Expression and Domain Shifts in the *Drosophila* Blastoderm by Dynamical Attractors. *Plos Computational Biology* 7(3): e1000049.
39. Manu , Surkova S, Spirov A, Gursky V, Janssens H, et al. (2009) Canalization of Gene Expression in the *Drosophila* Blastoderm by Gap Gene Cross Regulation. *Plos Biology* 591–603.
40. Alves F, Dilao R (2006) Modeling segmental patterning in *Drosophila*: Maternal and gap genes. *Journal of Theoretical Biology* 241: 342–359.
41. Sanchez L, Thieffry D (2001) A logical analysis of the *Drosophila* gap-gene system. *Journal of Theoretical Biology* 212(1): 115–141.
42. Perkins T, Jaeger J, Reinitz J, Glass L (2006) Reverse engineering the gap gene network of *Drosophila melanogaster*. *Plos Computational Biology* 417–428.
43. Ashyraliyev M, Jaeger J, Blom J (2008) Parameter estimation and determinability analysis applied to *Drosophila* gap gene circuits. *BMC Systems Biology* 2: 83.
44. Fomekong-Nanfack Y, Postma M, Kaandorp J (2009) Inferring *Drosophila* gap gene regulatory network: a parameter sensitivity and perturbation analysis. *BMC Systems Biology* 3: 94.
45. Fomekong-Nanfack Y, Kaandorp J, Blom J (2007) Efficient parameter estimation for spatio-temporal models of pattern formation: case study of *Drosophila melanogaster*. *Bioinformatics* 23: 3356–3363.

- 46.**Jaeger J, Reinitz J (2006) On the dynamic nature of positional information. *Bioessays* 1102–1111.
- 47.**Keranen S, Fowlkes C, Luengo Hendriks C, Sudar D, Knowles D, et al. (2006) Three-dimensional morphology and gene expression in the *Drosophila* blastoderm at cellular resolution II: dynamics. *Genome Biology* 7: R124.
- 48.**Luengo Hendriks C, Keranen S, Fowlkes C, Simirenko L, Weber G, et al. (2006) Three-dimensional morphology and gene expression in the *Drosophila* blastoderm at cellular resolution I: data acquisition pipeline. *Genome Biology* 7: R123.
- 49.**Fowlkes C, Luengo Hendriks C, Keranen S, Weber G, Rubel O, et al. (2008) A quantitative spatiotemporal atlas of gene expression in the *Drosophila* blastoderm. *Cell* 364–374.
- 50.**Vakulenko S, Manu , Reinitz J, Radulescu O (2009) Size Regulation in the Segmentation of *Drosophila*: Interacting Interfaces between Localized Domains of Gene Expression Ensure Robust Spatial Patterning. *Physical Review Letters* 103: 168102–5.
- 51.**Gursky V, Jaeger J, Kozlov K, Reinitz J, Samsonov A (2004) Pattern formation and nuclear divisions are uncoupled in *Drosophila* segmentation: comparison of spatially discrete and continuous models. *Physica D-Nonlinear Phenomena* 286–302.
- 52.**Nusslein-Volhard C (1991) Determination of the embryonic axes of *Drosophila*. *Development* 113: 1–10.
- 53.**Carroll S, Winslow G, Twombly V, Scott M (1987) Genes that control dorsoventral polarity affect gene-expression along the anteroposterior axis of the *Drosophila* embryo. *Development* 99: 327–332.
- 54.**Okabe-Oho Y, Murakami H, Oho S, Sasai M (2009) Stable, Precise, and Reproducible Patterning of Bicoid and Hunchback Molecules in the Early *Drosophila* Embryo. *Plos Computational Biology* 5(8): e1000486.
- 55.**Deng JY, Wang W, Lu LJ, Ma J (2010) A Two-Dimensional Simulation Model of the Bicoid Gradient in *Drosophila*. *Plos One* 5:
- 56.**He F, Saunders T, Wen Y, Cheung D, Jiao R, et al. (2010) Shaping a Morphogen Gradient for Positional Precision. *Biophysical Journal* 697–707.
- 57.**Jaeger J (2010) A matter of timing and precision. *Molecular Systems Biology* 6: 427.
- 58.**Jaeger J (2009) Modelling the *Drosophila* embryo. *Molecular Biosystems* 5: 1549–1568.
- 59.**Bieler J, Pozzorini C, Naef F (2011) Whole-embryo modeling of early segmentation in *Drosophila* identifies robust and fragile expression domains. *Biophysical Journal* 101: 287–296.
- 60.**Munteanu A, Sole R (2008) Neutrality and Robustness in Evo-Devo: Emergence of Lateral Inhibition. *Plos Computational Biology* 4(11): e1000226.

61. Wagner A (2008) Robustness and evolvability: a paradox resolved. *Proceedings of the Royal Society B-Biological Sciences* 91–100.
62. Wagner A (2005) Distributed robustness versus redundancy as causes of mutational robustness. *Bioessays* 176–188.
63. Gregor T, Wieschaus E, McGregor A, Bialek W, Tank D (2007) Stability and nuclear dynamics of the bicoid morphogen gradient. *Cell* 141–152.
64. Gregor T, Bialek W, van Steveninck R, Tank D, Wieschaus E (2005) Diffusion and scaling during early embryonic pattern formation. *Proceedings of the National Academy of Sciences of the United States of America* 18403–18407.
65. Kanodia J, Rikhy R, Kim Y, Lund V, DeLotto R, et al. (2009) Dynamics of the Dorsal morphogen gradient. *Proceedings of the National Academy of Sciences of the United States of America* 21707–21712.
66. Liberman L, Reeves G, Stathopoulos A (2009) Quantitative imaging of the Dorsal nuclear gradient reveals limitations to threshold-dependent patterning in *Drosophila*. *Proceedings of the National Academy of Sciences of the United States of America* 22317–22322.
67. Wang C, Lehmann R (1991) Nanos is the localized posterior determinant in *Drosophila*. *Cell* 637–647.
68. Umulis D, Shimmi O, O'Connor M, Othmer H (2010) Organism-Scale Modeling of Early *Drosophila* Patterning via Bone Morphogenetic Proteins. *Developmental Cell* 18: 260–274.
69. COMSOL Multiphysics® 3.5a. COMSOL AB, Palo Alto, CA, USA.
70. Sample C, Shvartsman S (2010) Multiscale modeling of diffusion in the early *Drosophila* embryo. *Proceedings of the National Academy of Sciences of the United States of America* 107: 10092–10096.
71. Grimm O, Wieschaus E (2010) The Bicoid gradient is shaped independently of nuclei. *Development* 137: 2857–2862.
72. MATLAB® R2009a. The Mathworks, Natick, MA, USA.

Supplemental Movies available at:

<http://www.plosone.org/article/info%3Adoi%2F10.1371%2Fjournal.pone.0026797>

Supplemental Figures below.

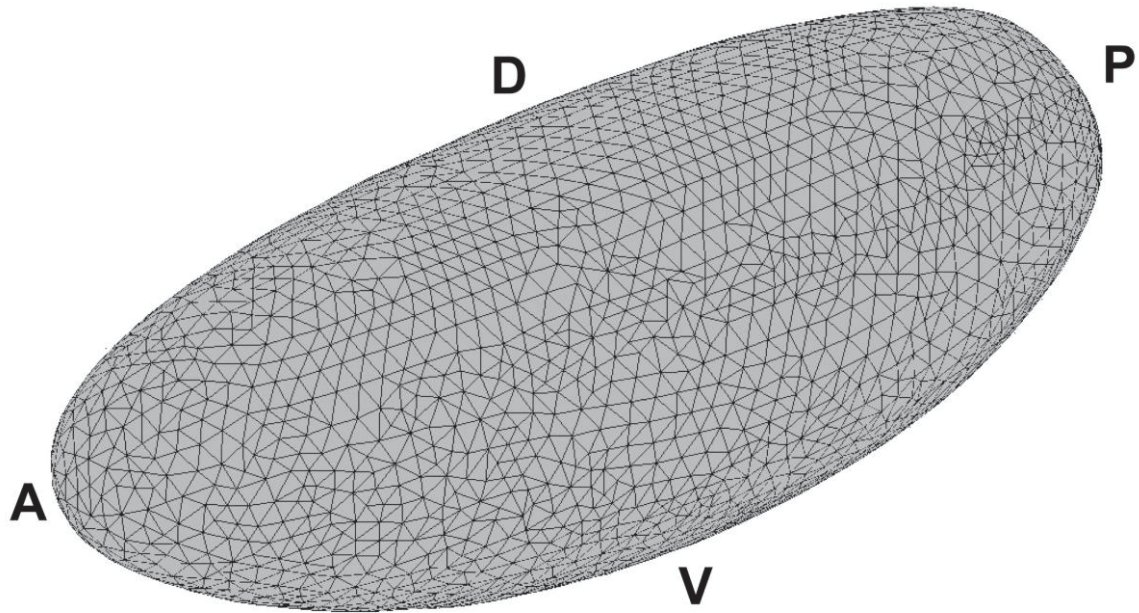


Figure S1. The VirtualEmbryo geometry.

A three-quarters view of the embryonic geometry with anterior (A), posterior (P), dorsal (D) and ventral (V) poles indicated.

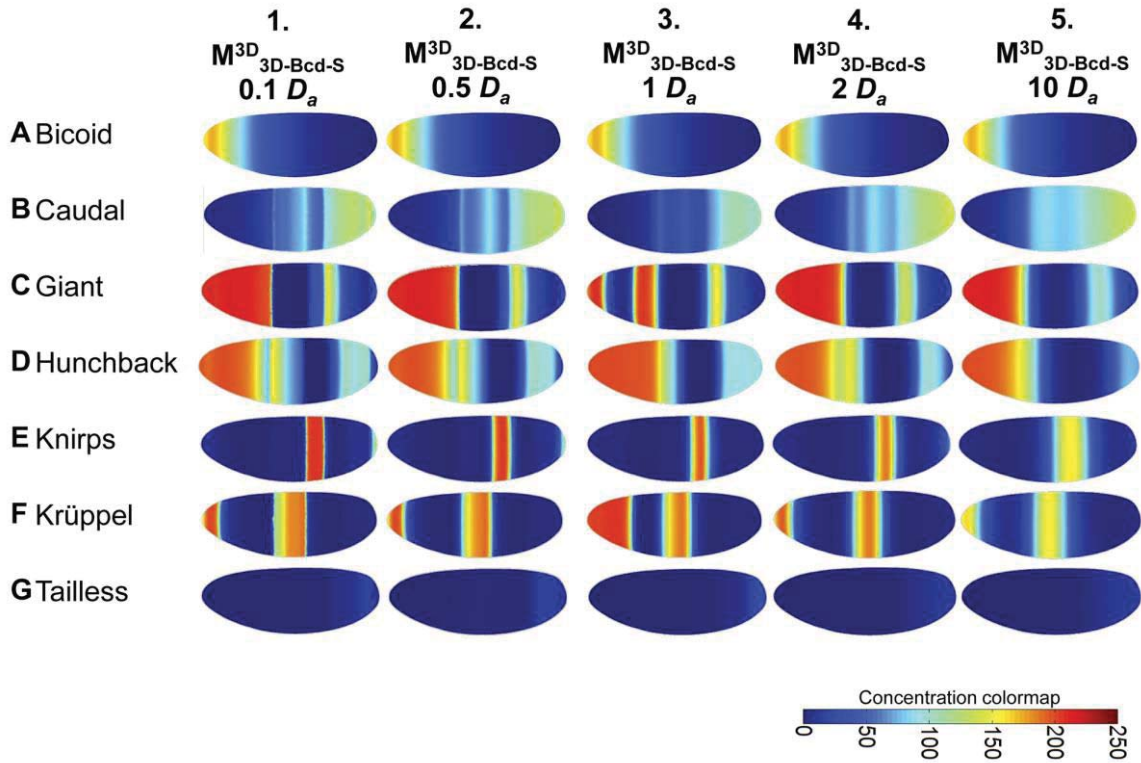


Figure S2. Scaled diffusion constants in DV-symmetric Bcd model M_{Bcd1D}^{3D} .

The model is insensitive to small changes in the diffusion constant. (A–G) Lateral view of VE geometry is shown in rows A–G (Gt, Hb, Kni, Kr, Tll at $t=70$ min, Cad at $t=56$ min); Column 1 displays output from M_{Bcd1D}^{3D} evaluated with GRN P_{VE}^{1D-F} and diffusion constants D_a scaled by 0.1; Column 2 displays output from M_{Bcd1D}^{3D} evaluated with GRN P_{VE}^{1D-F} and diffusion constants D_a scaled by 0.5; Column 3 displays output from M_{Bcd1D}^{3D} evaluated with GRN P_{VE}^{1D-F} and diffusion constants D_a scaled by 1; Column 4 displays output from M_{Bcd1D}^{3D} evaluated with GRN P_{VE}^{1D-F} and diffusion constants D_a scaled by 2; Column 5 displays output from M_{Bcd1D}^{3D} evaluated with GRN P_{VE}^{1D-F} and diffusion constants D_a scaled by 10.

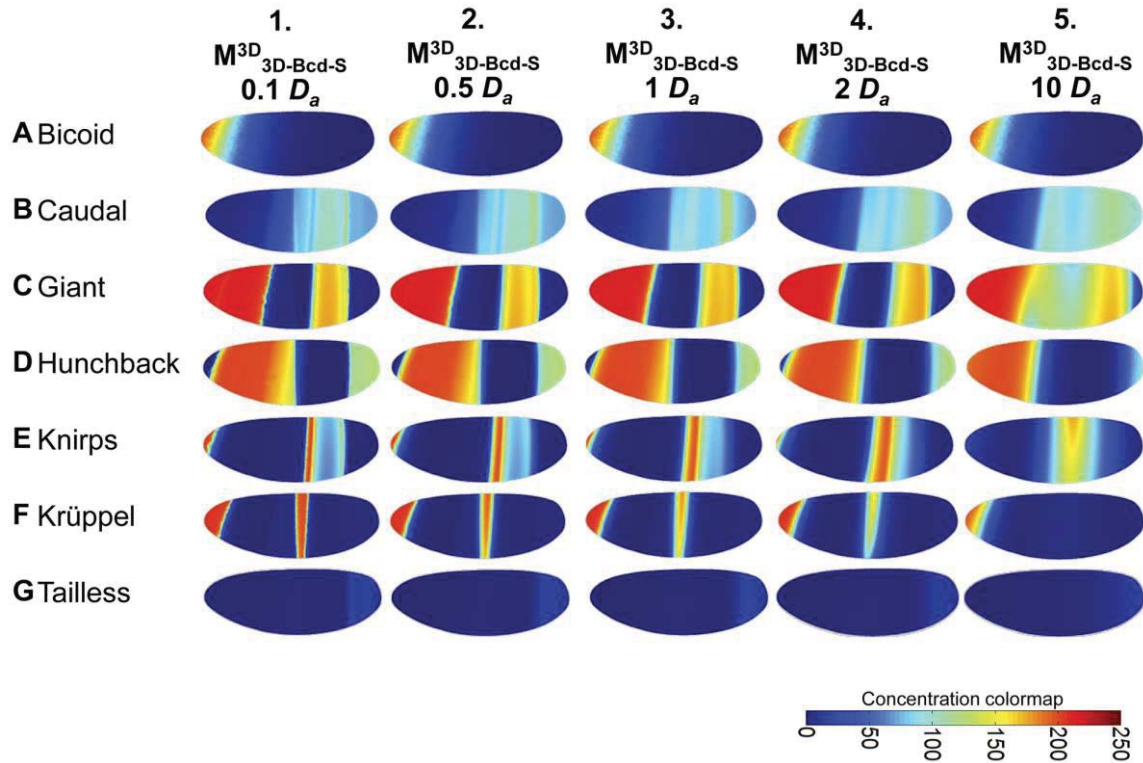


Figure S3. Scaled diffusion constants in DV-asymmetric Bcd model $M_{Bcd3D-S}^{3D}$.

The model is insensitive to small changes in the diffusion constant. (A–G) Lateral view of VE geometry is shown in rows A–G (Gt, Hb, Kni, Kr, Tll at $t=70$ min, Cad at $t=56$ min); Column 1 displays output from $M_{Bcd3D-S}^{3D}$ evaluated with GRN $P_{Bcd3D-S}^{3D}$ and diffusion constants D_a scaled by 0.1; Column 2 displays output from $M_{Bcd3D-S}^{3D}$ evaluated with GRN $P_{Bcd3D-S}^{3D}$ and diffusion constants D_a scaled by 0.5; Column 3 displays output from $M_{Bcd3D-S}^{3D}$ evaluated with GRN $P_{Bcd3D-S}^{3D}$ and diffusion constants D_a scaled by 1; Column 4 displays output from $M_{Bcd3D-S}^{3D}$ evaluated with GRN $P_{Bcd3D-S}^{3D}$ and diffusion constants D_a scaled by 2; Column 5 displays output from $M_{Bcd3D-S}^{3D}$ evaluated with GRN $P_{Bcd3D-S}^{3D}$ and diffusion constants D_a scaled by 10.

CHAPTER 4. THE IMPORTANCE OF CHOOSING PROPER OBJECTIVE FUNCTIONS FOR SPATIOTEMPORAL MODEL OPTIMIZATION

4.1 A Note About this Article

The introductory material in Chapter 1 contains an expanded version of Sections 1-2 of this publication.

PUBLICATION

Hengenius, JB, Gribskov, M, Rundell, AE, Umulis, DM. (2014) Making models match measurements: Model optimization for morphogen patterning networks. *Seminars in Cell and Developmental Biology* 35C:109-123

Making models match measurements: Model optimization for morphogen patterning networks

JB Hengeni^c
 MR Gribskov^c
 AE Rundell^a
 DM Umulis^{b,1}

^aWeldon School of Biomedical Engineering, Purdue University. 206 S. Martin Jischke Drive West Lafayette, IN 47907

^bDepartment of Agricultural and Biological Engineering, Purdue University. 225 S. University Street West Lafayette, IN 47907

^cDepartment of Biological Sciences, Purdue University. 247 S. Martin Jischke Drive West Lafayette, IN 47907

¹Correspondence: dumulis@purdue.edu

Abstract

Mathematical modeling of developmental signaling networks has played an increasingly important role in the identification of regulatory mechanisms by providing a sandbox for hypothesis testing and experiment design. Whether these models consist of an equation with a few parameters or dozens of equations with hundreds of parameters, a prerequisite to model-based discovery is to bring simulated behavior into agreement with observed data via parameter estimation. These parameters provide insight into the system (*e.g.*, enzymatic rate constants describe enzyme properties). Depending on the nature of the model fit desired - from qualitative (relative spatial positions of phosphorylation) to

¹Bcd – Bicoid; Gt – Giant; Kni – Knirps; AP – anterior-posterior; SDD – source diffusion decay; GRN – genetic regulatory network; DV – dorsal ventral; RMSE – root mean square error; SSE – sum of square error; OLS – least squares error; MSE – mean square error; MAE – mean absolute error; PCC – Pearson correlation coefficient; PDF – probability density function; K-S statistic – Kolmogorov-Smirnov statistic; CDF – cumulative density function; RE – relative entropy; K-L divergence – Kullbeck-Leibler divergence; wSSE – weighted sum of square error; nRMSE – normalized root mean square error; DSW (DTW) – dynamic space (time) warping; SA – sensitivity analysis; LHS – Latin hypercube sampling; MB-ODE – model based optimal design of experiments

quantitative (exact agreement of spatial position and concentration of gene products) - different measures of data-model mismatch are used to estimate different parameter values, which contain different levels of usable information and/or uncertainty. To facilitate the adoption of modeling as a tool for discovery alongside other tools such as genetics, immunostaining, and biochemistry, careful consideration needs to be given to how well a model fits the available data, what the optimized parameter values mean in a biological context, and how the uncertainty in model parameters and predictions plays into experiment design. The core discussion herein pertains to the quantification of model-to-data agreement, which constitutes the first measure of a model's performance and future utility to the problem at hand. Integration of this experimental data and the appropriate choice of objective measures of data-model agreement will continue to drive modeling forward as a tool that contributes to experimental discovery. The *Drosophila melanogaster* gap gene system, in which model parameters are optimized against *in situ* immunofluorescence intensities, demonstrates the importance of error quantification, which is applicable to a wide array of developmental modeling studies.

Key words: Developmental biology, mathematical modeling, dynamic modeling, objective functions, parameter estimation, morphogens

1. Introduction

Mathematical models of complex networks in development exist in an “uncanny valley”; many models look and behave *almost* like the natural systems they are designed to

simulate, but they display imperfections that make their predictions suspect. The disparity between a model result and the actual system may be a small yet systematic mismatch, the complete absence of frequently observed experimental features, or the prediction of unviable conditions (*e.g.*, fatal pH) despite good agreement with experimental data. This “uncanny valley” for models might suggest that modeling is a distraction that interferes with experimental discovery because the model attempts to show how the system works in quantitative detail, yet models are always deficient. Among model-builders it is understood that simulations will always be simplifications incapable of reproducing all experimental behaviors; however, imperfect models still promote greater understanding and have, more recently, been informing experimental design and testing assumptions when experiments are infeasible[35].

Central to modeling are the needs to quantify how well a model agrees with experimental data and to identify where it might disagree. Quantification of model-data agreement is determined by an objective function that measures the “error” of the model; however there are many ways to measure the error and the choice of objective to measure model-data differences depends on the type of data, the type of model, and the question being asked. Herein we review diverse objective functions for the calculation of model-data error and identify each function’s strengths and weaknesses in the context of developmental pattern formation by morphogens.

Mathematical models of varying complexity are used to represent diverse dynamic phenomena in the biological sciences. The specific type of model determines both the type of data needed to inform the model and the optimal objective functions to relate the

model to the data. A dynamic model describes change in the system state over a time course of interest; it contains explicit mechanistic descriptions of the system and rules for updating the state of the system in time [20]. Independent of the mechanistic description, the behavior of the model depends on the initial conditions of the system (*e.g.*, simulated molecular concentrations at time zero). Developmental models often simulate spatially heterogeneous systems; in these cases the shape of the spatial domain also affects outcome. Mechanistic dynamic models are parametric[21]. The parameters are constant values that define the behavior of the system and often have biophysical interpretations. For example, binding rate constants are parameters of receptor binding models[22,23]. To determine the validity of a model, parameter estimation must be used to bring the model into agreement with data[24]. This often involves iteratively simulating the model with different parameter values and comparing the resultant simulation to data. Parameters that yield simulated values minimally different (or maximally similar) to data are retained[24-26]. The difficulty of this parameter search depends on the range each parameter is allowed to assume, the number of parameters to be estimated, and the covariance of parameters with model output[27].

Mechanistic models should not be confused with statistical models (sometimes known as phenomenological models). Statistical models (*e.g.*, linear or logistic regression) quantify correlation among observable data. This knowledge often proves useful in hypothesis generation, but the predictive power of statistical models is limited to interpolation within the range of existing data [36]. Conversely, mechanistic models encode suppositions about the nature of the underlying system. As such, they may be

used to extrapolate beyond the range of current data and provide predictions *given that the modeled mechanism is accurate*. Mechanistic models are the primary context for the comparison of fitness metrics herein.

The quality of the model and the uncertainty of its predictions depend on the type and quality of the data used for the training and optimization of the model. Experimental data common in the analysis of morphogen signaling systems may take several forms depending on the nature of the assays used. Specifically, qualitative data encodes nonnumeric descriptors of the morphogen and targets of interest; semi-quantitative data is predominantly ratiometric such as the relative intensity of a stained molecule or intensity of a western blot; and quantitative data provides information of specific, measured quantities with associated uncertainty. As the quantitative content of the data increases, the associated uncertainties typically decrease. This provides more stringent constraints that improve the resulting model (see Pargett *et al.*, 2013 for further details[31]).

Once mechanistic models are trained or optimized to the supporting data, they can be used to address a number of important questions. Specifically, a parameterized model can be used to infer the behavior of hard-to-observe molecules, perform quantitative simulations of qualitative hypotheses, or generate new hypotheses based on model behavior. In Section 2 we focus on the challenges that exist in most model optimization problems and then utilize a specific example in the *Drosophila* gap gene network as an illustrative case study.

2. Model complexity and parameter estimation

Dynamic modeling allows insight into systems' behaviors, but this insight requires optimized physiochemical parameter values. Several challenges stand between a newly defined mechanistic model and the parameter values that make it biologically relevant. This parameter estimation problem grows exponentially as the number of modeled (and parameterized) biochemical interactions grows.

Model and objective function in hand, optimization proceeds in several steps. First, the unknown parameter values are enumerated and constrained to biologically feasible ranges (*e.g.*, a kinetic constant or diffusion constant cannot be negative). Second, a stochastic and incomplete search is performed within this feasible region of the parameter space while ignoring biologically impossible parameter value combinations. Third, resultant parameter sets are ranked according to the chosen objective function. Finally, investigators decide whether the fit is “good enough.” If it is, they stop; if not, they repeat the above search.

The magnitude of these difficulties grows with the size of the model and the increasing number of unknown parameters. As the number of parameters increase linearly, the feasible region grows exponentially. This is known as the curse of dimensionality. When an objective function is mapped to feasible parameter combinations, the resulting map is called a cost landscape (*see* Fig. 1A for a one-parameter landscape). Searches seek the lowest point – the global minimum – to minimize the cost [24,25]. Local search methods begin at an expert's “best guess” and proceed “downhill” to the nearest minimum (black

arrows, Fig. 1A). Because parameter values are uncertain, these methods usually lead to a local rather than the global minimum. To avoid such traps, randomized and incomplete global searches are used to sample the whole feasible region[39]. However, the curse of dimensionality means that smaller proportion of the space is covered. Parameter estimation scales poorly with model complexity. *As a result, parameters reported in the literature almost always represent local rather than global minima.* Multiple global searches are sometimes run to sample multiple local minima.

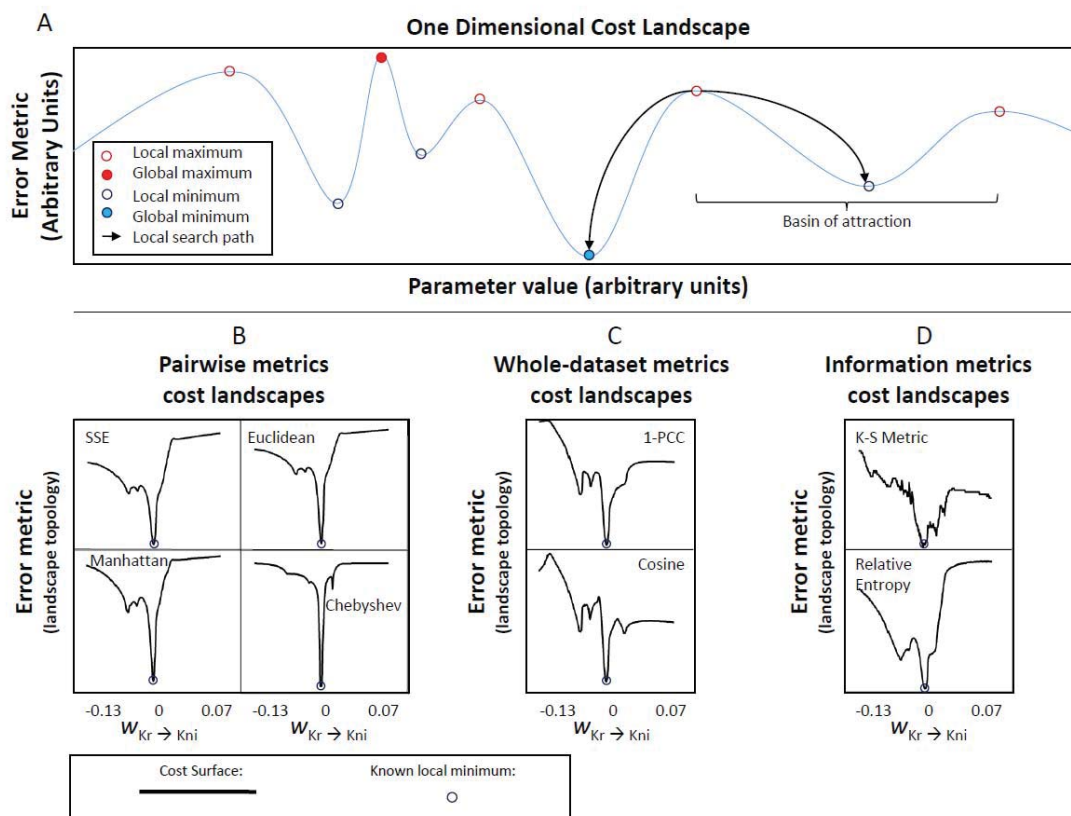


Figure 1. Objective choice affects the cost landscape and parameter estimation efficiency.

When objective functions are mapped to parameter values, a high-dimensional cost surface is revealed. (A) Plots a simple 1D surface. Maxima (red) and minima (blue) dot its surface; parameter estimation seeks the global minimum, or best fit, though this is not always possible. Each minimum has an associated basin of attraction; local search must start with the global minimum's basin to converge at the desired point. Because basins may be narrow and difficult to reach, global searches are used to survey the cost surface for low-cost points from which to launch local searches. In the full version of the *Drosophila* gap gene model, different objectives produce different landscapes (B-D), though all shared a similar minimal value near a predetermined local minimum (-0.034) of the $Kr \rightarrow Kni$ interaction parameter. Excepting Chebyshev, all of the pairwise measures (B) share qualitative trends. Whole dataset measures (C) also share a characteristic landscape. Information-theoretic measures (D) produced two qualitatively different landscapes when applied to this model.

When searches return optimized parameter sets, these sets are ranked by their objective values. Those with the lowest objective values are retained, though investigators often inject an element of subjectivity by ranking the lowest cost parameters “by eye.” This expert evaluation, coupled with the probabilistic nature of the search makes replicability of model analyses more difficult.

2.1. Bicoid gradient formation models

In *Drosophila melanogaster*, initial expression of gap genes takes positional cues from heterogeneously deposited maternal mRNAs and their resulting transcription factors [141]. The anterior determinant, Bicoid (Bcd), is expressed from anteriorly distributed mRNA and forms a decreasing concentration gradient from the anterior to posterior of the embryo [113]. Though Bcd has been studied since the 1980s [113,114,117,126,142-145], mathematical modeling of its gradient formation is a more recent enterprise [126,137,142,146,147]. These models represent the anterior-posterior (AP) axis of the embryo as a 1D spatial domain. In these early models, the anterior end of the line was a point source for Bcd production and expressed protein would diffuse toward the posterior. To avoid saturation of the AP axis by accumulating Bcd, Bcd degradation was modeled by a first order decay term [126,142]. Collectively, these source-diffusion-decay (SDD) models were numerically easy to calculate and contained parameters with explicit biophysical meanings (*e.g.*, diffusion constants). The models replicated the stationary Bcd gradient observed in data, though the time required to reach this state did not agree with comparable experimental time course observations. These discrepancies prompted further model development, demonstrating the utility of imperfect model

results. Ibanez and Belmonte provide an excellent review of these SDD modeling approaches [148].

Though Bcd is relatively simple to model, it is vital for the establishment of the gap gene patterning. The gap genes represent considerably more complex modeling approaches and are discussed in Section 2.2.

2.2.Gap gene patterning

Modeling has played a large role in the evaluation of the *Drosophila melanogaster* gap gene system. Driven in part by maternal mRNAs such as Bcd, this system of genetically interacting transcription factors forms increasingly specific expression bands along the fly embryo's anterior-posterior axis [141]. First experimentally characterized in the 1980s, decades of experimental work have gathered a wealth of data with which to fuel model-driven discovery [118,122,152-156]. Varied modeling approaches have been applied to this system over the last two decades, each presenting different challenges to model fitting. Early models (*e.g.*, Sanchez and Thierry [125]) incorporated pre-defined genetic regulatory networks (GRNs) inferred from expert interpretation of mutant data rather than using parameter estimation to infer GRNs. To compensate for contemporary computational limitations, these simulations frequently incorporated simplifying assumptions such as discrete protein levels, discrete spatial domains, and discrete time updates. The qualitative nature of the model output limited error calculations; protein data might be classified as high, low, or absent and compared to similar model output.

The work of Jaeger *et al.* [138,139] initiated quantitative modeling for the purpose of GRN inference via parameter estimation. This approach led to numerous analyses [140,157-163], but also brought new challenges to model fitting and parameter identification. Building on the partial differential equation simulation methods of Mjolsness and Reinitz [137], these models moved gap genes from discrete time and concentration simplifications to simulation of continuous concentrations and time on a 1D domain. Rather than building a model with *ad hoc* assumptions about the nature of GRN interactions, Jaeger *et al.* built a general model framework in which every gene had the potential to enhance or inhibit the expression of every other gap gene; they then fit the model to immunofluorescence expression data and observed which optimized GRNs minimized the unscaled sum of squared error between model and data. This approach generated a set of similar GRNs that recapitulated expression patterns and agreed with genetic interactions previously proposed from mutant data. While the computationally inferred GRNs are consistent with expectations, a major shortcoming remains: When gap genes were knocked out in simulations, the resulting protein distributions did not match available mutant data. This suggests that additional regulatory genes may be missing from the model, that the large number of parameters is causing overfitting, and provides further avenues for study.

All of the preceding models (except the early discrete variants) attempt to fit 25+ parameters; this high-dimensional parameter space *may* lead to two related problems: overfitting and non-unique solutions. In statistical models, overfitting refers to overly parameterized models which predict noise rather than underlying trends [36]. Similarly,

overfitting of dynamic models involves the distribution of error among many parameters during fitting; this may lead to spurious inferences from parameter estimation. While parameter estimation seeks the global optimal point – the best possible fit in the parameter space – high dimensional parameter spaces may contain many locally optimal parameter sets that produce equivalent fits (Fig. 1A). Indeed, when two parameters affect the same model output (*e.g.*, when two genes A and B enhance expression of a target gene C), the parameters regulating $A \rightarrow C$ and $B \rightarrow C$ are said to be correlated and unique parameter values will not be identifiable [39,166]. Because the approach of Jaeger *et al.* allows all gap proteins to interact (thus estimating 36+ interaction parameters), there is no guarantee of the uniqueness of estimated parameters and overfitting is likely. Fomekong-Nanfack *et al.* found that it was impossible to distinguish between enhancer and repressor activity in fitting results because of parameter correlation [157,160]. The sensitivity analysis of Bieler *et al.* also indicates correlation among model parameters, limiting the scope of model inference [165].

Finally, it must be noted that all of the preceding studies have utilized either qualitative fits (in the case of discrete models) or variants of the sum of squared error measure (*e.g.*, MSE, SSE, RMSE, and weighted SSE). The limitations of these measures in fitting relative spatial positioning data (such as adjacent gap genes) will be discussed in Section 3.

3. Objective functions

Objective functions compare model and data to produce lower residual scores for data-model agreement. In concrete terms, different objective functions compare different features of the model and experimental data. Two different metrics may produce conflicting rankings for the same sets of parameter values. As a result, the “terrain” of a cost landscape is determined by the choice of metric leading to different possible outcomes depending on the initial design choice. To demonstrate how each objective function responds to different types of model-data mismatches, data of the *Drosophila* gap gene *Knirps* (Figs. 2-4, brown diamonds) is compared against a set of artificially prepared erroneous distributions (Figs. 2A-4A, blue and red lines). To allow for ready production of the different types of mismatches, these distributions were generated from Gaussian distributions as a proxy for models described in Section 2.2. This enabled manipulation of spatial positioning (Figs. 2A-4A), width (Figs. 2B-4B), and aspects of magnitude (Figs. 2CD-4CD).

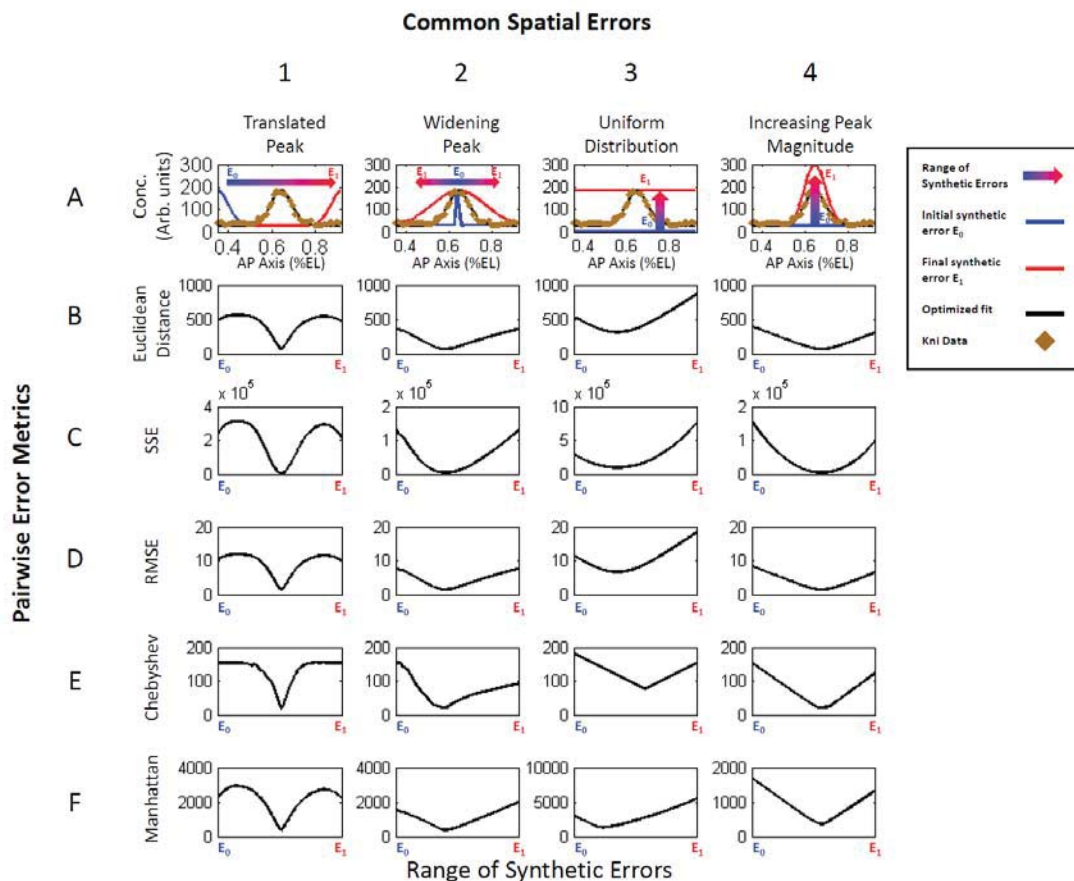


Figure 2. Response of pairwise objective functions to common spatial errors.

Each column represents a type of model-data mismatch; row A represents spatial distributions of the gap gene Knirps (Kni); rows B-F represent the responses of pairwise objective functions to each type of error. The Knirps (Kni) expression data in row A (brown diamonds) is from the lateral AP axis of embryonic *Drosophila melanogaster*. Relative to the data, the protein expression peak may be shifted anteriorly (A1, blue line) or posteriorly (A1, red line), it may narrow (A2, blue line) or widen (A2, red line), it may reach a uniform spatial distribution at varying concentrations (A3, blue line-red line), or it may decrease (A4, blue line) or increase (A4, red line) in concentration. Black lines in row A represent optimal model fits. Blue-to-red graded arrows in row A each represent a sweep across the range of erroneous models, with blue lines (E_0) at the beginning and red lines at the end (E_1) of each sweep. Rows B-F plot the response of each objective function as the sweep progresses.

3.1. Pairwise measures

The most commonly used cost functions are drawn from a class of pairwise measures.

These objectives are computed by comparing corresponding pairs of experimental and simulated data. The final objective is calculated using an aggregate of the individual pairwise residuals (or a subset of those residuals). Example equations for pairwise objectives are provided in Box 1.

Box 1: Pairwise Metrics

Sum of squared error (SSE)

The SSE is the summation of squared residuals between experimental and simulated data. For an equal number ($i = 1, 2, \dots, n$) of model and experimental data (y_i and \hat{y}_i , respectively), SSE is computed as

$$\sum_{i=1}^n (\hat{y}_i - y_i)^2$$

Euclidean Distance (l_2 -Norm)

The Euclidean distance is the square root of the SSE. For an equal number ($i = 1, 2, \dots, n$) of model and experimental data (y_i and \hat{y}_i , respectively), the Euclidean distance is computed as

$$\sqrt{SSE} = \sqrt{\sum_{i=1}^n (\hat{y}_i - y_i)^2}$$

Chebyshev Distance (l_∞ -Norm)

The Chebyshev distance is the maximum absolute residual. For an equal number ($i = 1, 2, \dots, n$) of model and experimental data (y_i and \hat{y}_i , respectively), the Chebyshev distance is computed as

$$\max_i (\hat{y}_i - y_i)$$

Weighting Approaches

The squared and absolute residuals in the preceding metrics may be weighted or normalized to reflect uncertainty in data and differences in data magnitude (e.g., where two proteins' concentrations orders of magnitude apart are being summed in the same function).

$$w_i |\hat{y}_i - y_i| \quad \text{or} \quad w_i (\hat{y}_i - y_i)^2 \quad \text{where } w_i \text{ may be}$$

$$w_i = \frac{1}{y_{\max} - y_{\min}}, \quad w_i = \frac{1}{\sigma_i}, \quad \text{or other functions.}$$

Root means squared error (RMSE)

The RMSE is the square root of the mean SSE. For an equal number ($i = 1, 2, \dots, n$) of model and experimental data (y_i and \hat{y}_i , respectively), RMSE is computed as

$$\sqrt{\frac{SSE}{n}} = \sqrt{\frac{\sum_{i=1}^n (\hat{y}_i - y_i)^2}{n}}$$

Manhattan Distance (l_1 -Norm)

The Manhattan distance is the summation of absolute error between residuals. For an equal number ($i = 1, 2, \dots, n$) of model and experimental data (y_i and \hat{y}_i , respectively), the Manhattan distance is computed as

$$\sum_{i=1}^n |\hat{y}_i - y_i|$$

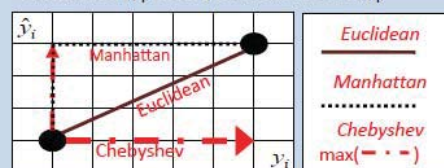
l_j -Norms

For an equal number ($i = 1, 2, \dots, n$) of model and experimental data (y_i and \hat{y}_i , respectively), the l_j -norm is computed as

$$\sqrt[j]{\sum_{i=1}^n |\hat{y}_i - y_i|^j}$$

Visual Comparison of Pairwise Measures

Simulated (\hat{y}_i) vs. Experimental Data (y_i)



Dotted and solid lines show the relative lengths of Manhattan and Euclidean distances between two points. The bold dash-dotted line indicates the Chebyshev distance

The sum of squared error (SSE), its square root the Euclidean distance, and its sample-normalized variant the root mean squared error (RMSE) are the most frequently used error measures in biological modeling studies. As its name implies, the SSE (also called ordinary least squares, OLS) is the summation of each squared pairwise residual.

Squaring the pairwise residuals serves two purposes. It prevents positive and negative residuals from partially canceling in the summation (thus underestimating the model-data mismatch). It also emphasizes larger residuals due to the super-linear growth of the square function. This intrinsic weighting translates to an error measure that is more tolerant of small residuals (*e.g.*, experimental noise at the optimal fit, Fig. 2B,1-4, data vs. optimal fit), while penalizing larger model-data disagreement with a weight proportional to the square of the mismatch (extrema of Fig. 2B,1-4). For global parameter searches that use gradient information from the cost landscape, this approach “smooths” the landscape (*cf.* Figs. 1B,SSE and 1D,K-S). In ideal situations, this smoothing may improve convergence toward minima, whether local or global. The data-averaged variant is the mean square error (MSE), calculated by dividing the SSE by the number of data points.

The square root of the SSE is the intuitive Euclidean distance metric (also known as the ℓ_2 norm and straight line distance). In everyday contexts, this is the familiar quadrature sum used to calculate the distance between points in space. Unlike the SSE, the Euclidean distance does not incorporate intrinsic residual-dependent weighting. This is exemplified in the one-parameter landscapes displayed in Fig. 1. SSE has lower relative costs corresponding to negative parameter values; the relative cost increases in Euclidean

distance (cf. Fig. 1B,SSE and 1B,Euclidean). Because the SSE is always nonnegative in practice, the cost landscape of the Euclidean distance will always share a global minimum with the SSE. However, the contours of the cost landscape will differ in that small errors are not smoothed from the landscape. This is shown in Fig. 1A,1,4 in which SSE ignores the low shoulders of the widened peak whereas Euclidean error takes them into account. Once global search algorithms have converged on the neighborhood of a minimum, the Euclidean metric provides a more stringent criterion by which local optimization homes in on the exact minimum value. A common normalization of the Euclidean distance is the root mean squared error (RMSE). The RMSE is computed by dividing the SSE by the number of data points before taking the square root. As demonstrated by Fig. 2A,C, this scalar normalization leads to identical landscapes for RMSE and Euclidean distance.

Though calculation time of the objective function is often negligible compared to the evaluation time of complex models, efficient objective calculations are sometimes called for. One such measure is the Manhattan distance (also known as the ℓ_1 norm, absolute distance, city block distance, and taxi cab distance), so named because it represents the distance traveled between two points on a regular grid such as New York's street system (see Box 1 for an illustrated example). As such, the Manhattan distance is always greater than or equal to the corresponding Euclidean distance. In practice, this objective is computed by summing the absolute values of each pairwise error. This serves the same purpose as squaring in the SSE; it prevents partial cancelation of positive and negative errors in the final distance value. The mean absolute error (MAE), the related per-datum

error, is computed by dividing the Manhattan distance by the number of data points. The Manhattan distance and MAE are not without drawbacks. They are not differentiable, making it impossible to analytically determine which direction on the cost landscape leads “downhill” to minima. These derivatives are used in some optimization algorithms. In practice, the derivatives of these error measures must be numerically estimated by evaluating the model multiple times. When using these algorithms, this numerical estimation may negate the increased efficiency derived by use of the Manhattan distance. The Manhattan distance has landscape behavior qualitatively similar to that of Euclidean and RMSE; this is demonstrated in Figs. 1B and 2F,1-4.

In practice, any ℓ_j norm may be computed for real numbers by summing the absolute residuals raised to the j th power and then taking the j th root of the result (see Box 1). As indicated in discussion of the SSE and Euclidean distances, larger values of j place larger intrinsic weights on larger residuals. The logical conclusion of this trend is the ℓ_∞ norm, or Chebyshev distance. This objective places all the weight on the largest residual and no weight on lesser residuals. The Chebyshev distance is computed by calculating the absolute residuals and then returning the largest residual. The objective shares the Manhattan distance’s drawback of non-differentiability. Determining the maximum residual is also computationally expensive for large datasets. The resulting cost landscape is often extremely flat, making optimization difficult. However, the Chebyshev distance is useful for mini-max optimization strategies. This entails minimization of the maximum residual between simulation and data, effectively finding the “best” worst-case parameter set and is reflected in a landscape that differs

qualitatively from other pairwise measures (Figs. 1B, extrema of 2E,1, overall shape of 2E,2-4).

In each of the preceding error measures, weighted and/or normalized variants are also in use. These are described in Section 3.5.

3.2. Whole-dataset measures

Pairwise error measures incorporate transformations and summations of residuals to report a scalar error value. In contrast, whole-dataset measures are computed using properties of the entire experimental and simulated data sets such as arithmetic mean and variance. These measures are most commonly encountered in statistical contexts (*e.g.*, the Pearson correlation coefficient) and machine learning and bioinformatics applications (the cosine similarity), but are rarely seen in dynamic model fitting. Implemented in isolation, these methods have limitations that restrict their use. These measures sometimes produce qualitatively similar landscapes (Fig. 1C), indicating that they share some of the same limitations.

The Pearson correlation coefficient (PCC) is often associated with linear regression. It is computed as the covariance of model and experimental data divided by the product of their standard deviations (see Box 2). This objective quantifies the variability of paired (experimental, model) data points relative to the least squares linear regression of the data; a value of one represents perfect correlation while negative one indicates perfect inverse correlation. As such, a large positive value of this metric *might* indicate a linear

relationship between the experiment and model (Fig. 3C,4) while the slope of the regression line provides a measure of linear scaling between the two sets. The chief limitation of this objective is its dependence on a linear relationship between simulated and experimental data. The variability measured by this objective may represent normally distributed residuals about the regression line. However, nonlinear errors may still produce relatively large correlation coefficients (Fig. 3C,2). Anscombe presented four examples that illustrate the measure's insensitivity to nonlinearities[227]; his results are reproduced in Box 2. Due to this limitation, correlation measures provide additional information about variability when used in conjunction with other measures. Used in isolation, PCC may lead to unrealistic parameter estimation.

Box 2: Whole Dataset Metrics

Pearson Correlation Coefficient (PCC)

The Pearson correlation uses the mean and variance of the model (\hat{y}) and experimental (y) data (with n data) to calculate the variability of model-experimental points predictions relative to a regression line fit to the data.

$$\frac{\text{cov}(y, \hat{y})}{\sigma_y \sigma_{\hat{y}}} = \frac{\sum_{i=1}^n (y_i - E[y])(\hat{y}_i - E[\hat{y}])}{\sum_{i=1}^n (y_i - E[y])^2 (\hat{y}_i - E[\hat{y}])^2}$$

The PCC increases with improved fit, but error metrics must decrease. To rescale the and invert the PCC, it is normalized as follows.

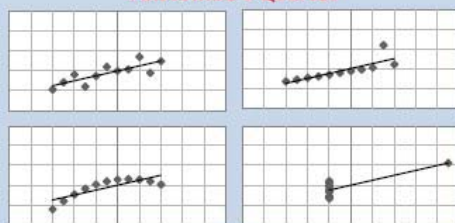
$$1 - \left(\frac{\text{PCC} + 1}{2} \right)$$

This distance measure is zero for perfect correlation and one for anti-correlation.

The Anscombe Quartet

The limitation of assuming linearity was demonstrated by Anscombe in 1973. He reported four distributions that returned respectable PCCs of 0.816 despite nonlinearity. This occurrence translates into false positives when optimizing parameters.

Anscombe's Quartet



PCC = 0.816;

$y = 3.00 + 0.500x$

Cosine (Angular) Distance Metric

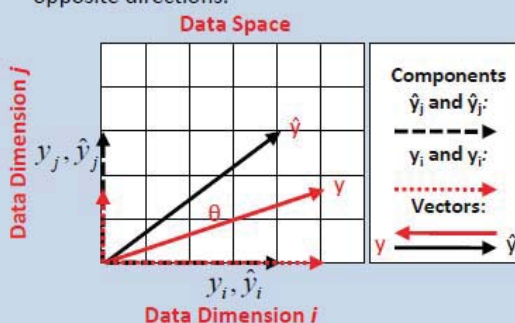
The cosine (or angular) similarity is computed by considering a data space n dimensions corresponding to n data. Model and experimental data are each represented by a vector in this space; the magnitude of the n th datum is the component of the vector in the n th data dimension. Cosine similarity computes the cosine of the angle θ between the two vectors as the crossproduct divided by the vectors' norms:

$$\cos(\theta) = \frac{y \cdot \hat{y}}{\|y\| \|\hat{y}\|} = \frac{\sum_{i=1}^n y_i \times \hat{y}_i}{\sqrt{\sum_{i=1}^n y_i^2} \times \sqrt{\sum_{i=1}^n \hat{y}_i^2}}$$

As with correlation, cosine similarities of one represent perfect agreement while values of negative one indicate vectors pointed 180° apart. Like the PCC, it is normalized to a range of zero to one and subtracted from one to provide a cost metric:

$$1 - \left(\frac{2 \cos^{-1}[\cos(\theta)]}{\pi} \right)$$

This measure is zero for vectors pointing in the same direction and one for vectors pointed in opposite directions.



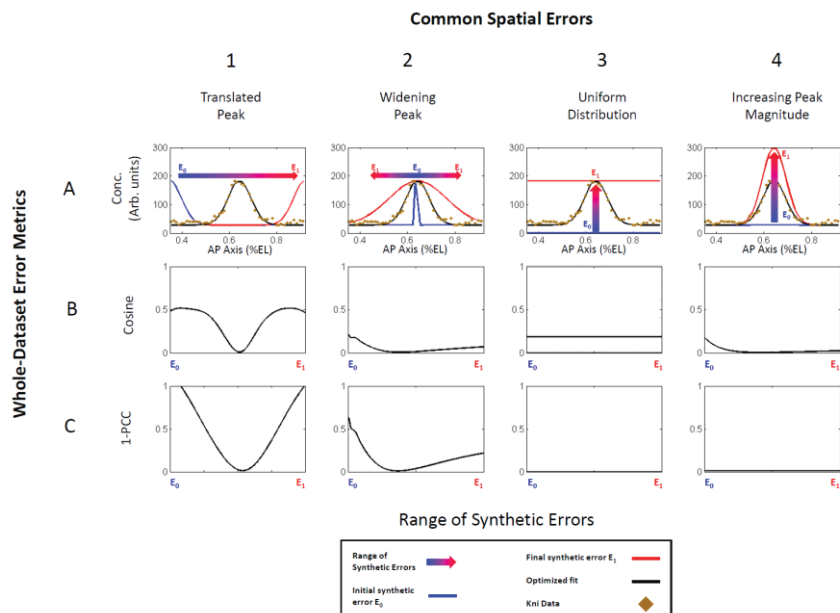


Figure 3. Response of whole-dataset objective functions to common spatial errors. Each column represents a type of model-data mismatch; row A represents spatial distributions of the gap gene Knirps (Kni); rows B-C represent the responses of whole-dataset objective functions to each type of error. The Knirps (Kni) expression data in row A (brown diamonds) is from the lateral AP axis of embryos. Relative to the data, the protein expression peak may be shifted anteriorly (A1, blue line) or posteriorly (A1, red line), it may narrow (A2, blue line) or widen (A2, red line), it may reach a uniform spatial distribution at varying concentrations (A3, blue line-red line), or it may decrease (A4, blue line) or increase (A4, red line) in concentration. Black lines in row A represent optimal model fits. Blue-to-red graded arrows in row A each represent a sweep across the range of erroneous models, with blue lines (E_0) at the beginning and red lines (E_1) at the end (E_1) of each sweep. Rows B-C plot the response of each objective function as the sweep progresses.

The cosine (or angular) distance and its relative the cosine similarity provide another means of comparing two datasets. It is often used in machine learning and clustering algorithms as a means of measuring distances between vectors of features used for classification; it is not often used to fit biological dynamic models. Rather than pairwise comparisons in two dimensions (model and experimental data), this objective considers each of the n paired data to represent a dimension in an n -dimensional data space. The model and experimental data are represented by two respective vectors in this space and the angle between these vectors is computed. The cosine of this angle will be one if the vectors point in the same direction and negative one if they point in the opposite direction, though this cosine similarity disregards scaling. It thus compares the overall shape of spatial morphogen distributions while lessening penalties for differences in total concentrations (Fig. 3B,2-4). Because cost functions represent poor fits with larger objective values, cosine similarity is often normalized from $(-1,1)$ to $(0,1)$ and then subtracted from one (see Box 2). This produces a measure that is one when the data vectors point in opposite directions of the data space and zero when the vector point in the same direction. The main shortcoming of this measure is its blindness to the relative magnitudes of model and experimental data. If a parameter set leads to a simulated dataset in which all morphogen concentrations are near zero, computational rounding errors and limited machine precision create varied objective results, which may be erroneously low – representing a good fit where none exists.

3.3. Information-theoretic measures

While the whole-dataset objectives are used to compare data vectors (albeit not always in the context of biology), this next class of information-theoretic objectives is used for comparison of probability density functions (PDFs). Here, we treat morphogen distributions as analogous to PDFs over an organism's spatial domain. In typical use, experimental or simulated sampling provides data to estimate the PDF(s) of interest. When the information measures are used as objective functions for model and experimental data, the intermediate sampling step and PDF estimation are not necessary. In place of sampling, the model and experimental data are treated as morphogen concentration density functions over the spatial domain of the. With these PDF analogues in hand, the information measures may be brought to bear, though the PDF analogues do not always meet conditions for a robust information-theoretic interpretation.

A common measure for PDF comparison is the Kolmogorov-Smirnov D-statistic (K-S statistic). The procedure for calculating the K-S statistic is similar to that of the Chebyshev distance (Section 3.1). Though the Chebyshev distance corresponds to the maximum absolute residual of the model and experimental data, the K-S first transforms the data- and model-sets y and \hat{y} to the cumulative density functions (CDFs) F_y and $F_{\hat{y}}$ (Box 3). The K-S statistic is the maximum absolute residual between these CDFs. Unlike the Chebyshev distance, K-S incorporates an implicit linear scaling. Regardless of relative magnitudes of the model and experimental data, transformation to CDFs bounds the functions from zero at one end of the spatial domain to one at the other. Like cosine distance (Section 3.2), the scaling emphasizes the overall shape of the data while relaxing

the requirement that concentration values match exactly. This statistic still has limitations. As indicated in Figs. 2E, 3B and 4B, Chebyshev and cosine distances penalize common errors differently. The intrinsic scaling in the K-S objective *function should* penalizes mismatches in absolute concentration less harshly, though the estimation of CDFs F_y and $F_{\hat{y}}$ is very sensitive to experimental noise. Figure 4B,1-2 demonstrates the effect of noisy data: the minimal K-S values do not even align with the best-fit distribution. Objectives like cosine emphasize the overall shape of the model and experimental distributions. Meanwhile, mini-max strategies like Chebyshev reduce the largest error – sometimes at the expense of an overall consistent fit.

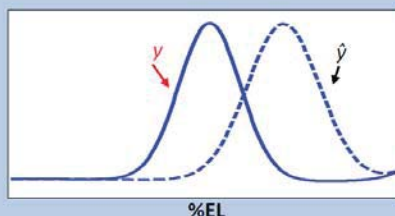
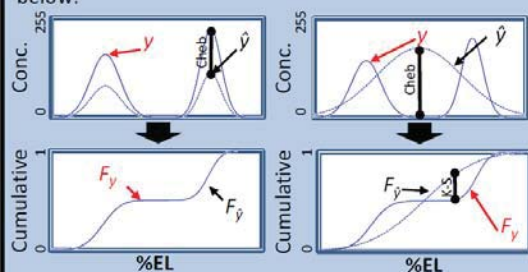
Box 3: Information Metrics

Kolmogorov-Smirnov Metric

The Kolmogorov-Smirnov (K-S) metric applies a mini-max optimization strategy similar to the Chebyshev distance. Rather than determining the maximum residual error of the data distributions (y , \hat{y}), the cumulative distribution functions (F_y , $F_{\hat{y}}$) are computed first. Then the Chebyshev distance is computed for these CDFs. For $i = 1, 2, \dots, n$ data, the absolute residuals of F_{y_i} and $F_{\hat{y}_i}$ are computed. The maximum residual is returned:

$$\max_i (|F_{\hat{y}_i} - F_{y_i}|)$$

A K-S value of zero indicates perfect agreement; the calculation ignores scaling like the cosine distance. A value of one indicates a large difference in distributions. Despite the similarity of the procedures, Chebyshev distance and K-S penalize functions differently. This is illustrated below.



Relative Entropy (RE; Kullback–Leibler divergence)

The relative entropy is used to compare the information content of two empirical distributions. Here, we take the model and experimental data to be probability distributions of protein concentration on the spatial domain. Under this assumption, relative entropy measures the information loss experienced if an incorrect modeled distribution is substituted for the true experimental distribution. It is calculated as

$$D_{RE}(y || \hat{y}) = \sum_{i=1}^n \ln\left(\frac{y_i}{\hat{y}_i}\right) y_i,$$

where n is the number of data points, y_i is the i th experimental point, and \hat{y}_i is the i th model point. Before computing the error, both distributions are normalized such that the area under the curve is one (i.e., probability density functions).

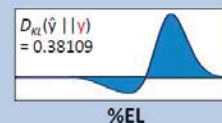
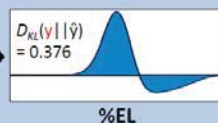
An important characteristic of the RE is the asymmetric nature of the measure. This may be explained by expanding the formula:

$$\sum_{i=1}^n \ln(y_i) y_i - \ln(\hat{y}_i) y_i$$

The information lost substituting model \hat{y}_i for data y_i is not identical to the opposite substitution:

$$\sum_{i=1}^n \ln(\hat{y}_i) \hat{y}_i - \ln(y_i) \hat{y}_i$$

This is illustrated in the figures at left and below. The integral (shaded area) is the relative entropy.



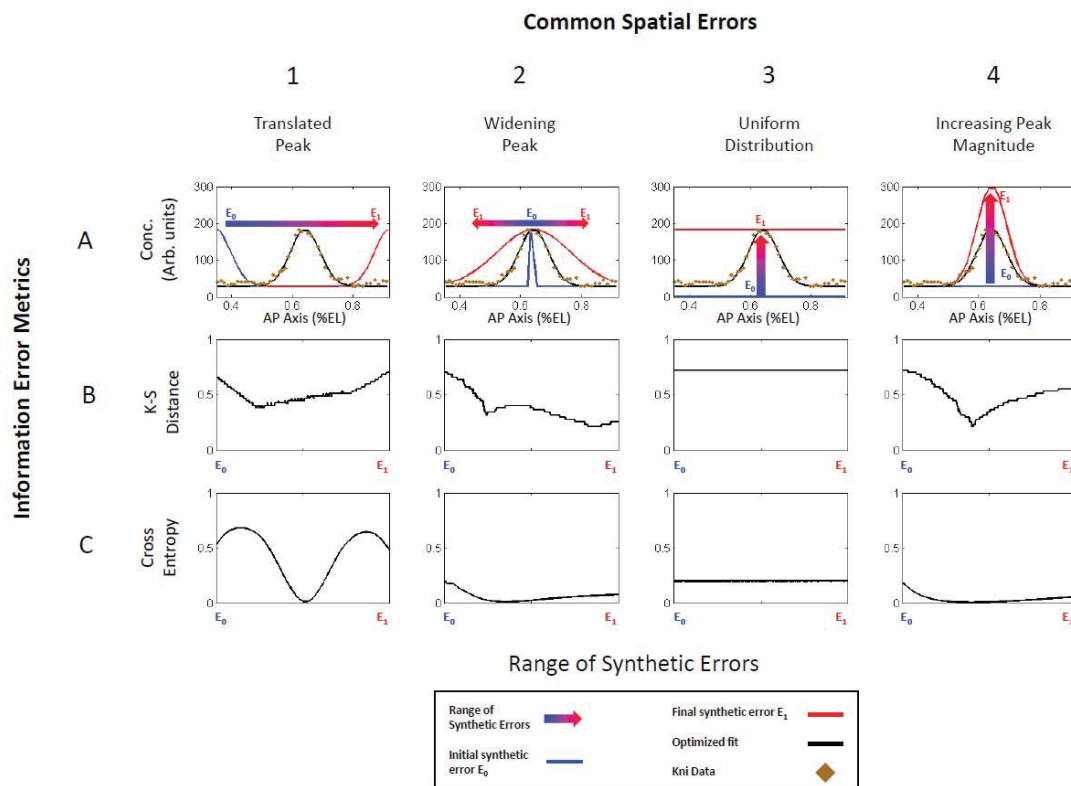


Figure 4. Response of information-theoretic objective functions to common spatial errors.

Each column represents a type of model-data mismatch; row A represents spatial distributions of the gap gene *Knirps* (*Kni*); rows B-C represent the responses of information objective functions to each type of error. The *Knirps* (*Kni*) expression data in row A (brown diamonds) is from the lateral AP axis of embryos. Relative to the data, the protein expression peak may be shifted anteriorly (A1, blue line) or posteriorly (A1, red line), it may narrow (A2, blue line) or widen (A2, red line), it may reach a uniform spatial distribution at varying concentrations (A3, blue line-red line), or it may decrease (A4, blue line) or increase (A4, red line) in concentration. Black lines in row A represent optimal model fits. Blue-to-red graded arrows in row A each represent a sweep across the range of erroneous models, with blue lines (E_0) at the beginning and red lines at the end (E_1) of each sweep. Rows B-C plot the response of each objective function as the sweep progresses.

Every distance measure discussed so far has been symmetric – the distance from y to \hat{y} is identical to the distance from \hat{y} to y . However, the relative entropy (also known as the Kullback–Leibler divergence) is asymmetric; these two distances are unequal. In the context of information theory, entropy is a measure of information. The relative entropy may be considered the amount of information lost if the model data \hat{y} is used to approximate the true experimental distribution y [228]. To compute the relative entropy, the two data sets are each normalized so that the data in each distribution sum to one (satisfying the criteria for a discrete probability distribution). Rather than using residuals, each comparison between experimental and model datum i ($i = 1, \dots, n$) is performed by multiplying y_i by the logarithmic ratio of y_i over \hat{y}_i . The summation of these values yields the relative entropy. A visualization of this measure is found in Box 3.

This method is not without limitations; it is only defined if both \hat{y} and y each sum to one (hence the normalization) and if y_i equals zero for any i where \hat{y}_i equals zero. This limits parameter estimation: If the model dataset predicts no morphogen at a point in space that has nonzero experimental data, the relative entropy will be undefined due to division-by-zero in the log ratio. This means that some parameter sets (which cannot be identified in advance) will not have an associated error value. If y_i and \hat{y}_i equal zero, the comparison becomes $0 \ln(0/0)$. If y_i is zero and \hat{y}_i is not, $0 \ln(0)$ appear in the calculation. These two values are normally considered to be undefined. For the purpose of relative entropy calculation, both are considered to be zero; in each case, the limit of $x \ln(x)$ and $x \ln(x/x)$ is zero as x goes to zero.

3.4. Composite cost functions

Pairwise, whole-dataset, and information-theoretic error measures all have strengths and weaknesses. It is common for computational biologists to assemble *ad hoc* combinations of objectives into a single composite cost function. These functions are tailored to emphasize the data features pertinent to the current research or to combine models and/or experiments. For example, we may wish to combine the qualitative shape matching of cosine distance with the residual-dependent weighting of SSE. The resulting composite function may appear as follows.

$$\text{Composite Cost} = w_1 \text{Cosine Error} + w_2 \text{SSE} \quad (1)$$

For a given parameter set, *Cosine Error* and *SSE* represent the two objective functions. Each is weighted by positive constant values w_1 and w_2 . These weights serve multiple purposes. Consider that the cosine distance ranges from zero to one while SSE values are dependent on the magnitude of the data. If weights are not applied within the composite function, the either objective may dominate the composite value. Depending on the magnitude of the data, one must choose a ratio of w_1 to w_2 to give each component objective comparable contributions to the final error.

Conversely, weights may be chosen to emphasize one component objective over another. Perhaps the foremost interest is in finding a qualitative shape match between experimental and simulated morphogen distributions. At the same time, we wish to avoid the inaccurately low error due to the cosine distance's blindness to magnitude differences. We

may choose weights w_1 and w_2 such that the cosine distance contributes more to the composite cost than SSE. The exact ratio is difficult to identify in advance of parameter estimation. Often, we generate a set of synthetic experimental data (model data generated by a known parameter set), and weight ratios are tested to determine which ratio recovers the known parameter set most efficiently.

3.5. The importance of transformation and normalization

A common transformation of data is unit conversion. For example, immunofluorescent intensities are assumed to correlate with the concentration of the antibody targets. When a model simulates concentration and experimental data is recorded in intensity, we might perform a linear transformation ($c = ax - b$) on data. Here, c is the estimated concentration, a is a linear scaling factor, x is the intensity data, and b accounts for background fluorescence in the micrograph. This simple example assumes uniform background intensity. This assumption is not always satisfied in practice due to varied experimental limitations. Though we limit our discussion to linear transformations, the transformation is assay-dependent and may involve more complex functions.

Experimental data does not always require linear or nonlinear transformation. Some computational biologists design their models and parameter ranges such that the simulated morphogen values are directly comparable to data. This approach precludes the need for mapping experimental units to simulated units; instead, subtraction of a uniform or nonuniform background value is the only modification to experimental data.

Error values may also be transformed. Some cost landscapes are very “rough,” leading to narrow basins of attraction separated by high “peaks” Figs. 1B-D. Some optimization techniques are more tolerant of “smoother” cost landscapes [229], and transformations may be used to reduce the magnitudes of the peaks in the landscape. Often, a logarithmic transform is applied to the objective function values; it acts to compress error values, which may be orders of magnitude apart before transformation, to the same magnitude.

The weighted SSE (wSSE) scheme calls for division of each residual by the replicate standard deviation of its experimental data point. Formulaically, the i th squared residual has a weight $w_i = 1/\sigma_i$. Here, σ_i is the standard deviation of experimental datum y_i . When the replicate values for a given experimental datum are highly variable, the residual is divided by a large standard deviation and the contribution of the uncertain data to the error is minimized. Other *ad hoc* weighting schemes may be used depending on our needs. Normalization methods are also employed in problem-specific contexts. For example, fractional or normalized RMSE (nRMSE) divides the RMSE by the range of predicted values; $w = \hat{y}_{max} - \hat{y}_{min}$. The resulting weighted residuals may be interpreted as a fractional or percentage errors in each simulated datum.

A special case of weighting addresses the comparison of model and experimental data spanning several types of chemical species. Intercellular morphogens and intracellular signaling molecules may have respective molarities differing by several orders of magnitude. In cases of pairwise measures without implicit linear scaling, this may lead to unequal contributions from each chemical species to the final cost value. For example,

errors in a morphogen profile spanning a 100 nM range could completely mask fluctuating error contributions from a protein distribution with a 10 nM range. Similarly, comparison of untransformed immunofluorescence or histochemical data with compatible models may be hindered by differences in antibody affinity among measured species. Different chemical species' errors may contribute unequally to the error value. One solution to this problem has been noted above. The nRMSE uses fractional residuals. Each residual is weighted by the range of the simulated chemical species. For morphogen $M1$, each residual is multiplied by a weight $w_{M1} = \hat{y}_{M1,max} - \hat{y}_{M1,min}$. Likewise, all residuals for morphogen $M2$ are weighted $w_{M2} = \hat{y}_{M2,max} - \hat{y}_{M2,min}$, and so on for each additional chemical species. Substituting fractional residuals in place of residuals, thus ensuring that they contribute equally to the overall error.

When sampling a large parameter space, it can be difficult even to find qualitatively useful features like peaks, let alone peaks that align with experimental data. Though some objectives tolerate spatial changes better than others, all surveyed objectives save the Kolmogorov-Smirnoff statistic have similar responses to spatially shifted peaks (Figs. 2C-F, 3B-C, and 4B-C). Dynamic space warping (DSW) provides a means of protecting qualitative agreement from positional mismatch. DSW is a nonlinear distortion of model values rather than a linear transform. It is an alignment algorithm that warps the spatial coordinates of two signals (such as immunofluorescence intensities) to minimize mismatch between the signals; this allows slightly offset peaks to be aligned before the objective is calculated and reduces penalties when evaluating distribution shapes. To demonstrate how the procedure, consider data and slightly offset model output (Fig 5A). DSW traverses the

length of the domain and calculates the residual of each model-datum pair in spatial order (an unwarped path would be the diagonal of Fig. 5B). It iteratively calculates the residuals of the residuals at spatially adjacent points and then moves to the smallest residual value (Fig. 5C). This results in an alignment (white line in Fig. 5B) that minimizes errors of position (but not errors of magnitude) between model and data (Fig. 5D). To prevent drastic warping, the method is often constrained to a fraction of the total domain length. A concise introduction is Müller's "Information Retrieval for Sound and Music"[230], which describes the mathematically analogous technique of dynamic space warping.

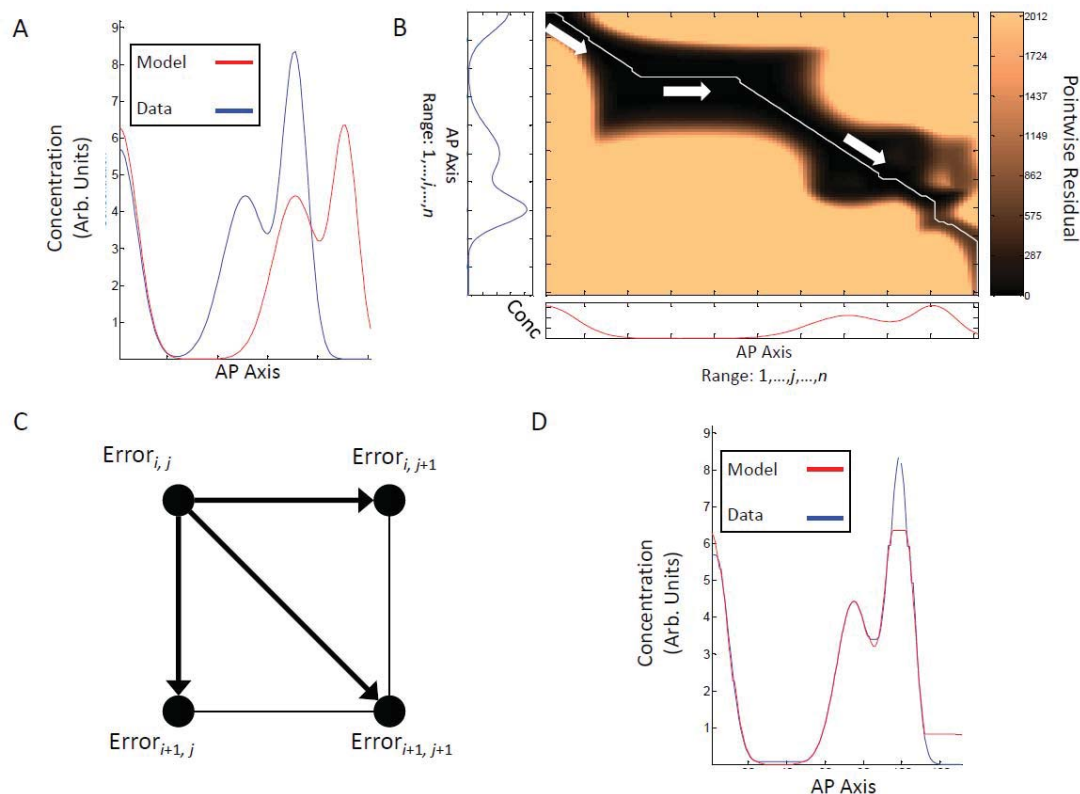


Figure 5. Schematic explanation of dynamic space warping.

Dynamic space warping is a spatial alignment of two signals to minimize the disagreement between them. Consider a dataset (A, blue line) and model simulation that is partially misaligned (A, red line). A pointwise array of the two signals' data (B) is formed and traversed from beginning to end of each sequence (B, white arrows and line). At the i th, j th position on the grid, the residual values are computed for the next model-datum pair at $i+1, j+1$, but the model is also compared to spatially adjacent data points $i+1, j$ and $i, j+1$. The traversal iterates by choosing the lowest of the three residual errors at each step (C). The mismatch between each model-datum pair is shown in B, with darker regions representing lower errors. The result is a warping that minimizes spatial translation and peak width errors.

Finally, a more flexible solution to the above problem is to employ a composite cost function. Rather than incorporating different measures of the same data, we may partition the data and compute the same objective function for each species. The weight ratios noted in Eqn.1 may simply equalize the contributions (equivalent to the nRMSE approach) or may be further modified to preferentially penalize some species if the research question calls for it.

4. Strategies for improved parameter estimation

Today, many modeling studies rely on “off-the-shelf” objective functions such as SSE. These objectives are not always appropriate for the biological question being addressed. Here, we provide a brief schema to screen objectives before committing computational resources and time to a large-scale search of the parameter space.

4.1. Identify appropriate error measures

The selection of appropriate error measures depends upon the type of data available (here assumed to be semi-quantitative), whether unit rescaling or normalization matters for the research problem, and the type of fit required (exact fit, shape matching, relative positioning, etc.).

The assumption of semi-quantitative data provides two important considerations. The data do not contain absolute concentrations of the values of interest, but rather recordings of some observable signal (immunofluorescent image intensity). Further, this implies that model outputs, if designed to accurately represent the underlying units of interest, may

differ in units and by orders of magnitude relative to experimental observables. In some cases, this will necessitate transformation/scaling to bring the two datasets' units into agreement.

In the *Drosophila* gap gene case study above, the model parameters were scaled such that model output was bounded between 0 and 255 arbitrary concentration units. This was decided so that model output could be compared directly to experimental image intensity data; in 8-bit digital imaging, each pixel's unitless intensity ranges from 0 to 255. This type of model does not require transformation of data because the model was designed to avoid issues of unit and magnitude mismatch. This is not always straightforward in model design. The construction of large models often involves surveying the literature of chemical rate constants – typically incorporating units of molarity – resulting in molar outputs. As noted in Section 3.5, a linear transformation is used to convert intensity to molarity. In the absence of calibration standards, the choice of linear transformation parameters must be optimized before each comparison of model and experimental data. An alternative method renders both datasets unitless by dividing each set by its maximum value; this also scales the data range from zero to one. Finally, this pre-processing step may be avoided by use of implicitly-scaled error measures such as cosine distance or the information measures. In addition, if the relative spatial positions of biochemical species are an important criterion for optimization, data pre-preprocessing via dynamic time warping may serve to align spatially offset data before objectives are applied. A schema for objective function selection is shown in Table 1. Note the many more objective

functions exist than are listed here; the Encyclopedia of Distance Measures provides brief descriptions of a greater number than can be discussed here [231].

Table 1. Criteria for selecting appropriate objective functions

Cost function criteria		
Error selection criteria	Objective function(s)	Scaling or normalization
Exact fit of concentrations	SSE, MSE, Euclidean , RMSE, Manhattan, MAE, ℓ_j norm	Transformation to bring units and magnitudes into agreement
Emphasis on spatial coordinates and “shape” of distributions	Cosine distance, relative entropy	Rescaling is implicit in these functions; Dynamic space warping may be required
Relative spatial positioning with exact concentrations	SSE, MSE, Euclidean , RMSE, Manhattan, MAE, ℓ_j norm with DSW	Transformation to bring units and magnitudes into agreement; DSW to align spatial offsets
Relative spatial positioning with emphasis on “shape”	Relative entropy, pairwise or whole-dataset method with DSW	Rescaling is implicit in these functions; DSW to align spatial offsets
Mini-max strategy for concentration fitting	Chebyshev	Transformation to bring units and magnitudes into agreement
Abbreviations: DSW, Dynamic space warping; MAE, Mean average error; MSE, Mean square error; RMSE, Root mean squared error; SSE, Sum of squared error		

4.2. Perform a basic global sensitivity analysis

To choose a well-behaved measure for the objective function, we first carry out a sensitivity analysis. Sensitivity analyses (SA) systematically perturb parameters to characterize a model's response to changes in parameter values. If the modeled behavior of a morphogen changes drastically in response to perturbation of its diffusion constant D , the morphogen is said to be sensitive to changes in D [232]. Rather than determining the sensitivities of biochemical species to parameter perturbations, we suggest a simple SA to determine the sensitivity of cost functions to parameters.

Global sensitivity analyses reveal trends in objective values over the entire parameter search space (*e.g.*, parameter regions where objective values are lower), but more informative analyses require additional model simulations. To save time, we recommend using an extremely simple global sensitivity approach: Randomly sample the parameter space and visually compare changing objective values versus each parameter. This will reveal direct effects of parameters on objectives, but not parameter interactions.

We recommend the Latin Hypercube Sampling (LHS) algorithm for fast sample selection. It is quasi-random and guarantees more uniform sampling of the parameter space than uniform random sampling [232]. The number of points in the sample will vary depending on the computational cost of the model and the size of the space. This method serves a preliminary screen before time-intensive parameter estimation, so we err on the side of efficiency rather than completeness: We use a heuristic of at least $1000d$ sampled parameter sets, where d is the number of parameters. (For the 1D *Drosophila* gap gene model, 42,000

evaluations take approximately six hours.) When the model in question is particularly fast, we may choose to increase the number. For models that require hundreds of seconds to evaluate, we may omit this step.

After sample parameter sets are selected and the model is evaluated, we compute all the objective functions chosen in Section 4.1 at each sample point. This creates a list of objective values that corresponds to each parameter set. With this information, we plot the each objective value against each model parameter. Because objective values are only plotted against one parameter at a time, the variability of other parameters adds noise to the plot; visible trends in these plots indicate global trends in objective sensitivity.

Regions of distinct high and low objective values are indicative of promising search areas (low cost regions) within the parameter space. These objective functions should be retained. Conversely, some objectives may produce only uncorrelated scatterplots; while minima exist in the corresponding cost landscapes, the surface is likely “flat” and “rough.” This may present difficulties during optimization[233].

4.3. Choose an objective or objectives

Using the above information, we may make an informed choice of objective functions rather than defaulting to SSE or RMSE. If visual analysis yields cost functions with global trends these are recommended for use in parameter optimization.

Scatterplots without any global trends do not indicate that the selected cost functions are inappropriate for parameter estimation. The sampling performed by random or LHS sampling is incredibly sparse when compared to the full-factorial sample. There may not be enough coverage to identify global trends. While it is not necessary to exclude objective functions without global trends, we consider removing them from subsequent steps unless (a) all objectives are uncorrelated or (b) objectives showing global trends fail in subsequent steps. Here we may choose to retain at least one stringent cost (*i.e.*, a magnitude matching function) and an error tolerant (shape matching) function.

4.4. Parameter optimization by sequential optimization

With objectives in hand, it is now possible to search for optimal parameter estimates. This step costs the most in terms of computation terms and we have undertaken the previous steps to identify maximally effective objective functions used in this step. We recommend a three-step process: It begins with another stochastic sampling to screen for promising parameter sets. Then these initial sampled points are used with a stochastic global search method (*e.g.*, genetic algorithms (GAs) or simulated annealing (SA))[234]. Finally, the best point(s) are locally optimized.

For the first task, choose the least stringent objective function you have retained from previous steps. The purpose of this global screen is to generate candidate parameter sets for further refinement. To do so, repeat the stochastic sampling discussed in Section 4.2. The number of points required is dependent on the global search algorithm you choose. The choice of a lenient objective ensures that promising minima and basins of attraction

are not discarded prematurely. Dynamic space warping (DSW), normally used in face- and handwriting-recognition may also be used if appropriate to the research goals[235]. From the results of the screen, identify the lowest-error point(s) as required for your chosen global search algorithm (such as the initial population of a GA or the starting point of SA).

The second task is the time-intensive parameter estimation step that would typically begin with a pre-chosen objective such as SSE or RMSE. Here, the promising parameter dataset(s) from the previous screen are used to initialize the stochastic search of the parameter space. Depending on available resources, this may be run once or multiple times to generate one or more optimal parameter sets for analysis.

For the third task, screen the resulting point(s) with a follow-up local search. The stopping criteria of global optimization methods generally stop the search short of the minimum of a basin. The purpose of the subsequent local search is to obtain the nearest minimum in the region of the solution found by the global search. We recommend switching to a more stringent objective for this task. The retained parameter sets should already be in the basins of the minima we wish to reach, so the risk of entrapment in another local minimum is lessened. The more stringent objective will enforce a closer fit between model and data.

5. Conclusions

Models that have been rigorously constrained to the available data can be used in a number of ways that complement the existing tools for experimental discovery.

Two- primary motivations for using modeling as part of the repertoire of experimental methods are to test new hypotheses with the model or to use the data obtained to reverse engineer the networks and/or parameters of signal regulation. For instance, while many mechanisms are testable *in principle* and may serve as inspiration for further experimentation, technical limitations such as the lack of appropriate antibodies, lack of equipment, and reagent costs sometimes make testing impractical. Using parameter estimation, mechanistic models may act as surrogate systems for interrogation when direct experiments are impractical. These surrogates might indicate an informative subset of possible experiments on which to expend limited resources.

Whereas hypothesis testing typically proceeds from identification of falsification criteria to experiment, dynamic models permit alternative approaches. When multiple explanations for observed behavior are under consideration and it is impractical to measure key concentration or kinetic values, each mechanism may be encoded in a separate model structure. So long as models simulate overlapping observable concentrations and kinetics, they may be fit to previously collected data. The hypotheses (models) are then ranked according to agreement with data [236]. Because these models each describe a single hypothesis, this surrogate approach is most useful for testing the sufficiency of proposed model mechanism(s) to explain observations. However, its scope is limited compared to direct experimentation. Simulated results may be used to rule out insufficient mechanisms but are only valid assuming the model is true. Experiments provide new data about the system even if they lead to falsification of prevailing hypotheses.

After models are ranked according to their ability to recapitulate existing data, analysis can proceed in two directions. If none of the hypotheses produce agreement with data, further hypothesis generation is called for. If one or more models are consistent with available data, the results can suggest additional experimental falsification criteria to discriminate between consistent models. For example, the competing viable models may predict distinguishable dynamics for observable but unmeasured molecular species. In this case, models drive experimental design by identifying the experiments that will have the greatest discriminatory power to resolve differences in the data-consistent networks, a process known in engineering as Model-Based Optimal Design of Experiments (MB-ODE) [35,237].

When parameter estimation is used to fit multiple models to data, it allows us to judge the sufficiency of competing mechanisms to explain observations. When investigators are confident in a particular mechanism, parameter estimation provides a framework to make holistic inferences about the underlying biology. The last decade has evidenced increasing enthusiasm for systems biology with over 15000 instances present in the NCBI PubMed database (8500 published since 2010)[238]. Despite the promise of whole-system analysis, the cost of comprehensive data collection and bottlenecks in data analysis present challenges to its implementation. Here again, models may serve as surrogates for costly batteries of high-throughput perturbation experiments.

Once estimated parameter values are selected that approximate observed data, sensitivity analyses are used to test the fragility and robustness of the system to parameter changes

and state perturbations. Clinically, fragile parameters may suggest targets for therapeutic intervention in signaling models of disease [239]. Conversely, robustness may be a design criterion in synthetic biology [240]. In developmental biology, robustness is related to the concept of canalization [164]. More generally, these predictions may inform experimental design for hypothesis falsification: Models predict which experimentally observable species are sensitive to small experimental perturbations to suggest experimental targets for model (hypothesis) discrimination.

Beyond model discrimination and inference about system behavior, parameter estimation may be used to infer the structure of biological pathways and genetic regulatory networks [128,138-140,158,241]. Reverse engineering of the gap gene network in *Drosophila* demonstrates both the utility and the challenges of inferring gene regulatory networks from image databases and a mathematical model. The richness of the existing data and tools available to acquire new data to inform models, and the evolution of algorithmic approaches to include diverse data in model optimization continue to drive the systems biology of development forward. Looking forward, our hope is that mechanistic models integrate more closely with experimental inquiry, and that they are more widely used alongside other tools in the biologist's toolbox for experimental discovery.

References

1. Chakrabarty A, Buzzard GT, Rundell AE (2013) Model-based design of experiments for cellular processes. *Wiley Interdisciplinary Reviews-Systems Biology and Medicine* 5: 181-203.
2. Strogatz SH (2001) *Nonlinear dynamics and chaos : with applications to physics, biology, chemistry, and engineering*: Westview Press. 512 p.
3. Tomlin CJ, Axelrod JD (2007) Biology by numbers: mathematical modelling in developmental biology. *Nature Reviews Genetics* 8: 331-340.
4. Umulis D, O'Connor M, Blair S (2009) The extracellular regulation of bone morphogenetic protein signaling. *Development* 136: 3715-3728.
5. Lauffenburger DA, Linderman J (1996) *Receptors: Models for Binding, Trafficking, and Signaling*: Oxford University Press. 376 p.
6. Voit E (2012) *A First Course in Systems Biology*: Garland Science. 496 p.
7. Voit E (2000) *Computational Analysis of Biochemical Systems*. New York, NY: Cambridge University Press. 532 p.
8. Ellner SP, Guckenheimer J (2006) *Dynamic Models in Biology*. Princeton, NJ: Princeton University Press. 329 p.
9. Perrot N, Trelea IC, Baudrit C, Trystram G, Bourguine P (2011) Modelling and analysis of complex food systems: State of the art and new trends. *Trends in Food Science & Technology* 22: 304-314.
10. Kutner M, Nachtsheim C, Neter J, Li W (2005) *Applied Linear Statistical Models*. Fifth ed. New York, NY: McGraw Hill. pp. 1396.
11. Pargett M, Umulis DM (2013) Quantitative model analysis with diverse biological data: Applications in developmental pattern formation. *Methods* 62: 56-67.
12. Schaber J, Klipp E (2011) Model-based inference of biochemical parameters and dynamic properties of microbial signal transduction networks. *Current Opinion in Biotechnology* 22: 109-116.
13. Jaeger J (2011) The gap gene network. *Cellular and Molecular Life Sciences*: 243-274.
14. Driever W, Nusslein-Volhard C (1988) A gradient of Bicoid protein in *Drosophila* embryos. *Cell* 54: 83-93.

15. Gregor T, Wieschaus E, McGregor A, Bialek W, Tank D (2007) Stability and nuclear dynamics of the bicoid morphogen gradient. *Cell*: 141-152.
16. Jaeger J, Sharp D, Reinitz J (2007) Known maternal gradients are not sufficient for the establishment of gap domains in *Drosophila melanogaster*. *Mechanisms of Development*: 108-128.
17. Gregor T, Bialek W, van Steveninck R, Tank D, Wieschaus E (2005) Diffusion and scaling during early embryonic pattern formation. *Proceedings of the National Academy of Sciences of the United States of America*: 18403-18407.
18. Driever W, Siegel V, Nusslein-Volhard C (1990) Autonomous determination of anterior structures in the early *Drosophila* embryo by the Bicoid morphogen. *Development*: 811-820.
19. Driever W, Thoma G, Nusslein-Volhard C (1989) Determination of spatial domains of zygotic gene-expression in the *Drosophila* embryo by the affinity of binding-sites for the Bicoid morphogen. *Nature*: 363-367.
20. St. Johnston D, Driever W, Berleth T, Richstein S, Nusslein-Volhard C (1989) Multiple steps in the localization of Bicoid RNA to the anterior pole of the *Drosophila* oocyte. *Development*: 13-19.
21. Driever W, Nusslein-Volhard C (1988) The Bicoid protein determines position in the *Drosophila* embryo in a concentration-dependent manner. *Cell*: 95-104.
22. Wu Y, Myasnikova E, Reinitz J (2007) Master equation simulation analysis of immunostained Bicoid morphogen gradient. *BMC Systems Biology*.
23. Alves F, Dilao R (2006) Modeling segmental patterning in *Drosophila*: Maternal and gap genes. *Journal of Theoretical Biology* 241: 342-359.
24. Reinitz J, Mjolsness E, Sharp DH (1995) Model for cooperative control of positional information in *Drosophila* by Bicoid and maternal Hunchback. *Journal of Experimental Zoology* 271: 47-56.
25. Ibanes M, Belmonte JCI (2008) Theoretical and experimental approaches to understand morphogen gradients. *Molecular Systems Biology* 4.
26. Jackle H, Tautz D, Schuh R, Seifert E, Lehmann R (1986) Cross-regulatory interactions among the gap genes of *Drosophila*. *Nature* 324: 668-670.
27. Hulskamp M, Pfeifle C, Tautz D (1990) A morphogenetic gradient of Hunchback protein organizes the expression of the gap genes Krüppel and Knirps in the early *Drosophila* embryo. *Nature* 346: 577-580.

28. Bronner G, Jackle H (1991) Control and function of terminal gap gene activity in the posterior pole region of the *Drosophila* embryo. *Mechanisms of Development*: 205-211.
29. Eldon E, Pirrotta V (1991) Interactions of the *Drosophila* gap gene Giant with maternal and zygotic pattern-forming genes. *Development* 111: 367-378.
30. Kraut R, Levine M (1991) Mutually repressive interactions between the gap genes Giant and Krüppel define the middle body regions of the *Drosophila* embryo. *Development* 111: 611-621.
31. Capovilla M, Eldon E, Pirrotta V (1992) The giant gene of *Drosophila* encodes a B-zip DNA-binding protein that regulates the expression of other segmentation gap genes. *Development* 114: 99-112.
32. Struhl G, Johnston P, Lawrence P (1992) Control of *Drosophila* body pattern by the Hunchback morphogen gradient. *Cell* 69: 237-249.
33. Sanchez L, Thieffry D (2001) A logical analysis of the *Drosophila* gap-gene system. *Journal of Theoretical Biology*: 115-141.
34. Jaeger J, Blagov M, Kosman D, Kozlov K, Manu, *et al.* (2004) Dynamical analysis of regulatory interactions in the gap gene system of *Drosophila melanogaster*. *Genetics*: 1721-1737.
35. Jaeger J, Surkova S, Blagov M, Janssens H, Kosman D, *et al.* (2004) Dynamic control of positional information in the early *Drosophila* embryo. *Nature*: 368-371.
36. Fomekong-Nanfack Y, Kaandorp J, Blom J (2007) Efficient parameter estimation for spatio-temporal models of pattern formation: case study of *Drosophila melanogaster*. *Bioinformatics* 23: 3356-3363.
37. Ashyraliyev M, Jaeger J, Blom J (2008) Parameter estimation and determinability analysis applied to *Drosophila* gap gene circuits. *BMC Systems Biology* 2: doi:10.1186/1752-0509-1182-1183.
38. Ishihara S, Shibata T (2008) Mutual interaction in network motifs robustly sharpens gene expression in developmental processes. *Journal of Theoretical Biology*: 131-144.
39. Ashyraliyev M, Siggins K, Janssens H, Blom J, Akam M, *et al.* (2009) Gene Circuit Analysis of the Terminal Gap Gene huckebein. *PLoS Computational Biology* 5: doi:10.1371/journal.pcbi.1000548.
40. Fomekong-Nanfack Y, Postma M, Kaandorp J (2009) Inferring *Drosophila* gap gene regulatory network: a parameter sensitivity and perturbation analysis. *BMC Systems Biology*.

41. Manu, Surkova S, Spirov A, Gursky V, Janssens H, *et al.* (2009) Canalization of Gene Expression and Domain Shifts in the *Drosophila* Blastoderm by Dynamical Attractors. PLoS Computational Biology 5: DOI: 10.1371/journal.pcbi.1000303.
42. Hengeniuss J, Gribskov M, Rundell A, Fowlkes C, Umulis D (2011) Analysis of Gap Gene Regulation in a 3D Organism-Scale Model of the *Drosophila melanogaster* Embryo. Plos One 6.
43. Kozlov K, Surkova S, Myasnikova E, Reinitz J, Samsonova M (2012) Modeling of Gap Gene Expression in *Drosophila* Krüppel Mutants. PLoS Computational Biology 8: DOI: 10.1371/journal.pcbi.1002635.
44. Jimenez-Hornero JE, Santos-Duenas IM, Garcia-Garcia I (2009) Optimization of biotechnological processes. The acetic acid fermentation. Part II: Practical identifiability analysis and parameter estimation. Biochemical Engineering Journal 45: 7-21.
45. Bieler J, Pozzorini C, Naef F (2011) Whole-embryo modeling of early segmentation in *Drosophila* identifies robust and fragile expression domains. Biophysical Journal 101: 287-296.
46. Anscombe F (1973) Graphs in Statistical Analysis. The American Statistician 27: 17-21.
47. Cover T, Thomas J (1991) Elements of Information Theory: Wiley Interscience. 576
48. Guinee RA, Lyden C, Aacc, Aacc A. Motor parameter identification using response surface simulation and analysis. Proceedings of the American Control Conference; 2001; Arlington, Va. pp. 4597-4602.
49. Müller M (2007) Information Retrieval for Music and Motion: Springer-Verlag New York, Inc.
50. Deza M, Deza E (2009) Encyclopedia of Distances. 2 ed. Berlin, Heidelberg: Springer-Verlag.
51. Saltelli A, Ratto M, Andres T, Compolongo F, Cariboni J, *et al.* (2008) Global Sensitivity Analysis: The Primer. Chichester, West Sussex, UK: Wiley. 282 p.
52. Kauffman SA (1993) The origins of order: Self-organization and selection in evolution. The origins of order: Self-organization and selection in evolution: xviii+709p-xviii+709p.
53. Spall JC (2003) Introduction to Stochastic Search and Optimization. Hoboken, N.J.: Wiley.

54. Alajlan N (2011) HopDSW: An approximate dynamic space warping algorithm for fast shape matching and retrieval. *Journal of King Saud University - Computer and Information Sciences* 23: 7-14.
55. Umulis D, Shimmi O, O'Connor M, Othmer H (2010) Organism-Scale Modeling of Early *Drosophila* Patterning via Bone Morphogenetic Proteins. *Developmental Cell* 18: 260-274.
56. Bazil JN, Buzzard GT, Rundell AE (2012) A Global Parallel Model Based Design of Experiments Method to Minimize Model Output Uncertainty. *Bulletin of Mathematical Biology* 74: 688-716.
57. PubMed.gov. Bethesda, MD: National Center for Biotechnology Information, U.S. National Library of Medicine.
58. Noble SL, Sherer E, Hannemann RE, Ramkrishna D, Vik T, *et al.* (2010) Using adaptive model predictive control to customize maintenance therapy chemotherapeutic dosing for childhood acute lymphoblastic leukemia. *Journal of Theoretical Biology* 264: 990-1002.
59. Chen BS, Lin YP (2013) A Unifying Mathematical Framework for Genetic Robustness, Environmental Robustness, Network Robustness and their Trade-offs on Phenotype Robustness in Biological Networks. Part III: Synthetic Gene Networks in Synthetic Biology. *Evolutionary Bioinformatics* 9: 87-109.
60. Siegal ML, Bergman A (2002) Waddington's canalization revisited: Developmental stability and evolution. *Proceedings of the National Academy of Sciences of the United States of America* 99: 10528-10532.
61. Perkins T, Jaeger J, Reinitz J, Glass L (2006) Reverse engineering the gap gene network of *Drosophila melanogaster*. *PLoS Computational Biology* 2: DOI: 10.1371/journal.pcbi.0020051.
62. MacNamara A, Terfve C, Henriques D, Bernabe BP, Saez-Rodriguez J (2012) State-time spectrum of signal transduction logic models. *Physical Biology* 9: 045003. doi: 10.1088/1478-0439/9/4/045003

CHAPTER 5. THE STATE OF THE ART AND FUTURE DIRECTIONS

The gap genes of *D. melanogaster* are an attractive model system for the study of developmental genetic regulatory networks. They represent a relatively small and tractable GRN with almost three decades of experimental literature[110,113,114,116,117,152-156]. Before modeling approaches were brought to bear, experimental data consisted of primarily mutant phenotypes. Using these data, developmental biologists were able draw conclusions about genetic interactions. However, studies were often limited to examining regulatory interactions between pairs of genes[114,116,153,155]. The ability to quantify the gap gene products with increasing spatiotemporal resolution has allowed a decade's worth of dynamic model-based inferences about the genes' interactions. In addition to predicting GRNs[128,138,139,157,158,160], these models have been interrogated as surrogate systems for testing the effects biophysical transport processes and transport's effect on developmental patterning[126,142,242-244].

Many open questions remain regarding the specific regulatory interactions of the gap gene system and the genetic, physical, and evolutionary properties of pattern formation during development. Part of my future work will be implementation of a discrete-state dynamic model of the gap gene network. This type of simplified model loses a degree of

quantitative information (proteins are either absent or present) and biological realism, but can decrease computational time by several orders of magnitude. The model's parameter space is also discretized to a finite number of GRNs; this reduces the size of the search and will allow complete screen of the parameter space via parallelized computing. The study will serve multiple functions. It will allow identification of the set of GRNs capable of generating observed gene expression data, though the coarse-grained nature of the discrete parameters may prevent some continuous solutions from being reported. The mapping of genotypic GRN structures to phenotypic morphological outcomes will suggest classes of regulatory “motifs” – common patterns of connectivity that generate similar phenotypic outcomes or regulatory strategies (*e.g.*, lateral inhibition[245]). Finally, the ongoing publication of several *Drosophilae* genomes now allows for prediction of the cis-regulatory elements in different *Drosophila* species[246-248]. Using genomic knowledge to focus on subsets of the complete GRN-to-phenotype mapping, I will determine which, if any, of each species genome-compatible GRNs give rise to species-specific patterning. Whereas the GRN-to-phenotype map may identify patterns of regulation, this species-specific analysis can provide knowledge of developmental GRN evolution.

My analysis of the gap gene system brought to light several shortcomings of current modeling approaches. The imposition of internal domain boundaries – a practice widely adopted in the 1D gap gene modeling literature[128,138,140,158,160,161,163] – artificially constrains protein concentrations at these boundaries and has the potential to add systemic errors near the domain boundaries. I avoided this source of error by

modeling proteins of the entire embryonic domain (Chapter 3). Analysis of the 1D models in Chapter 3 revealed the shortcomings of common error quantification methods and led me to characterize several classes of objective functions (Chapter 4). Comparing these objective functions led to the development of objective function selection criteria for optimal research-specific objectives. The most concerning limitation of existing models is the lack of precautions to avoid overfitting. This phenomenon occurs when many unknown parameters must be estimated; estimation may be inaccurate because many parameter values are altered to partially account for noise in data. The resulting GRNs reproduce the data to which they were fit, but are unrealistic in that they make poor predictions of new data[36]. The parameter estimation problem emphasizes the challenge of simultaneously searching for many unknown parameters in any high-dimensional (here, 28+ parameter) spaces. Despite the large number of unknown parameters, other gap gene modeling studies report alternative GRNs obtained via comparable parameter estimation methods (sometimes searching 40+ parameter)[128,138,139,158]. The striking disparity between these wildtype-consistent optimization and my GRN optimization outcomes has led me to consider current modeling approaches in the field and highlights underlying shortfalls of many biological modeling studies.

Since the early models of the 2000s, gap gene modelers have become increasingly ambitious, attempting to incorporate additional genes and biological interactions into their simulations[140,161]. The goal seems to be the construction of more comprehensive *Drosophila* gap gene models on which the sufficiency of “virtual hypotheses” may be

tested. This type of integrative modeling may foster greater understanding of so-called emergent behaviors unattainable by reductionist approaches, but model interpretability and predictive reliability suffer as the number of parameters grows. As the meaning of model behavior is obscured, the concept of what constitutes a successful modeling study becomes unclear. To date, the implicit criteria for a successful gap gene model have been its ability to recapitulate the expression data to which model parameters were fit and, sometimes, subsequent evaluation of model robustness to parameter perturbations[157,160]. The latter criterion is based on the evolutionary-developmental assumption that robustness protects embryonic development from environmental perturbations and is a trait subjected to positive selection[245]. This approach to model assessment fails to evaluate the crucial feature of dynamic models – their ability to predict new data. This model validation is performed by generating new test data against which the model error is computed or, when generation of additional data is infeasible, partitioning of the available data into training and test sets (cross-validation)[249].

In gap gene modeling, the effect of neglecting validation is best illustrated by the failure of reported GRNs to correctly predict the behavior of mutant phenotypes when the models are “mutated” (*e.g.*, a gene’s expression level is set to zero to represent a knockout mutant). The only model to date capable of reproducing a Krüppel mutant phenotype was fit using mutant data[163]; as such, it did not predict the phenotype independent of training. The model incorporated artificial internal boundary conditions that further render the biological GRN inferences suspect. With this exception, inferred

GRNs are not yet capable of predicting mutant test data, strongly indicating overfitting of the model.

Overfitting occurs when data-model error itself is predicted by fitting many “nuisance parameters” – parameters which may not correspond to any true biological interaction[250]. This leads to unrealistic parameter values (*e.g.*, a gap gene regulatory parameter $w_{a \rightarrow b}$ may take a promoting or repressing value to compensate for error even though genes a and b do not interact *in vivo*). When new data are predicted with these unrealistic GRNs, the results are unlikely to agree with test data.

This characteristic failure of model-inferred GRNs to predict new data demands reevaluation of existing work and incorporation of measures to counter overfitting in future studies. Until overfitting is accounted for, the simulation of complex biological systems will grow harder to interpret as many parameter values are modified to account for residuals between model and data. In this chapter, I discuss two approaches, used frequently in regression and statistical models[36,251], to reduce overfitting in the gap gene system. Finally, I present preliminary work on a simplified discrete -space, -time, -concentration, and -parameter model that allows a full search of the GRN parameter space.

5.1 Overfitting and Its Implications

The problem of overfitting arises from a fundamental tradeoff between a model’s ability to exactly fit a particular dataset (referred to as bias in statistical literature) and its

residual error (referred to as variance)[252]. Too much variance is equivalent to a poor model fit using error metrics, but too much bias toward particular data sometimes prevents a model from making generalizable biological predictions.

To demonstrate this tradeoff, consider the following empirical model fitting. Unlike mechanistic models that are constrained by assumptions about the systems under study, these models attempt to fit various functions to data without mechanistic interpretation. The black points of Figure 5.1A represent data generated from a linear function with normally distributed noise ε ,

$$y = 2x + 4 + \varepsilon \quad (5.1a)$$

$$\varepsilon = N(0,0.25). \quad (5.1b)$$

The blue and red lines of Figure 5.1A represent fits to the training data for a linear model with 2 parameters,

$$\hat{y} = ax + b, \quad (5.2)$$

and a sum of sines model with 24 parameters,

$$\hat{y} = a_1 \sin(b_1x + c_1) + a_2 \sin(b_2x + c_2) + \cdots + a_8 \sin(b_8x + c_8), \quad (5.4)$$

respectively. To compare the quality of each fit, the Euclidean distance between the model predictions (\hat{y} values) and training data (y values) is computed:

$$J_{Euclidean} = \sum_{i=1}^n (\hat{y}_i - y_i)^2. \quad (5.5)$$

Here, there are n training data. Values \hat{y}_i and y_i are the i th prediction and datum, respectively. It is clear from visual comparison of Fig. 5.1A that the distance between training data (black points) and the sum of sines predictions (red line) is less than the distance between training data and the linear fit (blue line). The sum of sines fit has a Euclidean distance of 0.711 when fit to the training data, but it exhibits multiple maxima and minima absent from the linear function used to generate data. However, the “true” linear model that originally generated the training data has a larger error (Euclidean distance = 3.52) when compared to the training data. Without further analysis, these results might suggest that the sum of sines is a preferable model.

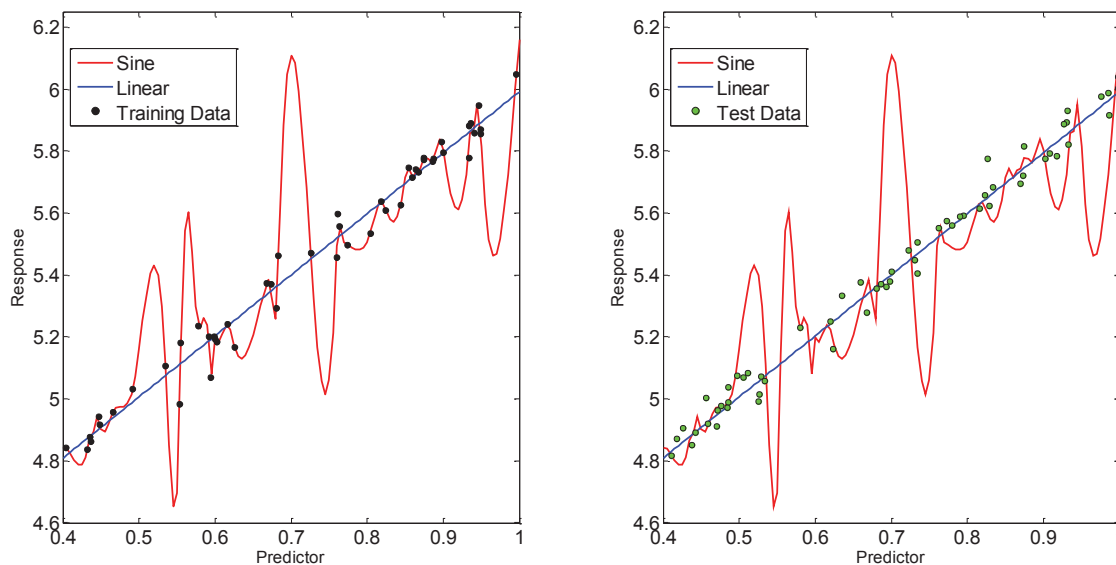


Figure 5.1 Overfitting and Model Complexity

Comparison of two empirical fits to synthetic training data (A, black points). Red lines represent an eight-term sum of signs function with 24 parameters (amplitude a , frequency b , and phase c for each term) fit to the training data in A. Blue lines represent a linear function with two parameters (slope and intercept) fit to training data in A. The sine function fits training data with a Euclidean error of 0.711 and the linear function fits training data with a Euclidean error of 3.52. Additional test data (B, green points) is used to evaluate sine and linear fits. The sine function fits test data with a Euclidean error of 17.58 and the linear function fits test data with a Euclidean error of 3.71.

However, the above fits are based solely on the training data (Fig. 5.1A, black points). Without a secondary test dataset, the bias-variance tradeoff of the two fits cannot be evaluated. In an ideal situation, additional test data is generated and the models' ability to predict these data is compared. Consider a new test dataset drawn from the same distribution as the training data (eqn. 5.1) in Figure 5.1B (green points). The linear fit demonstrates a modest increase in Euclidean error (from 3.52 to 3.71) when predicting the test data, but the sine function Euclidean error increases from 0.711 to 17.58. As the "true" model used to generate the training and test sets, the linear model provides the optimal tradeoff of bias and variance. The more complex sum of sines model produces a better fit to the training data, but it is biased; it fits the normally distributed noise in addition to the underlying linear signal.

Overfitting behavior is also observed in dynamic modeling constrained by mechanistic assumptions (encoded into the system of differential equations)[253]. One of the assumptions underlying the current gap gene modeling paradigm is that fitting an entirely interconnected GRN with 28+ potential interactions will result in GRNs with realistic biological interactions. As seen in the empirical sum of sines model, the inclusion of many parameters creates the possibility that some of these parameters assume unrealistic values to reduce error between the model and training data. Because no standard reference exists for the true genetic interactions in the gap gene system, it is not possible to directly assay overfitting by comparing GRNs to the reference. Even without a direct test, current results suggest that overfitting is occurring. Existing models perform poorly when used to predict additional mutant test data. This result may be attributable to other

causes such as incorrect or incomplete model structures (hypothesized mechanisms), but it is consistent with bias due to overfitting. Theoretical work and empirical findings suggest that GRNs tend to be sparsely connected[254-257]. However, the simulation-inferred GRNs exhibit many genetic interactions[127,140,157,158,160,161,163] with relatively few low magnitude, near-zero edges (*e.g.*, see low magnitude regulatory parameters WKr,Hb , $WTll,Hb$, $WKni,Gt$, $WBcd,Tll$, $WTll,Tll$ in Chapter 3, Figure 1). Together, the discrepancy between the expected sparsity of the true network and the highly interconnected inferred network, coupled with the poor predictive power of extant models, suggests that key findings reported from modeling studies have been based on overfit and unrealistic models.

There are steps that can be implemented to reduce the effects of overfitting in gap gene simulations. One method is model validation. As discussed, this involves comparison of the parameterized model output to new test data. A general test of a model's power is to predict additional data, but good fits to training data coupled with poor predictions of training data are indicative of overfitting[258]. Validation depends on the ability to generate new test data or set aside data as a test set. In situations where all available data must be used for training and generation of new data is infeasible, cross-validation techniques iteratively withhold subsets of data for model testing. The resulting parameters sets are evaluated by how well they predict the withheld data. Finally, the requirement for GRN sparsity can be enforced during parameter estimation by inclusion of a regularizer in the objective function. This is a term that penalizes the non-zero parameter values, countering the decrease in residual error that occurs when error is

compensated for by many parameters[259]. Using these methods in combination with model-based gap gene GRN inference may increase the realism of predicted GRNs (assuming the underlying model is sufficient), and will reduce effects of overfitting.

5.2 Countering Overfitting

Extant gap gene models behave in ways that are consistent with biological observations and intuition – when simulating wildtype data. Some model dynamics have proven robust to perturbations, which is thought to ensure healthy growth of developmental systems[260-279]. Jaeger *et al.*'s original model predicted genetic regulatory interactions consistent with experimental evidence. However, the lack of compensation for overfitting makes extrapolations suspect. Reevaluating the parameter-estimation-as-inference approach while controlling for overfitting is a logical step to advancing model-driven studies of the gap gene system. To do this, I propose regularization of objective functions during parameter estimation and cross-validation of models' performance with the estimated GRNs.

Validation of the gap gene system seems straightforward. Generate new data against which model can be tested, then discard GRNs that cannot predict the new data within a user-specified margin of error. However, generation of new data is not always a viable option, especially when a model is constructed and its parameters are estimated using previously published datasets. When data generation is not an option, another option is to withhold some data from training and use it as a test set. In this case, there is tension between how much data should be used to train a model and how much should be

retained for testing. For example, inclusion of mutant data in the training set for a gap gene model should lead to parameter estimates (GRNs) capable of accounting for both wildtype and mutant data[163], but this approach prevents the use of mutant data for testing. Mutant data is often reported qualitatively, further complicating comparison with qualitative model output[32]. “Conventional wisdom” in this research area is that data is wasted when it is withheld from testing; GRN parameters are typically trained on all available data and analyze the resulting GRNs without further validation.

To address the lack of validation in current models while reducing the “waste” of data for training, I propose use of cross-validation to test GRN performance. This resampling approach involves iteratively (i) partitioning available data into training and test sets, (ii) estimating parameters using the training partition, (iii) evaluating performance on the test partition, and then repeating the process after repartitioning data into new training and test sets[249]. Though some overfitting will occur in any dataset containing noise, cross-validation has been shown to reduce the effects of overfitting. In this approach, GRNs with the best performance during testing can be ranked according to their test set residuals.

Using the steps outlined above, cross-validation reduces the waste of testing data – all of the data are used as training and test data in in different partitions – while countering the effects of overfitting. In the simplest - but most costly - version of cross-validation, leave-one-out cross-validation, one point of n data is retained for testing and $n - 1$ data are used for training. Iteratively, each of the n points is withheld, the parameters are estimated,

and the testing error computed[249]. However, the computational cost of parameter estimation makes this approach infeasible. Parameter estimation for the 3D gap gene model, discussed in Chapter 3, requires approximately 180 seconds per model evaluation and may take weeks to estimate a single parameter set. With a 3D dataset of approximately $n = 2.4 \times 10^4$ points, repeating parameter estimation n times is not a realistic possibility. Even 1D model variants, which require approximately half a second per evaluation and use less numerous 1D data, may need hours to days for parameter estimation.

K -fold cross-validation avoids this computational bottleneck by sacrificing the number of training data for computation efficiency. Available data are divided into k randomly chosen partitions. In each iteration of parameter estimation, one partition is withheld as test data while $k - 1$ partitions are used for training. Parameter estimation is performed k times, where k is smaller and more tractable than n . (Leave-one-out cross-validation occurs when k is equal to n .) This method never trains GRNs on more than $k - 1$ partitions, meaning that $\frac{100}{k}\%$ of the data is “wasted” on training in any given iteration. I propose reevaluating key model findings including Jaeger *et al.*’s original six-gene model[138], Manu *et al.*’s reduction to four genes[161], and the Ashyraliyev *et al.*’s inclusion of the protein Hucklebein[140] to see how their inferred GRNs compare to cross-validated variants.

Cross-validation provides one way to control for overfitting; regularization provides another. Regularization is commonly used in regression to minimize the number of

predictors – and therefore parameters – in a model[251]. Consider a regression problem in which a dependent variable y may be predicted by independent variables x_1 through x_p ,

$$y = b_0 + b_1x_1 + b_2x_2 + \cdots + b_px_p + \varepsilon. \quad (5.6)$$

Parameters b_0 through b_p may all be assigned nonzero values during parameter estimation, but this is likely to result in overfitting of the model to account for both signal and noise in y . Suppose the objective function used in parameter estimation is the sum of squared error (SSE),

$$J(\mathbf{b}) = \sum_{i=1}^n (\hat{y}_i(\mathbf{b}) - y_i)^2, \quad (5.7)$$

where \mathbf{b} is the parameter vector containing b_0 through b_p , $\hat{y}_i(\mathbf{b})$ is the model prediction of the i th data point, y_i is the i th data point. When minimized, this formulation of the objective function will minimize overall training error, but not the number of nonzero parameters. When an L_1 -norm regularizer is included,

$$J(\mathbf{b}) = \sum_{i=1}^n (\hat{y}_i(\mathbf{b}) - y_i)^2 + \lambda \|\mathbf{b}\|_1, \quad (5.8a)$$

where λ is a scaling term and $\|\mathbf{b}\|_1$ is the L_1 -norm of \mathbf{b} ,

$$\|\mathbf{b}\|_1 = \sum_{i=0}^p |b_i|, \quad (5.8b)$$

the second term acts as a penalty as the magnitudes of the parameter values increase. The λ factor scales this penalty so that it is of the same magnitude as the SSE error metric. The L_1 -norm regularizer acts to concentrate model error into fewer nonzero parameters rather than selecting for the overall lowest training error[251]. Though eqn. 5.7 might return a lower overall error, eqn. 5.8 penalizes overfitting. In the context of the gap gene system, the regularizer should produce sparse GRNs consistent with theoretical evolutionary models[255,256].

Together, these measures against overfitting may lead to radically different – and possibly more biologically realistic – GRNs than have been previously inferred. Although the lack of a “gold standard” reference for the GRN prevents an absolute measure of overfitting and GRN error, reevaluation of prior predictions in light of these additional constraints is a crucial initial step for further model-driven studies of the gap gene system.

The issue of overfitting arises in part from the large number of unknown free parameters that are optimized. Without using prior knowledge to constrain and fix parameter values in advance, more parameters are available to compensate for error. The large number of continuous parameters also limits the coverage of any search algorithms used during parameter estimation. Trading biological detail for computational efficiency, I am developing a time-, space-, and state-discrete model of the gap gene system.

5.3 A Complete Search of the Gap Gene Parameter Space

Though the continuous models of the gap gene system provide quantitative protein expression values and near-continuous time resolution, the large parameter spaces associated with them prevent exhaustive searches for possible GRNs. Due to the sheer size of the space, there is no guarantee that GRNs capable of simulating biological data will be found in a particular search. To increase the coverage of possible GRNs, I am designing an efficient discretized version of the 1D gap gene model using discrete concentration states ($c = 0$ or 1 , present or absent), spatial positions ($x = 1$ to length l), times ($t = 1, 2, \dots$) and parameters ($w_{a,b} = -1, 0, \text{ or } 1$, inhibitory, neutral, promoting). This last discretization changes the parameter search from one performed on a continuously searchable 28+ dimensional space to one performed on 3^{24} to 3^{28} ($\approx 2.82 \times 10^{11}$ to 2.29×10^{13} depending on the model variant) discrete possible GRNs. These numbers are within the upper range of model evaluations that may feasibly be computed with efficient software and access to sufficient CPUs.

This model approximates the PDEs of the 1D model of Manu *et al*[161]. Only four gap gene products are simulated in this system: Gt, Hb, Kni, and Kr. Cad and Tll are treated as inputs that vary over time, but their dynamics are interpolated from data and are independent of the simulated transcription factors (Fig. 5.2). This PDE system is similar to the one described in Chapter 3. Each of the four simulated transcription factor's concentrations are modeled by a differential equation,

$$\frac{\partial c_a}{\partial t} = D_a \nabla^2 c_a + R_a \phi(u_a) - \lambda_a c_a, \quad (5.9)$$

where a represents each of the four simulated species. The first term, containing the diffusion constant D_a times the spatial gradient of transcription factor a , represents diffusion. The last term models first degree decay with the kinetic constant λ_a , and the middle term controls gene expression. R_a is the maximum expression for protein a and $\phi(u_a)$ is a sigmoidal function,

$$\phi(u_a) = \frac{1}{2} \left(\frac{u_a}{\sqrt{u_a^2 + 1}} + 1 \right), \quad (5.10)$$

that acts as a switch – gene expression is repressed when u_a is negative and enhanced when u_a is positive. The argument u_a is evaluated across the spatial domain and sums positive and negative regulatory effects of all genes present at each position,

$$u_a = h_a + \sum_{b=1}^7 w_{b,a} c_b. \quad (5.11)$$

The h_a term is positive or negative, representing intrinsic expression or inhibition, respectively. Index b represents each of the seven total simulated and independent proteins, Bcd, Cad, Gt, Hb, Kni, Kr, and Tll. Regulatory parameters (GRN edges) $w_{b,a}$ are positive or negative, representing enhancement or inhibition of protein a by protein b , respectively.

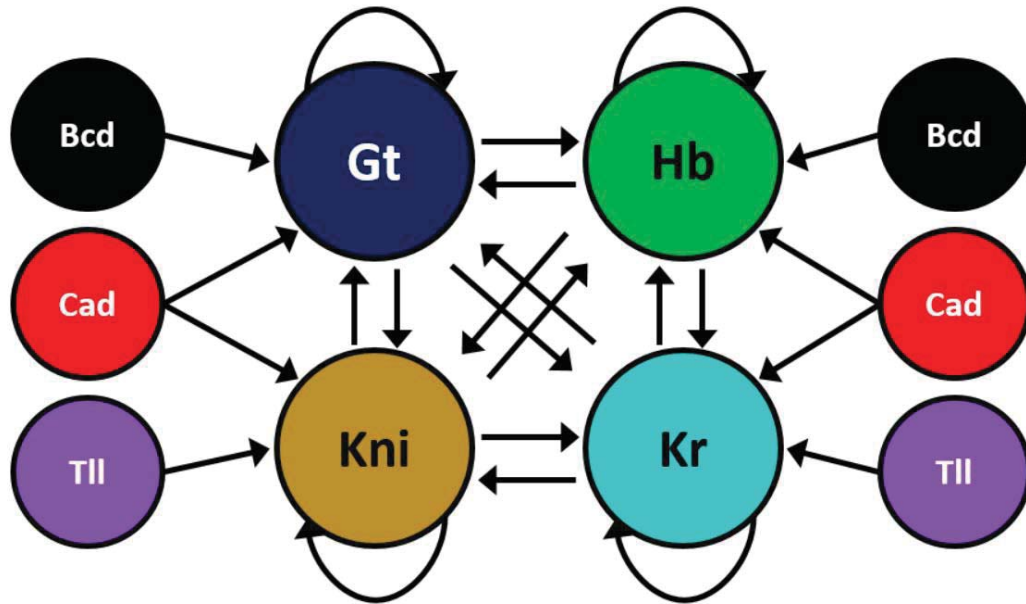


Figure 5.2 Reduced Four-Species Gap Gene Model

This reduced GRN represents genetic regulatory interactions between four simulated proteins, Gt, Hb, Kni, and Kr. Regulation of these proteins are subject to three independent inputs with spatiotemporal dynamics independent of the simulated proteins (*i.e.*, interpolated from data). Each arrow represents a regulatory parameter dictating the effect of a regulatory protein on its target. Negative parameters indicate repressor activity and positive parameters indicate promoter activity. Parameters with magnitudes of zero indicate absence of regulatory interactions.

This continuous spatiotemporal system has been converted into a discrete model with the following simplifications. The 1D domain has been divided into l segments with reflective boundary conditions at either AP extreme. Proteins are either present or absent at each segment. More importantly, time has been treated as a series of updates of the system states. This is a notable departure from the continuous case because the solver no longer chooses intervals to minimize error; rather, the time interval is effectively scaled to the slowest biochemical or physical process occurring in the system (usually protein degradation). Faster processes are assumed to occur during the duration of the interval, and this method sometimes leads to unrealistic behavior of the system. To account for these change in space, state, and time representations, the model's state update method differs substantially from the PDE solver approach. For each position segment x , the binary system state indicates the presence (1) or absence (0) of protein a is determined as follows:

$$c_a(x, t + 1) = \begin{cases} 1, & \text{if } u_a(x) > 0 \\ 0, & \text{if } u_a(x) \leq 0 \end{cases} \quad (5.12a-b)$$

Note that explicit diffusion and decay terms have been removed in this formulation. Transport is now accounted for in the regulatory term $u_a(x)$, and decay is implicit in the discrete time update rule. In the absence of regulation, or when repressors and promoters “cancel out” ($u_a(x) = 0$ in eqn. 5.12b), proteins are assumed to degrade to zero before the next time update. The structure of $u_a(x)$ is also modified in this model. Notably, it is now a function of the spatial coordinate x due to the incorporation of mass transport:

$$u_a(x) = \begin{cases} \sum_{b=1}^7 2w_{b,a}c_b(x, t) + w_{b,a}[c_b(x-1, t) + c_b(x+1, t)] & \text{if } x \neq 1, l \\ \sum_{b=1}^7 w_{b,a}c_b(x, t) + w_{b,a}c_b(x+1, t) & \text{if } x = 1. \\ \sum_{b=1}^7 w_{b,a}c_b(x, t) + w_{b,a}c_b(x+1, t) & \text{if } x = l \end{cases} \quad (5.13a-c)$$

This modified function now accounts for diffusion and gene expression. The first term in this summation is similar to the original regulatory function in eqn. 5.11; it sums the regulatory weights $w_{b,a}$ of each transcription factor present at position x . However, each transcription factor b now takes a value of one or zero and regulatory weights $w_{b,a}$ take values of negative one, zero, or one depending on the GRN. The second term of the summation implicitly represents diffusion. Because each time step is deemed sufficiently long to allow all biophysical processes to occur before the next iteration, regulation is updated assuming transcription factors have diffused from adjacent spatial segments (at $x-1, x+1$). In the cases of the AP extrema ($x=1$ or l), the form of u_a is modified remove contributions from nonexistent segments (*i.e.*, $x=0$ or $l+1$, eqns. 13b-c) and the remaining term is doubled to approximate conservation of mass. Finally, the constitutive expression term h_a is removed to reduce the parameter space to a more tractable size of 3^{24} . A more complicated model variant can incorporate constitutive expression into eqn. 5.12 to form,

$$c_a(x, t+1) = \begin{cases} 1, & \text{if } u_a(x) + h_a > 0 \\ 0, & \text{if } u_a(x) + h_a \leq 0 \end{cases}, \quad (5.14a-b)$$

but this variant increases the GRN search space to 3^{28} networks, pushing the limits of computational resources.

In either model variant, the same starting information required for PDEs is needed for model evaluation. The initial states at the first time point are required; the discretized versions (thresholds set to $\frac{1}{2}$ maximum for each protein species) are shown in Figure 5.3A. A GRN parameter set is also required, with each edge in Figure 5.2 assigned a value of negative one, zero, or one. The error between model and data is calculated by summing the residuals between model output and discretized data (Fig. 5.3A). Lack of standardized conversion methods for transforming qualitative mutant data to the discrete representations in Figure 5.3 may limit available training data (and there are few data points that may be withheld for training). Regularization of the discretized parameter sets remains an option to control for overfitting.

Currently, the model is implemented in Matlab and conversion to more efficient C code is in progress. This will allow for efficient memory management and faster evaluation times, making complete surveys of the GRN search space less computationally expensive. Even the relatively slow Matlab implementation has recovered near-matches (Fig. 5.3B) to the training data in Figure 5.3A. These GRNs were obtained using only random sampling of the GRN space.

Taking into account the potential artifacts caused by the time discretization and the loss of time, space, and concentration resolution, these discrete models are not replacements for continuous PDE simulations. Rather, they will serve as a screening tool for identification of coarse integer-valued GRNs that reproduce model data. Discrete GRNs

producing good fits to data may be used as starting points for parameter estimation in continuous models, reducing the overall computational expense of gap gene modeling.

5.4 Concluding Remarks

This two-pronged approach – critically reevaluating past models after reducing widespread overfitting and completely evaluating the space of possible GRNs – has the potential to improve systemically inaccurate GRN inferences and provide new insights into the working of realistic gap gene GRNs under theoretical evolutionary constraints. It also stands to inform evolutionary-developmental biology. Analysis of common patterns in the complete survey of possible GRNs may reveal regulatory motifs capable of giving rise to spatial patterning; combined with comparative genomics of twelve *Drosophila* genomes, this map of motifs to patterning properties can demonstrate how different *Drosophila* species' morphologies evolved. This work will advance understanding of both the physical processes underlying development and the evolutionary pathways capable of modifying organisms' bodyplans.

The biological focus of this work is the elucidation of poorly understood genetic regulatory networks via modeling and parameter estimation. Dynamic modeling studies in biology are frequently limited by low temporal and/or spatial data resolution, meaning that parameter estimation is often underdetermined. Because data are often insufficient to reveal a single optimal parameter set, our proposed approach will identify the minimally connected GRN(s) in the efficient discrete framework and subsequently optimize parameters on those GRN edges in the quantitative continuous framework. The first step

takes advantage of the fast discrete model simulation and reduced discrete parameter space to allow identification of the smallest GRNs capable of reproducing qualitative expression data. The second step takes advantage of the quantitative accuracy of continuous PDE simulation to determine whether those GRNs can fit quantitative data. In each step of the process, careful selection of objective functions will enhance parameter optimization, while selection of test data for cross-validation will reduce over-fitting, respectively. Once this approach is tested and refined, it may serve as a valuable asset for researchers reverse-engineering complex genetic regulatory systems.

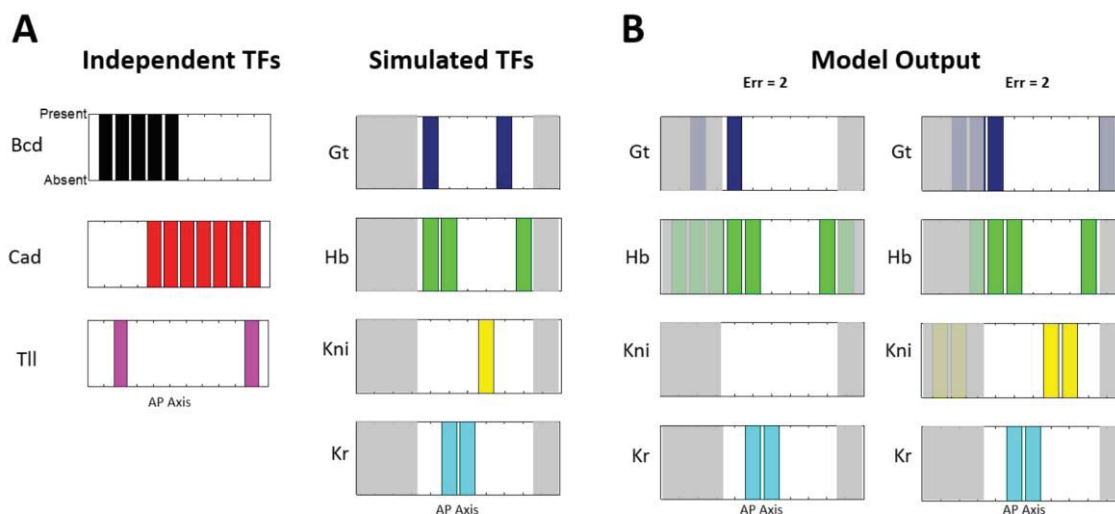


Figure 5.3 Discretized Gap Gene Data and Sample Model Output

(A) Independent transcription factor model inputs and discretized immunofluorescent training data (used to fit simulated transcription factors) were derived from 3D *Drosophila* blastoderm expression data[280]. The AP domain is divided into ten segments. Grayed out areas of the domain represent regions of the embryo where confidence in the model is low; data in these regions are not used for fitting and are omitted from the image. Random searches of the GRN parameter space for the 24-parameter model variant (eqn. 5.12) have yielded no perfect matches with data, but have returned two networks capable of producing model results (B) with errors of two (out of a total of twenty).

REFERENCES

REFERENCES

1. De Backer P, De Waele D, Van Speybroeck L (2010) Ins and outs of systems biology vis-a-vis molecular biology: continuation or clear cut? *Acta Biotheor* 58: 15-49.
2. Ideker T, Galitski T, Hood L (2001) A new approach to decoding life: systems biology. *Annu Rev Genomics Hum Genet* 2: 343-372.
3. Tyson JJ, Chen K, Novak B (2001) Network dynamics and cell physiology. *Nat Rev Mol Cell Biol* 2: 908-916.
4. Kirschner MW (2005) The meaning of systems biology. *Cell* 121: 503-504.
5. Lisacek F, Appel RD (2007) Systems Biology: a loose definition. *Proteomics* 7: 825-827.
6. Boogerd F, Bruggeman FJ, Hofmeyr J-HS, Westerhoff HV (2007) *Systems biology: philosophical foundations*: Elsevier.
7. Brigandt I, Love A (2012) Reductionism in Biology. In: Zalta EN, editor. *The Stanford Encyclopedia of Philosophy*. Summer 2012 ed. Stanford: The Metaphysics Research Lab, Center for the Study of Language and Information
8. Wiener N (1948) *Cybernetics; or, Control and communication in the animal and the machine*. New York,: J. Wiley. 194 p. p.
9. Mesarović MD, Case Institute of Technology. Systems Research Center. (1968) *Systems theory and biology*. Proceedings of the 3rd Systems Symposium at Case Institute of Technology. Berlin, New York etc.: Springer. xii, 403 p. with illus. p.
10. Savageau MA (1969) *Biochemical Systems Analysis* .1. Some Mathematical Properties of Rate Law for Component Enzymatic Reactions. *Journal of Theoretical Biology* 25: 365-&.
11. Savageau MA (1969) *Biochemical Systems Analysis* .2. Steady-State Solutions for an N-Pool System Using a Power-Law Approximation. *Journal of Theoretical Biology* 25: 370-&.
12. Savageau MA (1970) *Biochemical Systems Analysis* .3. Dynamic Solutions Using a Power-Law Approximation. *Journal of Theoretical Biology* 26: 215-&.
13. Hogeweg P (2011) The roots of bioinformatics in theoretical biology. *PLoS Comput Biol* 7: e1002021.
14. Papoutsakis ET (1984) Equations and Calculations for Fermentations of Butyric-Acid Bacteria. *Biotechnology and Bioengineering* 26: 174-187.
15. (1990) Five-Year Plan Goes to Capitol Hill. In: Project USDoEHG, editor. *Human Genome News*, May 1990; 2(1)
ed: Human Genome Management Information System of the Life Sciences Division at Oak Ridge National Laboratory.

16. Fleischmann RD, Adams MD, White O, Clayton RA, Kirkness EF, et al. (1995) Whole-Genome Random Sequencing and Assembly of *Haemophilus-Influenzae* Rd. *Science* 269: 496-512.
17. Pray CE, Naseem A (2005) Intellectual property rights on research tools: incentives or barriers to innovation? Case studies of rice genomics and plant transformation technologies. *AgBioForum* 8: 108-117.
18. Luscombe NM, Greenbaum D, Gerstein M (2001) What is bioinformatics? A proposed definition and overview of the field. *Methods of Information in Medicine* 40: 346-358.
19. (2011) *Bioinformatics - Trends and Methodologies*: Intech.
20. Strogatz SH (2001) *Nonlinear dynamics and chaos : with applications to physics, biology, chemistry, and engineering*: Westview Press. 512 p.
21. Tomlin CJ, Axelrod JD (2007) *Biology by numbers: mathematical modelling in developmental biology*. *Nature Reviews Genetics* 8: 331-340.
22. Umulis D, O'Connor M, Blair S (2009) The extracellular regulation of bone morphogenetic protein signaling. *Development* 136: 3715-3728.
23. Lauffenburger DA, Linderman J (1996) *Receptors: Models for Binding, Trafficking, and Signaling*: Oxford University Press. 376 p.
24. Voit E (2012) *A First Course in Systems Biology*: Garland Science. 496 p.
25. Voit E (2000) *Computational Analysis of Biochemical Systems*. New York, NY: Cambridge University Press. 532 p.
26. Ellner SP, Guckenheimer J (2006) *Dynamic Models in Biology*. Princeton, NJ: Princeton University Press. 329 p.
27. Perrot N, Trelea IC, Baudrit C, Trystram G, Bourguine P (2011) Modelling and analysis of complex food systems: State of the art and new trends. *Trends in Food Science & Technology* 22: 304-314.
28. Claussen JC, Hengenius JB, Wickner MM, Fisher TS, Umulis DM, et al. (2011) Effects of Carbon Nanotube-Tethered Nanosphere Density on Amperometric Biosensing: Simulation and Experiment. *Journal of Physical Chemistry C* 115: 20896-20904.
29. Claussen JC, Franklin AD, ul Haque A, Porterfield DM, Fisher TS (2009) Electrochemical biosensor of nanocube-augmented carbon nanotube networks. *ACS Nano* 3: 37-44.
30. Claussen JC, Kim SS, Haque AU, Artilis MS, Porterfield DM, et al. (2010) Electrochemical glucose biosensor of platinum nanospheres connected by carbon nanotubes. *J Diabetes Sci Technol* 4: 312-319.
31. Pargett M, Umulis DM (2013) Quantitative model analysis with diverse biological data: Applications in developmental pattern formation. *Methods* 62: 56-67.
32. Pargett M (2013) Quantitative analysis for complex biological models using qualitative data: Applications in developmental biology [Dissertation]. Ann Arbor: Purdue University. 187 p.
33. Gennemark P, Wedelin D (2007) Efficient algorithms for ordinary differential equation model identification of biological systems. *IET Syst Biol* 1: 120-129.
34. Toni T, Stumpf MP (2010) Parameter inference and model selection in signaling pathway models. *Methods Mol Biol* 673: 283-295.

35. Chakrabarty A, Buzzard GT, Rundell AE (2013) Model-based design of experiments for cellular processes. *Wiley Interdisciplinary Reviews-Systems Biology and Medicine* 5: 181-203.
36. Kutner M, Nachtsheim C, Neter J, Li W (2005) *Applied Linear Statistical Models*. Fifth ed. New York, NY: McGraw Hill. pp. 372.
37. Chaisson E, McMillan S (2002) *Astronomy today*. Upper Saddle River, N.J.: Prentice Hall.
38. Spall JC (2003) *Introduction to stochastic search and optimization : estimation, simulation, and control*. Hoboken, N.J.: Wiley-Interscience. 595 p.
39. Schaber J, Klipp E (2011) Model-based inference of biochemical parameters and dynamic properties of microbial signal transduction networks. *Current Opinion in Biotechnology* 22: 109-116.
40. Smyth S, Heron A (2006) Diabetes and obesity: the twin epidemics. *Nature Medicine* 12: 75-80.
41. (2013) WHO | The top 10 causes of death. WHO Fact Sheets. N°310 ed: World Health Organization.
42. Minino AM (2013) Death in the United States, 2011. NCHS Data Briefs: 8 pp.
43. Currie CJ, Peyrot M, Morgan CL, Poole CD, Jenkins-Jones S, et al. (2012) The Impact of Treatment Noncompliance on Mortality in People With Type 2 Diabetes. *Diabetes Care* 35: 1279-1284.
44. Malchesky PS (2014) Artificial organs 2013: a year in review. *Artif Organs* 38: 239-267.
45. Carlisle D (2013) The artificial pancreas. *Nurs Stand* 27: 22-23.
46. Robbins JM, Vaccarino V, Zhang H, Kasl SV (2005) Socioeconomic status and diagnosed diabetes incidence. *Diabetes Res Clin Pract* 68: 230-236.
47. Walker JJ, Livingstone SJ, Colhoun HM, Lindsay RS, McKnight JA, et al. (2011) Effect of socioeconomic status on mortality among people with type 2 diabetes: a study from the Scottish Diabetes Research Network Epidemiology Group. *Diabetes Care* 34: 1127-1132.
48. Lane JD, Krumholz DM, Sack RA, Morris C (2006) Tear glucose dynamics in diabetes mellitus. *Curr Eye Res* 31: 895-901.
49. Ye D, Liang G, Li H, Luo J, Zhang S, et al. (2013) A novel nonenzymatic sensor based on CuO nanoneedle/graphene/carbon nanofiber modified electrode for probing glucose in saliva. *Talanta* 116: 223-230.
50. Micheli L, Moscone D, Palleschi G (2012) Biosensors for non-invasive measurements. In: Higson S, editor. *Biosensors for Medical Applications*. pp. 263-300.
51. Wilson GS, Hu Y (2000) Enzyme-based biosensors for in vivo measurements. *Chem Rev* 100: 2693-2704.
52. Jurysta C, Bulur N, Oguzhan B, Satman I, Yilmaz TM, et al. (2009) Salivary glucose concentration and excretion in normal and diabetic subjects. *J Biomed Biotechnol* 2009.
53. Wang J (2008) Electrochemical glucose biosensors. *Chem Rev* 108: 814-825.

54. Kavanagh P, Leech D (2013) Mediated electron transfer in glucose oxidising enzyme electrodes for application to biofuel cells: recent progress and perspectives. *Phys Chem Chem Phys* 15: 4859-4869.
55. Heller A, Feldman B (2010) Electrochemistry in diabetes management. *Acc Chem Res* 43: 963-973.
56. Heller A, Feldman B (2008) Electrochemical glucose sensors and their applications in diabetes management. *Chem Rev* 108: 2482-2505.
57. Baker WS, Crooks RM (1998) Independent geometrical and electrochemical characterization of arrays of nanometer-scale electrodes. *J Phys Chem B* 102: 10041-10046.
58. Sirkar K, Pishko M (1999) Glucose sensor based upon nanoscale multilayered redox polymers. ... in *Medicine and Biology, 1999 21st*
59. Arrigan DWM (2004) Nanoelectrodes, nanoelectrode arrays and their applications. *Analyst* 129: 1157-1165.
60. Fan Y, Goldsmith BR, Collins PG (2005) Identifying and counting point defects in carbon nanotubes. *Nat Mater* 4: 906-911.
61. Song Z, Huang J, Wu B, Shi H, Anzai J, et al. (2006) Amperometric aqueous sol-gel biosensor for low-potential stable choline detection at multi-wall carbon nanotube modified platinum electrode. *Sensors and Actuators B:*
62. Vamvakaki V, Tsagaraki K, Chaniotakis N (2006) Carbon nanofiber-based glucose biosensor. *Analytical chemistry*.
63. Lanyon YH, De Marzi G, Watson YE, Quinn AJ, Gleeson JP, et al. (2007) Fabrication of nanopore array electrodes by focused ion beam milling. *Anal Chem* 79: 3048-3055.
64. Lu Y, Yang M, Qu F, Shen G, Yu R (2007) Amperometric biosensors based on Platinum nanowires. *Analytical letters*.
65. Corres J, Sanz A, Arregui F, Matías I, ... (2008) Fiber optic glucose sensor based on bionanofilms. *Sensors and Actuators B:*
66. Manesh K, Kim H, Santhosh P, Gopalan A, ... (2008) A novel glucose biosensor based on immobilization of glucose oxidase into multiwall carbon nanotubes-polyelectrolyte-loaded electrospun nanofibrous membrane. *Biosensors and*
67. Reitz E, Jia W, Gentile M, Wang Y, Lei Y (2008) CuO nanospheres based nonenzymatic glucose sensor. *Electroanalysis*.
68. Umar A, Rahman M, Kim S, ... (2008) ZnO nanonails: synthesis and their application as glucose biosensor. *Journal of nanoscience*
69. Zhang X, Wang G, Gu A, Wei Y, Fang B (2008) CuS nanotubes for ultrasensitive nonenzymatic glucose sensors. *Chemical Communications*.
70. Liu X, Hu Q, Wu Q, Zhang W, Fang Z, et al. (2009) Aligned ZnO nanorods: a useful film to fabricate amperometric glucose biosensor. *Colloids and Surfaces B:*
71. Ren X, Chen D, Meng X, Tang F, Du A, et al. (2009) Amperometric glucose biosensor based on a gold nanorods/cellulose acetate composite film as immobilization matrix. *Colloids and Surfaces B:*
72. Safavi A, Maleki N, Farjami E (2009) Fabrication of a glucose sensor based on a novel nanocomposite electrode. *Biosensors and Bioelectronics* 24: 1655-1660.

73. Bai H, Han M, Du Y, Bao J, Dai Z (2010) Facile synthesis of porous tubular palladium nanostructures and their application in a nonenzymatic glucose sensor. *Chem Commun*.
74. García-Morales V, Krischer K (2010) Fluctuation enhanced electrochemical reaction rates at the nanoscale. *Proceedings of the National Academy of Sciences of the United States of America* 107: 4528-4532.
75. Alves W, Alves W, Sousa C, ... (2011) Biosensors based on biological nanostructures: cdn.intechopen.com.
76. Hong J, Han J, Yoon H, Joo P, Lee T, et al. (2011) Carbon-based layer-by-layer nanostructures: from films to hollow capsules. *Nanoscale*.
77. Ju H, Zhang X, Wang J (2011) Biosensors Based on Sol–Gel Nanoparticle Matrices. *NanoBiosensing*.
78. Li J, Yuan R, Chai Y, Che X, Li W, et al. (2011) Nonenzymatic glucose sensor based on a glassy carbon electrode modified with chains of platinum hollow nanoparticles and porous gold nanoparticles in a chitosan *Microchimica acta*.
79. Periasamy A, Chang Y, Chen S (2011) Amperometric glucose sensor based on glucose oxidase immobilized on gelatin-multiwalled carbon nanotube modified glassy carbon electrode. *Bioelectrochemistry*.
80. Ahmad R, Tripathy N, Kim J, Hahn Y (2012) Highly selective wide linear-range detecting glucose biosensors based on aspect-ratio controlled ZnO nanorods directly grown on electrodes. *Sensors and Actuators B:*
81. Liu W, Hashim U, Rao S (2012) Carbon nanotubes-based electrochemical biosensors. *Biomedical Engineering and*
82. Zhang Q, Du Y, Hua J, Di J (2012) Electrodeposition of ZnO Nanosheet Structures and their Application for Glucose Biosensor. *Advanced Materials Research*.
83. Zhong X, Yuan R, Chai Y (2012) In situ spontaneous reduction synthesis of spherical Pd@ Cys-C 60 nanoparticles and its application in nonenzymatic glucose biosensors. *Chemical Communications*.
84. Liu H, Tsai C, Wang G (2013) Glucose biosensors based on a gold nanodendrite modified screen-printed electrode. *Nanotechnology*.
85. Ragupathy D, Lee S, Al-Deyab S, ... (2013) Electrochemical synthesis of a novel poly (2, 5-dimethoxy aniline) nanorod for ultrasensitive glucose biosensor application. *Journal of Industrial and*
86. Wu J, Yin F (2013) Easy Fabrication of a Sensitive Non-Enzymatic Glucose Sensor Based on Electrospinning CuO-ZnO Nanocomposites. *Integrated Ferroelectrics*.
87. Bhattacharya A, Rao V, Jain C, Ghose A, Banerjee S (2014) Bio-sensing property of gold coated ZnO nanorods. *Materials Letters*.
88. SoYoon S, Ramadoss A, Saravanakumar B, ... (2014) Novel Cu/CuO/ZnO hybrid hierarchical nanostructures for non-enzymatic glucose sensor application. *Journal of*
89. Haes AJ, Van Duyne RP (2002) A nanoscale optical biosensor: sensitivity and selectivity of an approach based on the localized surface plasmon resonance spectroscopy of triangular silver nanoparticles. *Journal of the American Chemical Society* 124: 10596-10604.

90. Shafer-Peltier KE, Haynes CL, Glucksberg MR, Van Duyne RP (2003) Toward a glucose biosensor based on surface-enhanced Raman scattering. *Journal of the American Chemical Society* 125: 588-593.
91. Kong KV, Hui Ho CJ, Gong T, On Lau WK, Olivo M (2014) Sensitive SERS Glucose Sensing in Biological Media Using Alkyne Functionalized Boronic acid on Planar Substrates. *Biosensors and Bioelectronics*.
92. Al-Ogaidi I, Gou H, Al-kazaz AK, Aguilar ZP, K Melconian A, et al. (2014) A Gold@ Silica Core-Shell Nanoparticle-Based Surface-Enhanced Raman Scattering Biosensor for Label-Free Glucose Detection. *Analytica chimica acta*.
93. Yonzon CR, Haynes CL, Zhang X, Walsh JT, Van Duyne RP (2004) A glucose biosensor based on surface-enhanced Raman scattering: improved partition layer, temporal stability, reversibility, and resistance to serum protein interference. *Analytical chemistry* 76: 78-85.
94. Zhu X, Li C, Liu Q, Zhu X, ... (2011) Investigation of Non-enzymatic Glucose Biosensor Based on Graphene/Gold Nanocomposites: *Zhongguo Kexueyuan, Changchun*
95. Zhu J, Chen M, He Q, Shao L, Wei S, et al. (2013) An overview of the engineered graphene nanostructures and nanocomposites. *RSC Adv*.
96. Zhou Y, Wang L, Ye Z, Zhao M, Cai H, et al. (2013) Mango core inner shell membrane template-directed synthesis of porous ZnO films and their application for enzymatic glucose biosensor. *Applied Surface Science*.
97. Zhou C, Shi Y, Ding X, Li M, Luo J, et al. (2012) Development of a fast and sensitive glucose biosensor using iridium complex-doped electrospun optical fibrous membrane. *Analytical*
98. Zhang Y, Sun X, Zhu L, Shen H, Jia N (2011) Electrochemical sensing based on graphene oxide/Prussian blue hybrid film modified electrode. *Electrochimica Acta*.
99. Zhang X, Liao Q, Chu M, Liu S, Zhang Y (2014) Structure effect on graphene-modified enzyme electrode glucose sensors. *Biosensors and Bioelectronics*.
100. Zhang W, Ganesh N, Block I, ... (2008) High sensitivity photonic crystal biosensor incorporating nanorod structures for enhanced surface area. *Sensors and Actuators B: Chemical*.
101. Zhang J, Zhu X, Dong H, Zhang X, Wang W, et al. (2013) In situ growth cupric oxide nanoparticles on carbon nanofibers for sensitive nonenzymatic sensing of glucose. *Electrochimica Acta*.
102. Zhang J (2012) Improved sensing with nanostructures. *The Journal of Physical Chemistry Letters*.
103. Zhang G (2011) Design and fabrication of 3D skyscraper nanostructures and their applications in biosensors: cdn.intechopen.com.
104. Yuan M, Liu A, Zhao M, Dong W, Zhao T, et al. (2014) Bimetallic PdCu nanoparticle decorated three-dimensional graphene hydrogel for non-enzymatic amperometric glucose sensor. *Sensors and Actuators B: Chemical*.
105. Šimelevičius D, Petrauskas K, Baronas R, Razumienė J (2014) Computational Modeling of Mediator Oxidation by Oxygen in an Amperometric Glucose Biosensor. *Sensors* 14: 2578-2594.

106. Razumiene J, Gureviciene V, Sakinyte I, Barkauskas J, Petrauskas K, et al. (2013) Modified SWCNTs for Reagentless Glucose Biosensor: Electrochemical and Mathematical Characterization. *Electroanalysis* 25: 166-173.
107. Loghambal S, Rajendran L (2011) Mathematical modeling in amperometric oxidase enzyme–membrane electrodes. *Journal of Membrane Science* 373: 20-28.
108. Romero MR, Baruzzi AM, Garay F (2012) How low does the oxygen concentration go within a sandwich-type amperometric biosensor? *Sensors and Actuators B: Chemical* 174: 279-284.
109. Morgan TH (1910) Chromosomes and heredity. *American Naturalist*: 449-496.
110. Akam M (1987) The Molecular-Basis for Metameric Pattern in the *Drosophila* Embryo. *Development* 101: 1-&.
111. Anderson K (1987) Dorsal Ventral Embryonic Pattern Genes of *Drosophila*. *Trends in Genetics* 3: 91-97.
112. Lehmann R, Nusslein-Volhard C (1987) Hunchback, a gene required for segmentation of the anterior and posterior region of the *Drosophila* embryo. *Developmental Biology* 119: 402-417.
113. Driever W, Nusslein-Volhard C (1988) A gradient of Bicoid protein in *Drosophila* embryos. *Cell* 54: 83-93.
114. Driever W, Nusslein-Volhard C (1988) The Bicoid protein determines position in the *Drosophila* embryo in a concentration-dependent manner. *Cell*: 95-104.
115. Driever W, Ma J, Nusslein-Volhard C, Ptashne M (1989) Rescue of Bicoid mutant *Drosophila* embryos by Bicoid fusion proteins containing heterologous activating sequences. *Nature*: 149-154.
116. Driever W, Nusslein-Volhard C (1989) The Bicoid protein is a positive regulator of Hunchback transcription in the early *Drosophila* embryo. *Nature*: 138-143.
117. Driever W, Thoma G, Nusslein-Volhard C (1989) Determination of spatial domains of zygotic gene-expression in the *Drosophila* embryo by the affinity of binding-sites for the Bicoid morphogen. *Nature*: 363-367.
118. Bronner G, Jackle H (1991) Control and function of terminal gap gene activity in the posterior pole region of the *Drosophila* embryo. *Mechanisms of Development*: 205-211.
119. Hulskamp M, Tautz D (1991) Gap Genes and Gradients - The Logic Behind the Gaps. *Bioessays* 13: 261-268.
120. Nusslein-Volhard C (1991) Determination of the embryonic axes of *Drosophila*. *Development*.
121. Small S, Kraut R, Hoey T, Warrior R, Levine M (1991) Transcriptional regulation of a pair-rule stripe in *Drosophila*. *Genes & Development*: 827-839.
122. Capovilla M, Eldon E, Pirrotta V (1992) The giant gene of *Drosophila* encodes a B-zip DNA-binding protein that regulates the expression of other segmentation gap genes. *Development* 114: 99-112.
123. St. Johnston D, Nusslein-Volhard C (1992) The origin of pattern and polarity in the *Drosophila* embryo. *Cell*: 201-219.
124. Simpsonbrose M, Treisman J, Desplan C (1994) Synergy between the Hunchback and Bicoid morphogens is required for anterior patterning in *Drosophila*. *Cell* 78: 855-865.

125. Sanchez L, Thieffry D (2001) A logical analysis of the *Drosophila* gap-gene system. *Journal of Theoretical Biology*: 115-141.
126. Gregor T, Bialek W, van Steveninck R, Tank D, Wieschaus E (2005) Diffusion and scaling during early embryonic pattern formation. *Proceedings of the National Academy of Sciences of the United States of America*: 18403-18407.
127. Jaeger J, Reinitz J (2006) On the dynamic nature of positional information. *Bioessays*: 1102-1111.
128. Perkins T, Jaeger J, Reinitz J, Glass L (2006) Reverse engineering the gap gene network of *Drosophila melanogaster*. *PLoS Computational Biology* 2: DOI: 10.1371/journal.pcbi.0020051.
129. Bollenbach T, Pantazis P, Kicheva A, Bokel C, Gonzalez-Gaitan M, et al. (2008) Precision of the Dpp gradient. *Development*: 1137-1146.
130. Lucchetta E, Vincent M, Ismagilov R (2008) A Precise Bicoid Gradient Is Nonessential during Cycles 11-13 for Precise Patterning in the *Drosophila* Blastoderm. *PLoS One*: -.
131. Liberman L, Reeves G, Stathopoulos A (2009) Quantitative imaging of the Dorsal nuclear gradient reveals limitations to threshold-dependent patterning in *Drosophila*. *Proceedings of the National Academy of Sciences of the United States of America*: 22317-22322.
132. Spencer FA, Hoffmann FM, Gelbart WM (1982) Decapentaplegic: a gene complex affecting morphogenesis in *Drosophila melanogaster*. *Cell* 28: 451-461.
133. Blackman RK, Sanicola M, Raftery LA, Gillevet T, Gelbart WM (1991) An extensive 3' cis-regulatory region directs the imaginal disk expression of decapentaplegic, a member of the TGF-beta family in *Drosophila*. *Development* 111: 657-666.
134. Baonza A, Roch F, Martin-Blanco E (2000) DER signaling restricts the boundaries of the wing field during *Drosophila* development. *Proceedings of the National Academy of Sciences of the United States of America* 97: 7331-7335.
135. Schweizer L, Nellen D, Basler K (2003) Requirement for Pangolin/dTCF in *Drosophila* Wingless signaling. *Proceedings of the National Academy of Sciences of the United States of America* 100: 5846-5851.
136. Kopyl SA, Dorogova NV, Baimak T, Chang L, Omel'ianchuk LV (2008) [Role of the porcupine gene in the development of the wing imaginal disk of *Drosophila melanogaster*]. *Genetika* 44: 1486-1492.
137. Reinitz J, Mjolsness E, Sharp DH (1995) Model for cooperative control of positional information in *Drosophila* by Bicoid and maternal Hunchback. *Journal of Experimental Zoology* 271: 47-56.
138. Jaeger J, Blagov M, Kosman D, Kozlov K, Manu, et al. (2004) Dynamical analysis of regulatory interactions in the gap gene system of *Drosophila melanogaster*. *Genetics*: 1721-1737.
139. Jaeger J, Surkova S, Blagov M, Janssens H, Kosman D, et al. (2004) Dynamic control of positional information in the early *Drosophila* embryo. *Nature*: 368-371.

140. Ashyraliyev M, Siggins K, Janssens H, Blom J, Akam M, et al. (2009) Gene Circuit Analysis of the Terminal Gap Gene *huckebein*. *PLoS Computational Biology* 5: doi:10.1371/journal.pcbi.1000548.
141. Jaeger J (2011) The gap gene network. *Cellular and Molecular Life Sciences*: 243-274.
142. Gregor T, Wieschaus E, McGregor A, Bialek W, Tank D (2007) Stability and nuclear dynamics of the bicoid morphogen gradient. *Cell*: 141-152.
143. Jaeger J, Sharp D, Reinitz J (2007) Known maternal gradients are not sufficient for the establishment of gap domains in *Drosophila melanogaster*. *Mechanisms of Development*: 108-128.
144. Driever W, Siegel V, Nusslein-Volhard C (1990) Autonomous determination of anterior structures in the early *Drosophila* embryo by the Bicoid morphogen. *Development*: 811-820.
145. St. Johnston D, Driever W, Berleth T, Riehlstein S, Nusslein-Volhard C (1989) Multiple steps in the localization of Bicoid RNA to the anterior pole of the *Drosophila* oocyte. *Development*: 13-19.
146. Wu Y, Myasnikova E, Reinitz J (2007) Master equation simulation analysis of immunostained Bicoid morphogen gradient. *BMC Systems Biology*: -.
147. Alves F, Dilao R (2006) Modeling segmental patterning in *Drosophila*: Maternal and gap genes. *Journal of Theoretical Biology* 241: 342-359.
148. Ibanes M, Belmonte JCI (2008) Theoretical and experimental approaches to understand morphogen gradients. *Molecular Systems Biology* 4.
149. Lipshitz HD (2009) Follow the mRNA: a new model for Bicoid gradient formation. *Nature Reviews Molecular Cell Biology* 10: 509-512.
150. Spirov A, Fahmy K, Schneider M, Frei E, Noll M, et al. (2009) Formation of the bicoid morphogen gradient: an mRNA gradient dictates the protein gradient. *Development* 136: 605-614.
151. Cheung D, Miles C, Kreitman M, Ma J (2011) Scaling of the Bicoid morphogen gradient by a volume-dependent production rate. *Development* 138: 2741-2749.
152. Jackle H, Tautz D, Schuh R, Seifert E, Lehmann R (1986) Cross-regulatory interactions among the gap genes of *Drosophila*. *Nature* 324: 668-670.
153. Hulskamp M, Pfeifle C, Tautz D (1990) A morphogenetic gradient of Hunchback protein organizes the expression of the gap genes *Kruppel* and *Knirps* in the early *Drosophila* embryo. *Nature* 346: 577-580.
154. Eldon E, Pirrotta V (1991) Interactions of the *Drosophila* gap gene *Giant* with maternal and zygotic pattern-forming genes. *Development* 111: 367-378.
155. Kraut R, Levine M (1991) Mutually repressive interactions between the gap genes *Giant* and *Kruppel* define the middle body regions of the *Drosophila* embryo. *Development* 111: 611-621.
156. Struhl G, Johnston P, Lawrence P (1992) Control of *Drosophila* body pattern by the Hunchback morphogen gradient. *Cell* 69: 237-249.
157. Fomekong-Nanfack Y, Kaandorp J, Blom J (2007) Efficient parameter estimation for spatio-temporal models of pattern formation: case study of *Drosophila melanogaster*. *Bioinformatics* 23: 3356-3363.

158. Ashyraliyev M, Jaeger J, Blom J (2008) Parameter estimation and determinability analysis applied to *Drosophila* gap gene circuits. *BMC Systems Biology* 2: doi:10.1186/1752-0509-1182-1183.
159. Ishihara S, Shibata T (2008) Mutual interaction in network motifs robustly sharpens gene expression in developmental processes. *Journal of Theoretical Biology*: 131-144.
160. Fomekong-Nanfack Y, Postma M, Kaandorp J (2009) Inferring *Drosophila* gap gene regulatory network: a parameter sensitivity and perturbation analysis. *BMC Systems Biology*: -.
161. Manu, Surkova S, Spirov A, Gursky V, Janssens H, et al. (2009) Canalization of Gene Expression and Domain Shifts in the *Drosophila* Blastoderm by Dynamical Attractors. *PLoS Computational Biology* 5: DOI: 10.1371/journal.pcbi.1000303.
162. Hengeniuss J, Gribskov M, Rundell A, Fowlkes C, Umulis D (2011) Analysis of Gap Gene Regulation in a 3D Organism-Scale Model of the *Drosophila melanogaster* Embryo. *Plos One* 6.
163. Kozlov K, Surkova S, Myasnikova E, Reinitz J, Samsonova M (2012) Modeling of Gap Gene Expression in *Drosophila* Kruppel Mutants. *PLoS Computational Biology* 8: DOI: 10.1371/journal.pcbi.1002635.
164. Siegal ML, Bergman A (2002) Waddington's canalization revisited: Developmental stability and evolution. *Proceedings of the National Academy of Sciences of the United States of America* 99: 10528-10532.
165. Bieler J, Pozzorini C, Naef F (2011) Whole-embryo modeling of early segmentation in *Drosophila* identifies robust and fragile expression domains. *Biophysical Journal* 101: 287-296.
166. Jimenez-Hornero JE, Santos-Duenas IM, Garcia-Garcia I (2009) Optimization of biotechnological processes. The acetic acid fermentation. Part II: Practical identifiability analysis and parameter estimation. *Biochemical Engineering Journal* 45: 7-21.
167. Rübél O, Weber G, Keränen S, Fowlkes C, Luengo-Hendriks C, et al. PointCloudXplore: Visual Analysis of 3D Gene Expression Data Using Physical Views and Parallel Coordinates. In: Ertl T, Joy K, Santos B, editors; 2006; Lisbon, Portugal. The Eurographics Association. pp. 203-210.
168. Claridge SA, Schwartz JJ, Weiss PS (2011) Electrons, Photons, and Force: Quantitative Single-Molecule Measurements from Physics to Biology. *ACS Nano* 5: 693-729.
169. Jiang X, Hu J, Fitzgerald LA, Biffinger JC, Xie P, et al. (2010) Probing electron transfer mechanisms in *Shewanella oneidensis* MR-1 using a nanoelectrode platform and single-cell imaging. *Proc Natl Acad Sci USA* 107: 16806-16810.
170. Sun P, Laforge FoO, Abeyweera TP, Rotenberg SA, Carpino J, et al. (2008) Nanoelectrochemistry of mammalian cells. *Proceedings of the National Academy of Sciences of the United States of America* 105: 443-448.
171. Tricoli A, Pratsinis SE (2009) Dispersed nanoelectrode devices. *Nat Nano* 5: 54-60.
172. Velmurugan J, Zhan D, Mirkin MV (2010) Electrochemistry through glass. *Nat Chem* 2: 498-502.

173. Compton RG, Wildgoose GG, Rees NV, Streeter I, Baron R (2008) Design, fabrication, characterisation and application of nanoelectrode arrays. *Chem Phys Lett* 459: 1-17.
174. Soleymani L, Fang Z, Sargent EH, Kelley SO (2009) Programming the detection limits of biosensors through controlled nanostructuring. *Nat Nanotechnol* 4: 844-848.
175. Murray RW (2008) Nanoelectrochemistry: metal nanoparticles, nanoelectrodes, and nanopores. *Chem Rev* 108: 2688-2720.
176. Zhang B, Zhang Y, White HS (2006) Steady-state voltammetric response of the nanopore electrode. *Anal Chem* 78: 477-483.
177. Bard AJ, Faulkner LR (2001) *Electrochemical Methods. Fundamentals and Applications*. New York: John Wiley. 1-43 p.
178. Rao CNR, Kulkarni GU, Thomas PJ, Edwards PP (2002) Size-dependent chemistry: properties of nanocrystals. *Chem Eur J* 8: 28-35.
179. Godino N, Borrisé X, Mun oz FX, del Campo FJ, Compton RG (2009) Mass transport to nanoelectrode arrays and limitations of the diffusion domain approach: theory and experiment. *J Phys Chem C* 113: 11119-11125.
180. Lin Y, Lu F, Tu Y, Ren Z (2004) Glucose biosensors based on carbon nanotube nanoelectrode ensembles. *Nano Lett* 4: 191-195.
181. Tan LK, Chong ASM, Tang XSE, Gao H (2007) Combining atomic layer deposition with a template-assisted approach to fabricate size-reduced nanowire arrays on substrates and their electrochemical characterization. *J Phys Chem C* 111: 4964-4968.
182. Menshykau D, Huang XJ, Rees NV, Del Campo FJ, Muñoz FX, et al. (2008) Investigating the concept of diffusional independence. Potential step transients at nano- and micro-electrode arrays: theory and experiment. *Analyst* 134: 343-348.
183. Lanyon YH, Arrigan DWM (2007) Recessed nanoband electrodes fabricated by focused ion beam milling. *Sensors and Actuators B: Chemical* 121: 341-347.
184. Sandison ME, Cooper JM (2006) Nanofabrication of electrode arrays by electron-beam and nanoimprint lithographies. *Lab Chip* 6: 1020-1025.
185. Sander MS, Tan LS (2003) Nanoparticle arrays on surfaces fabricated using anodic alumina films as templates. *Adv Funct Mater* 13: 393-397.
186. Katz E, Willner I, Wang J (2004) Electroanalytical and bioelectroanalytical systems based on metal and semiconductor nanoparticles. *Electroanalysis* 16: 19-44.
187. Luo X, Morrin A, Killard AJ, Smyth MR (2006) Application of nanoparticles in electrochemical sensors and biosensors. *Electroanalysis* 18: 319-326.
188. Rakhi RB, Sethupathi K, Ramaprabhu S (2009) A Glucose Biosensor Based on Deposition of Glucose Oxidase onto Crystalline Gold Nanoparticle Modified Carbon Nanotube Electrode. *J Phys Chem B* 113: 3190-3194.
189. Wen Z, Ci S, Li J (2009) Pt nanoparticles inserting in carbon nanotube arrays: nanocomposites for glucose biosensors. *J Phys Chem C* 113: 13482-13487.
190. Lu J, Do I, Drzal LT, Worden RM, Lee I (2008) Nanometal-Decorated Exfoliated Graphite Nanoplatelet Based Glucose Biosensors with High Sensitivity and Fast Response. *ACS Nano* 2: 1825-1832.

191. Hong W, Bai H, Xu Y, Yao Z, Gu Z, et al. (2010) Preparation of Gold Nanoparticle/Graphene Composites with Controlled Weight Contents and Their Application in Biosensors. *J Phys Chem C* 114: 1822-1826.
192. Maschmann MR, Franklin AD, Scott A, Janes DB, Sands TD, et al. (2006) Lithography-free in situ ohmic contacts to single-walled carbon nanotubes. *Nano Lett* 6: 2712-2717.
193. Menshykau D, Huang XJ, Rees NV, Del Campo FJ, Muñoz FX, et al. (2009) Investigating the concept of diffusional independence. Potential step transients at nano-and micro-electrode arrays: theory and experiment. *Analyst* 134: 343-348.
194. Baronas R, Ivanauskas F, Kulys J (2003) The influence of the enzyme membrane thickness on the response of amperometric biosensors. *Sensors* 3: 248-262.
195. Bartlett PN, Pratt KFE (1993) Modeling of processes in enzyme electrodes. *Biosensors and Bioelectronics* 8: 451-462.
196. Squires TM, Messinger RJ, Manalis SR (2008) Making it stick: convection, reaction and diffusion in surface-based biosensors. *Nat Biotechnol* 26: 417.
197. Vijayendran RA, Ligler FS, Leckband DE (1999) A computational reaction-diffusion model for the analysis of transport-limited kinetics. *Analytical Chemistry* 71: 5405-5412.
198. Franklin AD, Janes DB, Claussen JC, Fisher TS, Sands TD (2008) Independently addressable fields of porous anodic alumina embedded in SiO₂ on Si. *Appl Phys Lett* 92: 013122.
199. Anandan V, Gangadharan R, Zhang G (2009) Role of SAM Chain Length in Enhancing the Sensitivity of Nanopillar Modified Electrodes for Glucose Detection. *Sensors* 9: 1295.
200. Brito R, Tremont R, Feliciano O, Cabrera CR (2003) Chemical derivatization of self-assembled 3-mercaptopropionic and 16-mercaptohexadecanoic acids at platinum surfaces with 3-aminopropyltrimethoxysilane: a spectroscopic and electrochemical study. *J Electroanal Chem* 540: 53-59.
201. Ziegler KJ, Gu Z, Peng H, Flor EL, Hauge RH, et al. (2005) Controlled oxidative cutting of single-walled carbon nanotubes. *J Am Chem Soc* 127: 1541-1547.
202. Guo S, Wen D, Zhai Y, Dong S, Wang E (2010) Platinum Nanoparticle Ensemble-on-Graphene Hybrid Nanosheet: One-Pot, Rapid Synthesis, and Used as New Electrode Material for Electrochemical Sensing. *ACS Nano* 4: 3959-3968.
203. Liu Z, Lin X, Lee JY, Zhang W, Han M, et al. (2002) Preparation and Characterization of Platinum-Based Electrocatalysts on Multiwalled Carbon Nanotubes for Proton Exchange Membrane Fuel Cells. *Langmuir* 18: 4054-4060.
204. Cambiaso A, Delfino L, Grattarola M, Verreschi G, Ashworth D, et al. (1996) Modelling and simulation of a diffusion limited glucose biosensor. *Sensors and Actuators B: Chemical* 33: 203-207.
205. Lemke K (1988) Mathematical simulation of an amperometric enzyme-substrate electrode with apO 2 basic sensor. *Med Biol Eng Comput* 26: 523-532.
206. Mell LD, Maloy JT (1975) Model for the amperometric enzyme electrode obtained through digital simulation and applied to the immobilized glucose oxidase system. *Anal Chem* 47: 299-307.

207. Campbell FW, Belding SR, Baron R, Xiao L, Compton RG (2009) The hydrogen evolution reaction at a silver nanoparticle array and a silver macroelectrode compared: changed electrode kinetics between the macro-and nanoscales. *J Phys Chem C* 113: 14852-14857.
208. Jeoung E, Galow TH, Schotter J, Bal M, Ursache A, et al. (2001) Fabrication and characterization of nanoelectrode arrays formed via block copolymer self-assembly. *Langmuir* 17: 6396-6398.
209. Streeter I, Baron R, Compton RG (2007) Voltammetry at nanoparticle and microparticle modified electrodes: theory and experiment. *J Phys Chem C* 111: 17008-17014.
210. Montgomery DC, Runger GC (2010) Applied statistics and probability for engineers. New York: John Wiley. 135-140 p.
211. Davies TJ, Compton RG (2005) The cyclic and linear sweep voltammetry of regular and random arrays of microdisc electrodes: Theory. *J Electroanal Chem* 585: 63-82.
212. Fletcher S, Horne MD (1999) Random assemblies of microelectrodes (RAMTM electrodes) for electrochemical studies. *Electrochem Commun* 1: 502-512.
213. Hrapovic S, Liu Y, Male KB, Luong JH (2004) Electrochemical biosensing platforms using platinum nanoparticles and carbon nanotubes. *Anal Chem* 76: 1083-1088.
214. Kang X, Mai Z, Zou X, Cai P, Mo J (2008) Glucose biosensors based on platinum nanoparticles-deposited carbon nanotubes in sol-gel chitosan/silica hybrid. *Talanta* 74: 879-886.
215. Pang X, He D, Luo S, Cai Q (2009) An amperometric glucose biosensor fabricated with Pt nanoparticle-decorated carbon nanotubes/TiO₂ nanotube arrays composite. *Sens Actuators, B* 137: 134-138.
216. Tsai MC, Tsai YC (2009) Adsorption of glucose oxidase at platinum-multiwalled carbon nanotube-alumina-coated silica nanocomposite for amperometric glucose biosensor. *Sens Actuators, B* 141: 592-598.
217. Zhao K, Zhuang S, Chang Z, Songm H, Dai L, et al. (2007) Amperometric glucose biosensor based on platinum nanoparticles combined aligned carbon nanotubes electrode. *Electroanalysis* 19: 1069-1074.
218. Kim SS, Amama PB, Fisher TS (2010) Preferential Biofunctionalization of Carbon Nanotubes Grown by Microwave Plasma-Enhanced CVD. *J Phys Chem C* 114: 9596-9602.
219. Narayanan R, El-Sayed MA (2005) Catalysis with transition metal nanoparticles in colloidal solution: Nanoparticle shape dependence and stability. *The Journal of Physical Chemistry B* 109: 12663-12676.
220. Banks CE, Compton RG (2006) New electrodes for old: from carbon nanotubes to edge plane pyrolytic graphite. *Analyst* 131: 15-21.
221. Bong S, Kim YR, Kim I, Woo S, Uhm S, et al. Graphene supported electrocatalysts for methanol oxidation. *Electrochem Commun* 12: 129-131.
222. Kagie A, Bishop DK, Burdick J, La Belle JT, Dymond R, et al. (2008) Flexible Rolled Thick Film Miniaturized Flow Cell for Minimally Invasive Amperometric Sensing. *Electroanalysis* 20: 1610-1614.

223. Mukhopadhyay R (2006) Devices to drool for. *Analytical Chemistry* 78: 4255-4259.
224. Tabak LA (2007) Point of Care Diagnostics Enter the Mouth. *Annals of the New York Academy of Sciences* 1098: 7-14.
225. Jung S-K, Trimarchi JR, Sanger RH, Smith PJS (2001) Development and application of a self-referencing glucose microsensor for the measurement of glucose consumption by pancreatic β -Cells. *Anal Chem* 73: 3759-3767.
226. Porterfield DM (2007) Measuring metabolism and biophysical flux in the tissue, cellular and sub-cellular domains: Recent developments in self-referencing amperometry for physiological sensing. *Biosensors and Bioelectronics* 22: 1186-1196.
227. Anscombe F (1973) Graphs in Statistical Analysis. *The American Statistician* 27: 17-21.
228. Cover T, Thomas J (1991) *Elements of Information Theory*: Wiley Interscience. 576 p.
229. Guinee RA, Lyden C, Aacc, Aacc A. Motor parameter identification using response surface simulation and analysis. *Proceedings of the American Control Conference*; 2001; Arlington, Va. pp. 4597-4602.
230. Müller M (2007) *Information Retrieval for Music and Motion*: Springer-Verlag New York, Inc.
231. Deza M, Deza E (2009) *Encyclopedia of Distances*. 2 ed. Berlin, Heidelberg: Springer-Verlag.
232. Saltelli A, Ratto M, Andres T, Compolongo F, Cariboni J, et al. (2008) *Global Sensitivity Analysis: The Primer*. Chichester, West Sussex, UK: Wiley. 282 p.
233. Kauffman SA (1993) *The origins of order: Self-organization and selection in evolution*. The origins of order: Self-organization and selection in evolution: xviii+709p-xviii+709p.
234. Spall JC (2003) *Introduction to Stochastic Search and Optimization*. Hoboken, N.J.: Wiley.
235. Alajlan N (2011) HopDSW: An approximate dynamic space warping algorithm for fast shape matching and retrieval. *Journal of King Saud University - Computer and Information Sciences* 23: 7-14.
236. Umulis D, Shimmi O, O'Connor M, Othmer H (2010) Organism-Scale Modeling of Early *Drosophila* Patterning via Bone Morphogenetic Proteins. *Developmental Cell* 18: 260-274.
237. Bazil JN, Buzzard GT, Rundell AE (2012) A Global Parallel Model Based Design of Experiments Method to Minimize Model Output Uncertainty. *Bulletin of Mathematical Biology* 74: 688-716.
238. PubMed.gov. Bethesda, MD: National Center for Biotechnology Information, U.S. National Library of Medicine.
239. Noble SL, Sherer E, Hannemann RE, Ramkrishna D, Vik T, et al. (2010) Using adaptive model predictive control to customize maintenance therapy chemotherapeutic dosing for childhood acute lymphoblastic leukemia. *Journal of Theoretical Biology* 264: 990-1002.
240. Chen BS, Lin YP (2013) A Unifying Mathematical Framework for Genetic Robustness, Environmental Robustness, Network Robustness and their Trade-offs

- on Phenotype Robustness in Biological Networks. Part III: Synthetic Gene Networks in Synthetic Biology. *Evolutionary Bioinformatics* 9: 87-109.
241. MacNamara A, Terfve C, Henriques D, Bernabe BP, Saez-Rodriguez J (2012) State-time spectrum of signal transduction logic models. *Physical Biology* 9: 045003. doi: 045010.041088/041478-043975/045009/045004/045003.
 242. Coppey M, Berezhkovskii AM, Kim Y, Boettiger AN, Shvartsman SY (2008) Modeling the bicoid gradient: Diffusion and reversible nuclear trapping of a stable protein (vol 312, pg 623, 2007). *Developmental Biology* 316: 548-548.
 243. He F, Saunders TE, Wen Y, Cheung D, Jiao RJ, et al. (2010) Shaping a Morphogen Gradient for Positional Precision. *Biophysical Journal* 99: 697-707.
 244. Houchmandzadeh B, Wieschaus E, Leibler S (2002) Establishment of developmental precision and proportions in the early *Drosophila* embryo. *Nature* 415: 798-802.
 245. Munteanu A, Sole R (2008) Neutrality and Robustness in Evo-Devo: Emergence of Lateral Inhibition. *PLoS Computational Biology*: -.
 246. Negre N, Brown CD, Ma L, Bristow CA, Miller SW, et al. (2011) A cis-regulatory map of the *Drosophila* genome. *Nature* 471: 527-531.
 247. modEncode C, Roy S, Ernst J, Kharchenko PV, Kheradpour P, et al. (2010) Identification of functional elements and regulatory circuits by *Drosophila* modENCODE. *Science* 330: 1787-1797.
 248. *Drosophila* 12 Genomes C, Clark AG, Eisen MB, Smith DR, Bergman CM, et al. (2007) Evolution of genes and genomes on the *Drosophila* phylogeny. *Nature* 450: 203-218.
 249. Arlot S (2010) A survey of cross-validation procedures for model selection. *Statistics Surveys* 4: 40-79.
 250. Hawkins DM (2004) The problem of overfitting. *Journal of Chemical Information and Computer Sciences* 44: 1-12.
 251. Y. NA. Feature selection, L1 vs. L2 regularization, and rotational invariance; 2004. *Proceedings of the 21st Annual International Conference on Machine Learning*, ACM. pp. 78.
 252. Bishop CM (2006) *Pattern recognition and machine learning*. New York: Springer.
 253. Xun X, Cao J, Mallick B, Maity A, Carroll RJ (2013) Parameter Estimation of Partial Differential Equation Models. *Journal of the American Statistical Association* 108: 1009-1020.
 254. Leclerc RD (2008) Survival of the sparsest: robust gene networks are parsimonious. *Mol Syst Biol* 4: 213.
 255. Spirov AV, Holloway DM (2013) Modeling the evolution of gene regulatory networks for spatial patterning in embryo development. *Procedia Comput Sci* 18.
 256. Spirov A, Holloway D (2013) Using evolutionary computations to understand the design and evolution of gene and cell regulatory networks. *Methods* 62: 39-55.
 257. Spirov AV, Sabirov MA, Holloway DM (2012) In silico evolution of gene cooption in pattern-forming gene networks. *ScientificWorldJournal* 2012: 560101.
 258. de Hoon MJ, Imoto S, Kobayashi K, Ogasawara N, Miyano S (2003) Inferring gene regulatory networks from time-ordered gene expression data of *Bacillus subtilis* using differential equations. *Pac Symp Biocomput*: 17-28.

259. Golub GH, van Loan CF (1980) An analysis of the total least squares problem. *Siam Journal on Numerical Analysis* 17: 883–893.
260. Kitano H (2010) Violations of robustness trade-offs. *Mol Syst Biol* 6: 384.
261. Kitano H (2007) Towards a theory of biological robustness. *Mol Syst Biol* 3: 137.
262. Kitano H (2004) Biological robustness. *Nat Rev Genet* 5: 826-837.
263. Garfield DA, Runcie DE, Babbitt CC, Haygood R, Nielsen WJ, et al. (2013) The impact of gene expression variation on the robustness and evolvability of a developmental gene regulatory network. *PLoS Biol* 11: e1001696.
264. Jaeger J, Manu, Reinitz J (2012) *Drosophila* blastoderm patterning. *Curr Opin Genet Dev* 22: 533-541.
265. Gursky VV, Surkova SY, Samsonova MG (2012) Mechanisms of developmental robustness. *Biosystems* 109: 329-335.
266. Lander AD (2011) Pattern, growth, and control. *Cell* 144: 955-969.
267. Gursky VV, Panok L, Myasnikova EM, Manu, Samsonova MG, et al. (2011) Mechanisms of gap gene expression canalization in the *Drosophila* blastoderm. *BMC Syst Biol* 5: 118.
268. Rodrigo G, Carrera J, Elena SF, Jaramillo A (2010) Robust dynamical pattern formation from a multifunctional minimal genetic circuit. *BMC Syst Biol* 4: 48.
269. Delattre M, Felix MA (2009) The evolutionary context of robust and redundant cell biological mechanisms. *Bioessays* 31: 537-545.
270. Chaves M, Sengupta A, Sontag ED (2009) Geometry and topology of parameter space: investigating measures of robustness in regulatory networks. *J Math Biol* 59: 315-358.
271. Umulis D, O'Connor MB, Othmer HG (2008) Robustness of embryonic spatial patterning in *Drosophila melanogaster*. *Curr Top Dev Biol* 81: 65-111.
272. Chaves M, Albert R (2008) Studying the effect of cell division on expression patterns of the segment polarity genes. *J R Soc Interface* 5 Suppl 1: S71-84.
273. Baker RE, Maini PK (2007) Travelling gradients in interacting morphogen systems. *Math Biosci* 209: 30-50.
274. Tsikolia N (2006) The role and limits of a gradient based explanation of morphogenesis: a theoretical consideration. *Int J Dev Biol* 50: 333-340.
275. Ma W, Lai L, Ouyang Q, Tang C (2006) Robustness and modular design of the *Drosophila* segment polarity network. *Mol Syst Biol* 2: 70.
276. Proulx SR, Phillips PC (2005) The opportunity for canalization and the evolution of genetic networks. *Am Nat* 165: 147-162.
277. Nijhout HF (2002) The nature of robustness in development. *Bioessays* 24: 553-563.
278. Gibson G (2002) Developmental evolution: getting robust about robustness. *Curr Biol* 12: R347-349.
279. Furusawa C, Kaneko K (2001) Theory of robustness of irreversible differentiation in a stem cell system: chaos hypothesis. *J Theor Biol* 209: 395-416.
280. Fowlkes C, Luengo Hendriks C, Keranen S, Weber G, Rubel O, et al. (2008) A quantitative spatiotemporal atlas of gene expression in the *Drosophila* blastoderm. *Cell*: 364-374.

VITA

VITA

James Hengenius
Graduate School, Purdue University

Education

B.S., Biology, 2007, Case Western Reserve University, Cleveland, Ohio
Ph.D., Biology, 2014, Purdue University, West Lafayette, Indiana

Awards and Fellowships

Lynn Fellowship
NIH Molecular Biophysics Training Grant
Computational Life Sciences (CLS) specialization at Purdue University

Teaching Experience

Lecture and laboratory teaching assistant for Introductory Anatomy and Physiology, 6 semesters.

Research Interests

Dynamic system modeling.
Intracellular signaling models.
Spatiotemporal developmental systems.
Agent-based game theoretic models of evolutionary processes.
Computer-aided metabolic engineering.

Articles

1) James Hengenius, Michael Gribskov, Ann Rundell, Charless Fowlkes, and David Umulis. "Analysis of Gap Gene Regulation in a 3D Organism-Scale Model of the *Drosophila melanogaster* Embryo."(2011) PLoS ONE 6(11): e26797.

2) Jonathan Claussen, James Hengenus, Monique Wickner, Timothy Fisher, David Umulis, David Umulis. "Effects of Carbon Nanotube-Tethered Nanosphere Density on Amperometric Biosensing: Simulation and Experiment." (2011) *Journal of Physical Chemistry C*. 115(43): 20896–209043) Hengenus, JB, Gribskov, M, Rundell, AE, Umulis, DM. (2014) Making models match measurements: Model optimization for morphogen patterning networks. *Seminars in Cell and Developmental Biology* 35C:109-123

Meetings and Abstracts

1) James Hengenus, Ann E. Rundell, Michael Gribskov, and David M. Umulis. "Effects of a realistic 3D domain on models of *Drosophila melanogaster* gap gene regulation." SIAM Great Lakes Conference: Modeling and Numerical PDEs in Mathematical Biology. University of Michigan-Dearborn, April 2010.

2) James Hengenus, Ann E. Rundell, Michael Gribskov, and David M. Umulis. "Drosophila melanogaster gap gene regulation: geometric effects of realistic embryonic geometries." From Computation Biophysics to Systems Biology. Northwestern Michigan University, June 2010.

3) James Hengenus, Ann E. Rundell, Michael Gribskov, and David M. Umulis. "Gap Gene Regulation In *Drosophila*: A Study in Multi-Objective Optimization of Spatiotemporal Models." From the American Institute of Chemical Engineers Annual Meeting. Minneapolis, October 2011.

4) James Hengenus, Ann E. Rundell, Michael Gribskov, and David M. Umulis. "Choosing the Best Error Metric for Parameter Estimation: A Case Study in *Drosophila* Gap Gene Interaction." From ICSB Intelligent Systems for Molecular Biology Conference. Long Beach, 2012.

Bio

James earned his biology bachelor of science at Case Western Reserve University in 2007. During his graduate education at Purdue, he studied in an interdisciplinary life sciences program. Drawing from biological, biomedical engineering, and biological and agricultural engineering, he worked to identify genetic regulatory networks in early *Drosophila* development. His other research interests include stochastic optimization methods for high-dimensional parameter estimation, objective function choice in spatiotemporal systems, control theory applied to biomedical systems, and dynamic modeling formalisms applied to biological and biotechnological systems.